CHARGE STORAGE AND TRANSPORT IN METAL OXIDE RESISTIVE SWITCHING DEVICES

By

PUNYA PRASAD MAINALI

Bachelor of Science in Physics
Trichandra College, Tribhuvan University
Kathmandu, Nepal
2014

Master of Science in Physics
Patan Multiple Campus, Tribhuvan University
Kathmandu, Nepal
2017
Oklahoma State University
Stillwater, Oklahoma
2020

Submitted to the Faculty of the
Graduate College of the
Oklahoma State University
in partial fulfillment of
the requirements for
the Degree of
DOCTOR OF PHILOSOPHY
December, 2022

CHARGE STORAGE AND TRANSPORT IN METAL OXIDE RESISTIVE SWITCHING DEVICES

Dissertation Approved:

David N. McIlroy, PhD
Advisor

Mario F. Borunda, PhD
Committee Member

Derek Meyer, PhD
Committee Member

Seok-jhin Kim, PhD
Outside Committee Member

.

ACKNOWLEDGEMENTS

First, I would like to thank my advisor Dr. David N. McIlroy for his continuous support and guidance that made this dissertation and my research work possible. His constant encouragement, advice, and support made me go through every single problem I faced during my research work. I cordially appreciate his transfer of knowledge during my Ph.D. research work. I would like to thank my advisory committee members, Dr. Mario F. Borunda, Dr. Derek J. Meyers, and Dr. Seokjhin Kim for their encouragement, creative comments, and questions.

Besides my advisory committee members, I would like to thank Dr. Elena Echeverria, Dr. Lyndon Bastatas, and Dr. Prasanna Sankaran who helped me get direction in my research work by instructing and encouraging me on using different techniques for the fabrication, characterization, and analysis of the data. I would like to thank Mr. Nishan Khatri who helped me draft this dissertation by proofreading and making necessary corrections to every single chapter. I would like to thank Mr. Phadindra Wagle for the countless hours of discussions that helped me not only generate ideas but solve problems related to my research work.

Last but not the least, I would like to thank my family, especially my parents for their struggle to make me achieve this milestone. I am indebted to my dear wife, Manisha Ghimire, for her constant support and motivation throughout my Ph.D. life.

Name: PUNYA PRASAD MAINALI

Date of Degree: DECEMBER, 2022

Title of Study: CHARGE STORAGE AND TRANSPORT IN METAL OXIDE RESISTIVE SWITCHING DEVICES

Major Field: PHYSICS

Abstract: Metal oxide resistive switching devices are designed and prepared using atomic layer deposition (ALD) and spin coating methods. The electrical and optical characteristics are studied for their applications in memory, photo-detection, and chemical sensing. Two electrically dissimilar ZnO thin film layers produced by using two different ALD recipes on a Si substrate as a bilayer is studied and found to have characteristics (rectification, hysteresis, and threshold voltage) needed to solve the crosstalk problem in crossbar memory array. ZnO bilayer device has fingerprint of a memristive device with AC frequency. The ratio of high to low resistive states (HRS/LRS) increases, reaches its maximum and starts to decrease with increasing frequency of applied AC voltage which is attributed to the diffusion dominating low frequency transport and charge freeze at high frequency. The maximum HRS/LRS achieved at 1 kHz is 2.3. Next part of the study deals with the α-Fe_2O_3 thin films on p-Si and glass substrates. α-Fe_2O_3 /p-Si samples show excellent ultra-fast visible light photo-detection property of response times under 10 μs with large zero bias photocurrent of >16 nA. The study of resistive switching properties of the α-Fe_2O_3 /p-Si samples reveals that it has synaptic potentiation property of neurons. The device's conductance increases with increasing voltage pulse applied to it and saturates at its maximum after some pulses. The mathematical hill function fit to the conductance data shows that activation of the device is programmable with the intensity of white light illumination. α-Fe_2O_3 /glass sample shows the coexistence of resistive switching and negative differential resistance phenomena in the presence of humid air with the transport analysis, it is attributed to the formation of the space charge at the material electrode interface. The same sample is used to quantify the relative humidity in air by using a novel sweeping I-V method.

TABLE OF CONTENTS

Chapter Page

LIST OF TABLES

Table Page

LIST OF FIGURES

Figure Page

Figure Page

Figure Page

Figure Page

CHAPTER I

INTRODUCTION TO RESISTIVE SWITCHING PHENOMENA

1. Introduction

Basic electronic circuits have three fundamental two terminal elements: resistors, capacitors, and inductors. These circuit elements have specific equations connecting underlying variables. For instance, Ohm's law connects Current and Voltage across a resistor($dV = R \times dI$). The basic circuit variables, current, voltage, charge and flux are linked to each other with specific equations and corresponding circuit elements. The link between flux and charge was missing until Leon Chua in 1971 theorized based on a symmetry argument that a fourth circuit element existed called a memristor [1]. The resistance of a resistor is independent of input voltage or current, but in the case of a memristor, the resistance depends not only on the applied input but on the history of applied input. Current and voltage are linked by a resistor, charge, and voltage by a capacitor and current and flux by an inductor. Chua realized that the link between charge and flux should exist in the form of a memristor, which is a short form of memory resistor; a resistor that adjusts its resistance depending on the history of applied voltage/current.

Fig.1.1 shows the schematic diagram of the basic circuit elements, circuit variables and their linked equations. The missing link is a two terminal circuit element that connects the flux and charge, similar to the resistor connecting current and voltage. The unknown in the figure is found to be a memristor. Regarding the I-V characteristics of the memristor, it must exhibit a pinched hysteresis loop [2]. Specifically, the current increases as the voltage increases, but when the voltage decreases, the current does not follow the initial path in reverse like a resistor obeying Ohm's Law. Instead, it traces a higher current path.

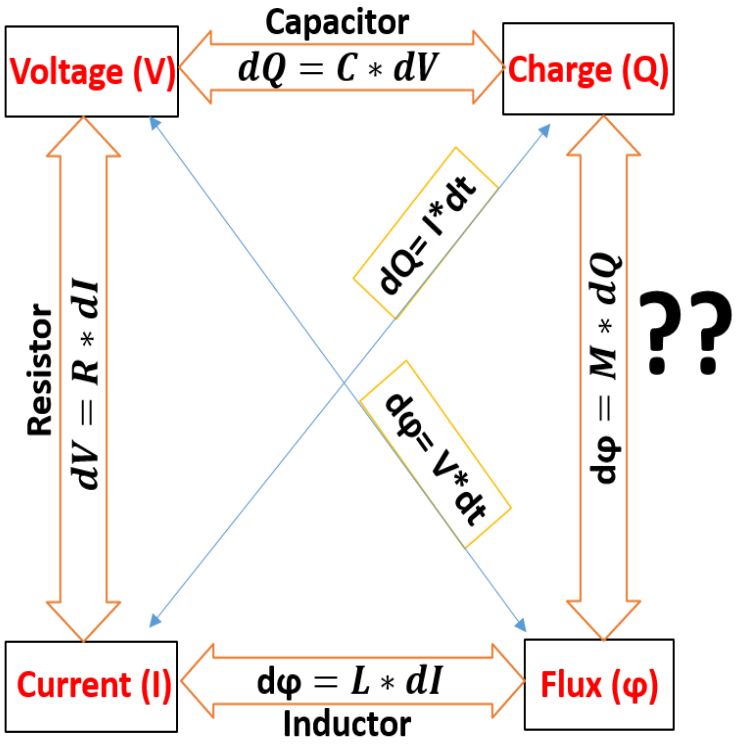

Fig. 1.1: Schematic diagram of basic circuit elements, the circuit variables and their linked equations. Question marks demand for a missing two terminal circuit element which was theorized to be memristor.

Fig. 1.2 illustrates the typical I-V characteristics of all the basic circuit elements [3]. A pure resistive device has a one-to-one correspondence between current and voltage, as shown in

top left corner I-V curve in Fig 1.2. Whereas the reactive devices (capacitive and inductive) have elliptical I-V curves that do not cross origin, which means the device stores some energy in the form of electromagnetic field (red and green I-V curves in Fig. 1.2). A memristive device has a characteristic pinched hysteresis loop, where the I-V curve always crosses origin (purple I-V curve in Fig 2), i.e., it does not store energy.

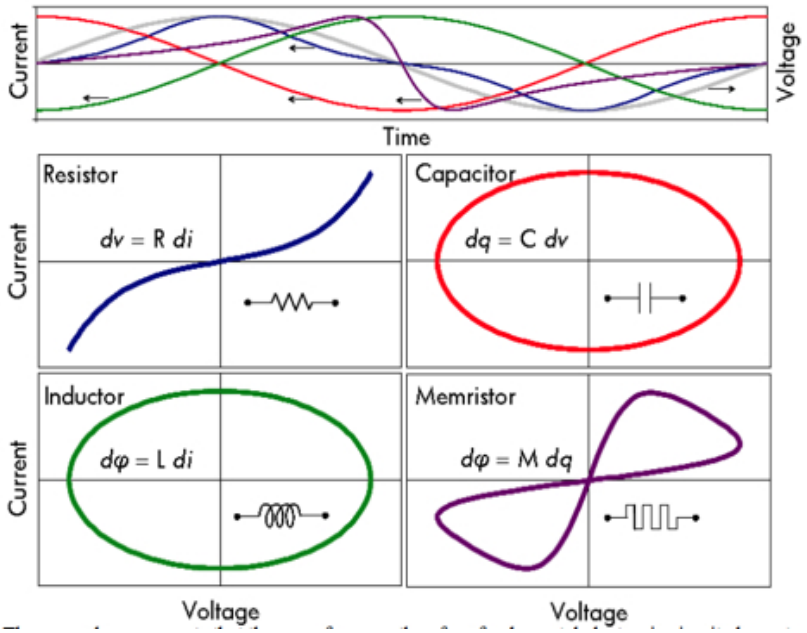

Fig. 1.2: Typical I-V characteristics of fundamental circuit elements. Fig. adopted from [3].

2. Resistive Switching Mechanisms

The fundamental structure of a memristive device is similar to a parallel plate capacitor, an active material layer sandwiched between bottom and top electrodes. The application of an electric field between the two electrodes induces a change in the active material layer that switches the device conductivity back and forth. Fig. 1.3 shows the fundamental structure of resistive switching devices.

There are several switching mechanisms [4], [5] for two terminal switching devices, where some of the more widely utilized mechanisms are discussed here.

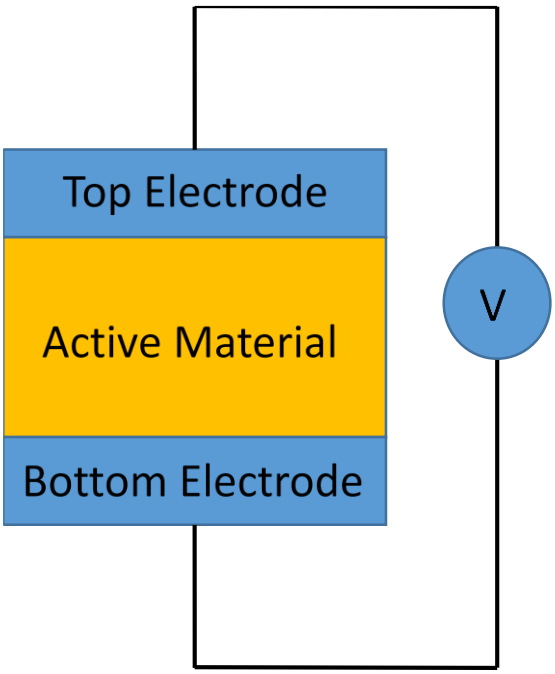

Fig. 1.3: Schematic diagram of fundamental memristive device architecture.

2.1. Electrochemical Metallization

Under the influence of the electric field applied across the active material, the vacancies, metal, or oxygen ions migrate towards one of the electrodes and form a conducting filament, there by switching from a higher resistive state (HRS) to a lower resistive state (LRS). Upon switching the polarity of the electric field, the filaments rupture, and the active material transitions from the LRS back to an HRS[6], [7]. Fig. 1.4 shows an example of formation and rupture of conducting filaments and the set and reset process.

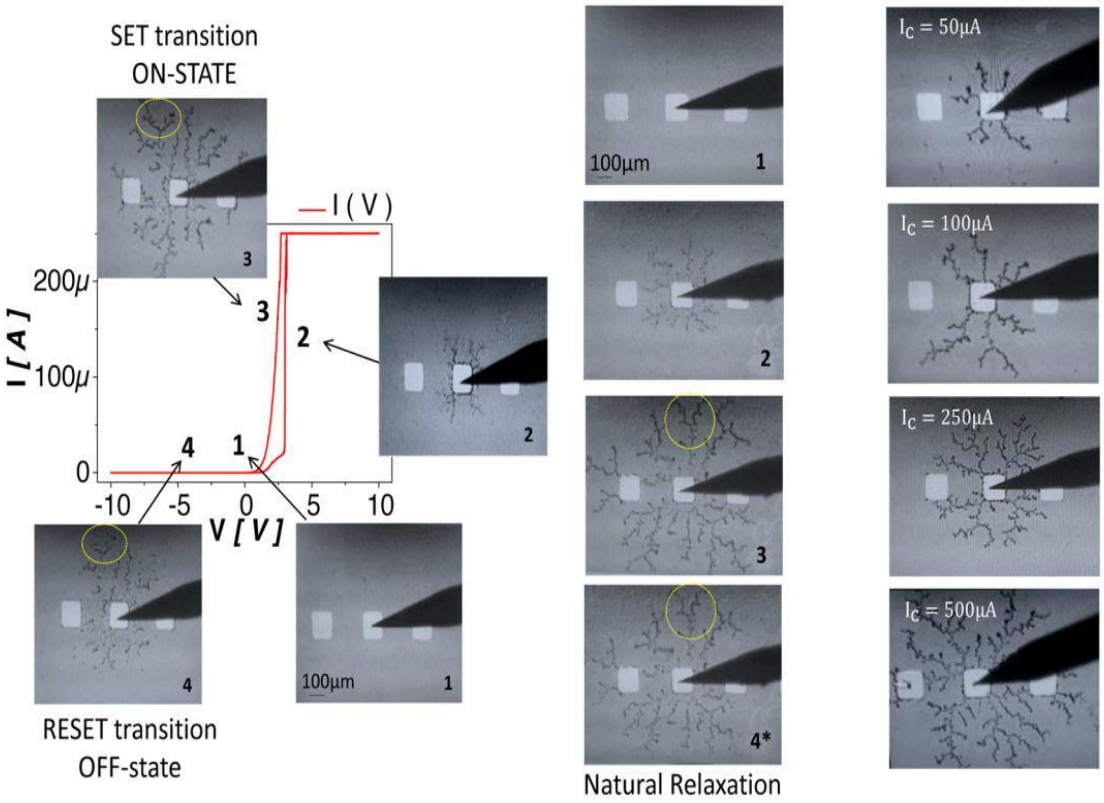

Fig. 1.4: Formation and rupture of conducting filament when the applied electric field is increased and the polarity reversed. Figure adopted from [7].

2.2. Ferroelectric Polarization Switching

Ferroelectric materials change their polarization when electric field is applied across it. Specifically, the polarization of the material changes from one state to another giving rise to different polarized material and, hence, switches from one tunnel resistive state to the another[8]. The material resets to the original polarization upon application of the reverse (negative) field. Therefore, the HRS and LRS take place in accordance with the switching of polarization state of the active material. Fig. 1.5(a) shows the schematic diagram of ferroelectric switching memristive device and Fig 1.5(b) shows the resistive state as a function of applied voltage.

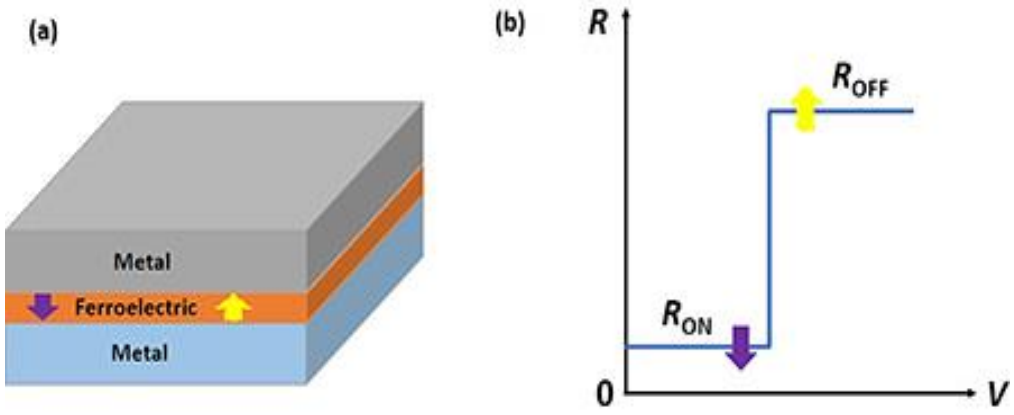

Fig. 1.5: (a) Schematic diagram for ferroelectric switching device. (b) The resistive states associated with the corresponding polarization in ferroelectric material.

2.3. Phase change Switching

Some materials[9], [10] structurally change from a crystalline phase to an amorphous phase upon applying a pulse of current. The as-grown active material is in the crystalline phase and a strong current pulse melts the material and establishes a region of amorphous phase, as shown in Fig. 1.6. The amorphous high resistance phase is programmable, and it is in the series with crystalline low resistance phase and effectively determines the overall resistance of the device[11].

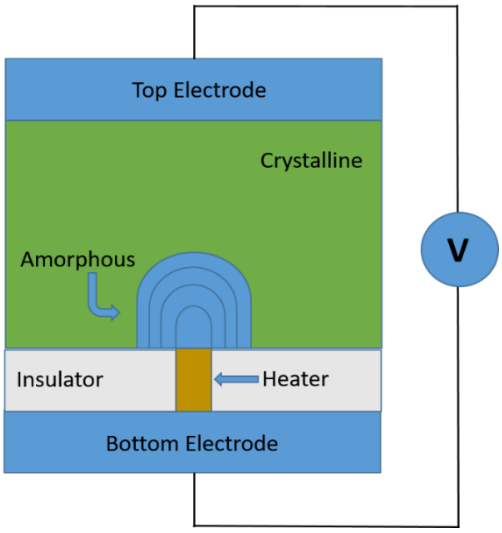

Fig. 1.6: Schematic diagram of phase change memory device. The amorphous phase shown is the active programmable region.

3. Applications of Memristive Devices

The experimental demonstration of memristive devices opened a new frontier for memory and in memory computing paradigm. Memristive devices are shown to have numerous and important applications [12], [13]. Some promising applications are discussed here.

3.1. Non-volatile Memory

The memristors retain their state until a reset pulse is sent. Memristors can store information for a long period of time without the need for external power. The information stored in the form of conductance state can be accessed after a very long time and at an ultra-fast rate. Due to its scalability, memristors are said to have potential to extend Moore's law.

3.2. Dynamic Load

The memristors have the ability to adjust their conductance in accordance with the applied voltage. This property can be applied to design electrical circuits using memristors as dynamic loads. For example, using memristive device, a programmable gain amplifier has been constructed [14] in which pulse program code sets the gain parameter. The same

property is applied to construct programmable switching threshold Schmitt triggers, programmable threshold comparator and programmable frequency relaxation oscillators [15].

3.3. Memristor aided logic gates

Memristors are used in logic gates (AND, OR and NOR etc.). Unlike traditional transistor-based logic gates, memristor uses only one input voltage but the inputs are determined by the initial state of the input memristors. The basic logic gates using memristors are called Memristor Aided Logic (MAGIC) [16].

3.4. Synaptic Devices and Neuromorphic Computing

The temporal dependence of the conductance change in memristive devices can be used to emulate synaptic behavior in neuromorphic systems. When a series of positive and negative pulses are sent through the memristive device, the conductance of the device is changed depending not only on the amplitude and polarity of the pulse, but also the temporal attributes. The time difference between the pulse and the width of the pulse effectively dictates the change in the conductance of the device, which directly emulates spike timing dependent plasticity (STDP) of a synapse [17]–[19]. The famous Pavlov's dog experiment that shows biological associative learning is experimentally demonstrated using memristive network[20], [21]. A single memristive device is shown to emulate the biological habituation/fatigue behavior of a synapse[22].

This research work addresses the materials design and fabrication for novel memristive systems and its applications in addressing crosstalk problem in crossbar memory arrays, photo detection, emulation of synaptic potentiation, and chemical sensing. An important electrical characteristic required to address the crosstalk problem in crossbar memory array is observed in bilayer ZnO device. A negative differential resistance with resistive switching

behavior is found to coexist in Fe_2O_3 material system in humid environment. This research work also discusses the application of resistive switching and negative differential resistance behavior found in Fe_2O_3 material system in quantification of relative humidity in the environment by applying a novel sweeping I-V method.

CHAPTER II

MATERIALS' PREPARATIONS AND CHARACTERIZATION

1. Materials' preparations

1.1.Fabrication of ZnO bilayer

The technique of atomic layer deposition (ALD) was used in the fabrication of ZnO thin films at low temperatures (<200°C), which results in a high density of defects [23]–[26], thereby making it an electrically conductive metal oxide. The ALD recipe controls the electrical and morphological characteristics of ZnO thin films[27]–[29]. In this work, two different ALD recipes were used to make electrically dissimilar ZnO thin films, ALD deposition was performed in an Okyay Technologies ALD system. The films were deposited on a Si (100) substrate with native oxide at 180 ^{o}C under a constant flow of N_2 (15 sccm) using diethyl zinc (DEZ) and DI water as the Zn source and oxidizer, respectively. The ALD was operated in 'soak' mode for the bottom layer where the precursors were allowed to remain in the reactor for a predetermined time prior to pumping down the reactor. Soaking increases the deposition rate, such that it is no longer true ALD. A 'soak' deposition cycle consisted of a 100 ms dose of DEZ, soak for 20 s, pump down for 35 s, then a 15 ms dose of DI water, soak for 20 s, followed by a pump down for 35 s before beginning the next cycle.

The ZnO deposition rate with soaking was 2.2 Å/cycle. The top ZnO layer was deposited using a standard ALD cycle, sans soaking. In this case, a deposition cycle consisted of a 100 ms dose of DEZ (100 ms), pump down for 20 s, and then a 15 ms dose of DI water, followed by a pump down for 10s before beginning the next cycle.

This results in a deposition rate of 1 Å/cycle. Here, the higher deposition rate with soaking produces ZnO films with morphologies and resistances differing from films without soaking, which is addressed in the succeeding sections. The bottom ZnO layer was annealed at 300 ^{o}C in a tube furnace in an ambient atmosphere prior to the deposition of the top layer. The rationale for annealing is provided in later chapters. The two dissimilar ZnO form a bilayer ZnO homojunction memristor.

1.2. Fabrication of Fe_2O_3 thin films

The α-Fe_2O_3/p-Si samples were prepared using an organic iron solution consisting of 0.1 and 0.5 grams powder of Fe (III) Acetylacetonate (Strem Chemicals CAS#: 14024-18-1) in 10 ml (10g/L and 50 g/L) solutions of acetone (28 mM and 141 mM). The solution was sonicated for an hour, followed by vortex stirring and filtering. Approximately 10 µL of the solution was spin-coated onto a p-Si (100) and glass substrates at 3000 rpm. The solvent was allowed to evaporate and then the sample was annealed in air at 500°C for 1 hour inside a tube furnace and then allowed to slowly cool to the room temperature to avoid cracking of the α-Fe_2O_3 film. Circular gold electrical contacts with an approximate area of 0.071 cm^2 were sputtered onto the sample using a shadow mask. The sputter chamber was held at a pressure of 10 mTorr of Ar and deposition was carried out with a plasma power of 25 W. The samples were then annealed at 300°C in the air for 45 minutes to form good electrical contact between the Au electrodes and the Fe_2O_3 films.

2. Materials' characterization

This section briefly discusses the materials characterization techniques. X-ray photoelectron spectroscopy (XPS) was used to study the elemental composition and relative non-stoichiometric oxygen content present in the ZnO samples. The basic working principle, instrumentation, and specific application of XPS related to this research work is explained in section 2.1.

Scanning electron microscopy (SEM) was used to study sample morphology. In particular, the morphology of two different ZnO thin films and Fe_2O_3 microcrystalline thin films. The basic working principle, parts and instrumentation and specific application applied in this dissertation are presented in section 2.2. Sections 2.3 and 2.4 review the techniques of energy dispersive x-ray spectroscopy (EDX) and Raman spectroscopy, their basic working principles, and the specific applications peculiar for this study.

2.1.X-ray Photoelectron Spectroscopy (XPS)

The working principle of XPS is based on the theoretical photoelectric effect explained by Albert Einstein in 1905 [30]. X-ray photons with characteristic energy (usually Mg Kα,1253.6 eV or Al Kα, 1486.6 eV radiations) are impinged upon the surface of the sample, thereby exciting core level electrons of an atom into the vacuum level, where these excited electrons are called photoelectrons. The photoelectrons are collected and their kinetic energy measured and recorded by an electrostatic electron energy analyser. Equation 2.1, Einstein's photoelectric equation based on conservation of energy [31], is the relationship between the binding energy (E_B) of the electron in an atom, the kinetic

energy (E_K) of the free electron (photoelectron) in the vaccum and the energy of the photon (X-ray) used to create (excite) the photoelectron [32]:

$$h\upsilon = \phi_s + E_B + E_k \quad (2.1)$$

In equation 2.1, h is the Planck's constant, υ is the frequency of incident X-ray photon, E_B is the binding energy of the atomic orbital in which the electron resided in the atom, E_k is the kinetic energy of the photoelectrons, and ϕ_s is the effective work function between the sample and the electrostatic electron energy analyzer. Each atom in its particular oxidation state has its own unique signature binding energies of electrons. The elemental binding energy varies because of the chemical state and polarizability of the element, therefore one can get direct information about the chemical state of the element from the binding energy shift relative to its pure form. The photoelectrons with kinetic energy in the range 50-100 eV have a mean free path (path length through the material without scattering) in the order of few angstroms. Consequently, only photoelectrons originating from atoms within the first few layers of surface of the sample escape into the vacuum level and subsequently analyzed by electrostatic electron energy analyzer. Typically, XPS can be used to probe a depth of 8nm – 10nm into a sample [33]. Therefore, XPS is an excellent tool for probing the surfaces of materials [34].

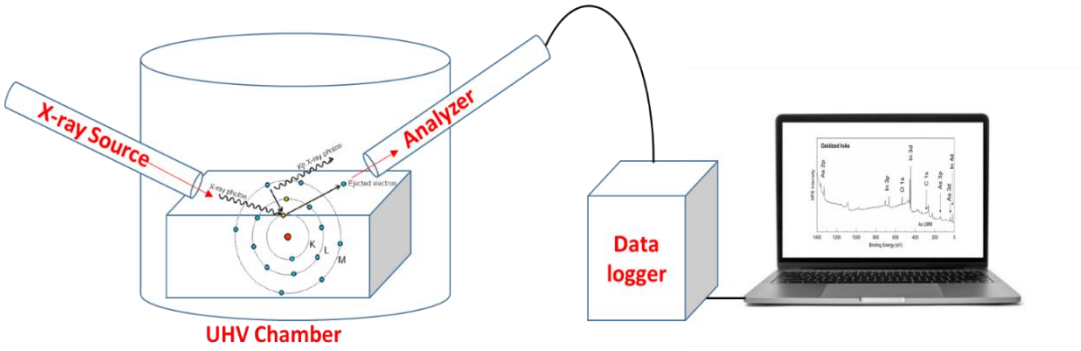

Fig. 2.1: Schematic diagram of XPS components, working principle and the data acquisition system.

XPS measurements must be performed in ultra high vacuum (UHV) conditions with pressures of ~10^{-10} Torr in order to protect the samples from contamination, false reading of photoelectron energies, and excessive scattering of the photoelectrons by molecules in the atmosphere [35]. Fig. 2.1 shows the schematics of the XPS parts along with the working and the data acquisition system. The photoelectrons ejected from the surface of the sample are collected and analysed by the analyzer. The data are transferred to the computer through the data logger and the data analysed accordingly.

In the present work, XPS was carried out at room temperature in a UHV chamber with a base pressure <$8x10^{-10}$ Torr. The XPS spectra were acquired with the Al-Kα emission line from a dual anode X-ray source (Physical Electronics XR 04-548) operated at 400 W and an incident angle of 54.7° and normal emission. The photoelectrons were collected and analyzed with an Omicron EA 125 hemispherical electron energy analyzer with an energy resolution of 0.02 eV. Subsequently, the data was analyzed using the CasaXPS software package [36], [37] where a Shirley background was subtracted from the core level spectra presented herein [38]. In this study, XPS analysis has been used to map the

relative concentrations of stoichiometric (O^{2-}) and non-stoichiometric ($O^{(2-\delta)-}$) oxygen (δ is a positive fraction) present in the the two electrically dissimilar ZnO thin films grown on the Si(100) substrates. The core level spectra are deconvoluted with Voight functions centered at binding energies of 531.0 eV (O^{2-}) and 532.5 eV ($O^{(2-\delta)-}$). The areas under their respective curves are relative quantitative concentration of defects or non stoichiometric oxygen present in the two types of ZnO. The XPS analysis of the two electrically dissimilar ZnO thin films are presented in chapter III.

2.2.Scanning Electron Microscopy (SEM)

Scanning electron microscopy was used to study the surface morphology and the average crystalline size of the materials used in this dissertation. The SEM rasters a focused beam of electrons across the surface of the sample and reconstructs the backscattered electrons into an image of the sample surface. A typical SEM system is comprised of four essential components; an electron source or gun, specimen stage, secondary electron detector and imaging/display system [39]. The electron gun consists of a low work function thermal emission filament, high voltage elements to accelerate the electrons, condenser lenses to focus the beam, and a deflection system consisting of electric coils for rastering the beam across the sample [40]. The sample is placed on a specimen stage with three axes of translation and one degree of tilt. The SEM system operates inside a vacuum chamber. The schematic diagram of SEM system is shown in Fig. 2.2.

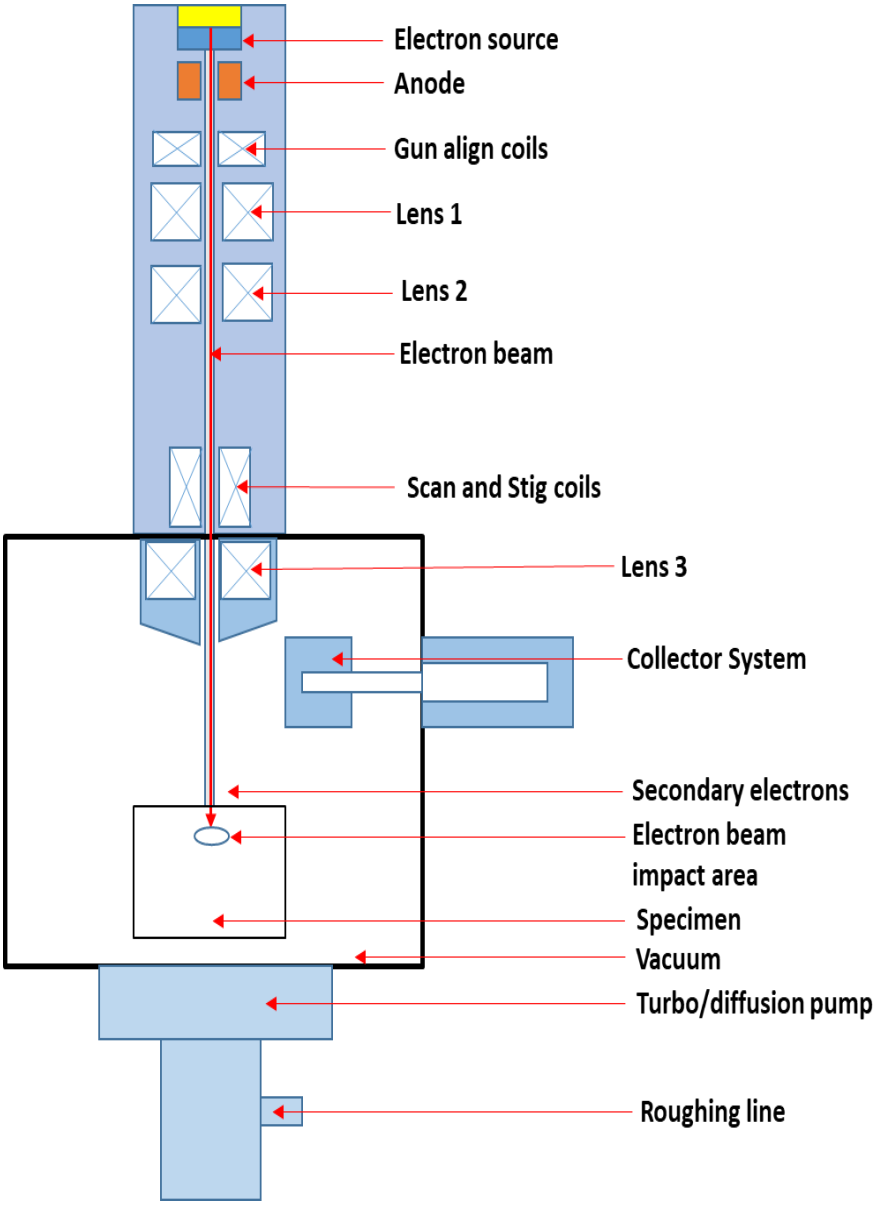

Fig.2.2: Schematic diagram of scanning electron microscopy (SEM)

A high energy (0.1-30 KeV) electron beam is produced from the electron gun condensed by the lens system interacts with the sample and produces the backscattered and secondary electrons which are detected by the detector. The scanning coils move the electron beam from point to point until a rectangular image of the scanned area is formed.

The spot size of electron beam can be < 10 nm implying the resolution of SEM can be < 10 nm and the depth of penetration into the sample is around 1μm [41].

In the current study, SEM images of samples were acquired with a FEI scanning electron microscope at different magnifications. The analysis of the image was done using ImageJ software. SEM micrographs provided the insight into the sample morphology and the average size of the polycrystalline ZnO, the average size of the voids in the sample surface, etc. In the case of Fe_2O_3 samples, SEM micrographs provided the overall distribution of the microcrystalline particle assembly as well as revealing the discontinuous nature of the films. The overall elemental distribution of Fe and O in the Fe_2O_3 microcrystalline particles with EDX analysis, discussed in the next section. The detailed results are discussed in the respective chapters.

2.3.Energy Dispersive X-ray Spectroscopy (EDX)

Most SEM systems are equipped with the EDX analysis system. When high energy electrons strike an atom, an electron from a core level state can be excited into the vacuum, much like in photoemission, leaving a positive hole in its place. An electron from higher energy level decays to fill the hole, giving out an x-ray radiation equal to the energy difference between the two energy levels, i.e., conservation of energy. The x-ray radiation is detected and analyzed by EDX system [42]. The energy of the x-ray emitted from the atom is unique to that atom, therefore it can be used to analyze chemical information of the sample.

EDX can be used for qualitative and quantitative analysis of the sample. One can identify the presence of certain elements, the percentage of the elements present in the specimen and the overall distribution of the elements[43].

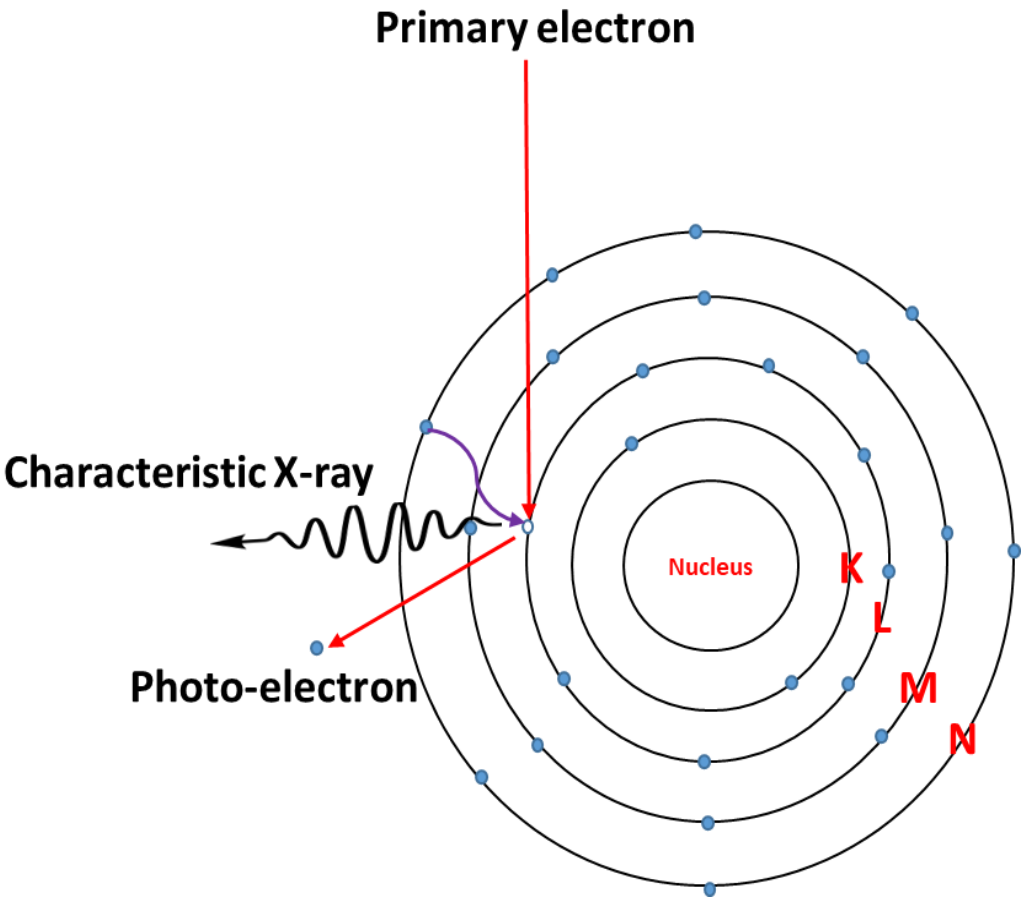

Fig.2.3: Schematic diagram of characteristic x-ray production in EDX system.

In this study, an EDX system from Bruker Nano Berlin, Germany with primary energy of 10keV, take off and azimuth angles of 35° and 45°, respectively, was used to analyze sample. The detailed results and discussion can be found in chapters IV and VI.

2.4. Raman Spectroscopy

With Raman spectroscopic analysis or Raman spectroscopy, a sample irradiated with a monochromatic laser that emits in the UV-visible region of the light spectrum [44]. The incident light scatters due to interaction with different vibrational modes of molecules or a material. The back-scattered light having the same wavelength as the incident light is said to undergo Rayleigh scattering and is the strongest scattered light. However, a small fraction of light undergoes scattering at a different wavelength that depends on the chemical structure of the molecule or material. This is called Raman scattering, which are further divided into Stokes and Anti-stokes scattering with frequencies $\upsilon_0 - \upsilon_m$ and $\upsilon_0 + \upsilon_m$ respectively. Here, υ_0 is the frequency of incident light and υ_m is the frequency of vibrational mode of a molecule or material and is a signature of the chemical state of the scatterer [45].

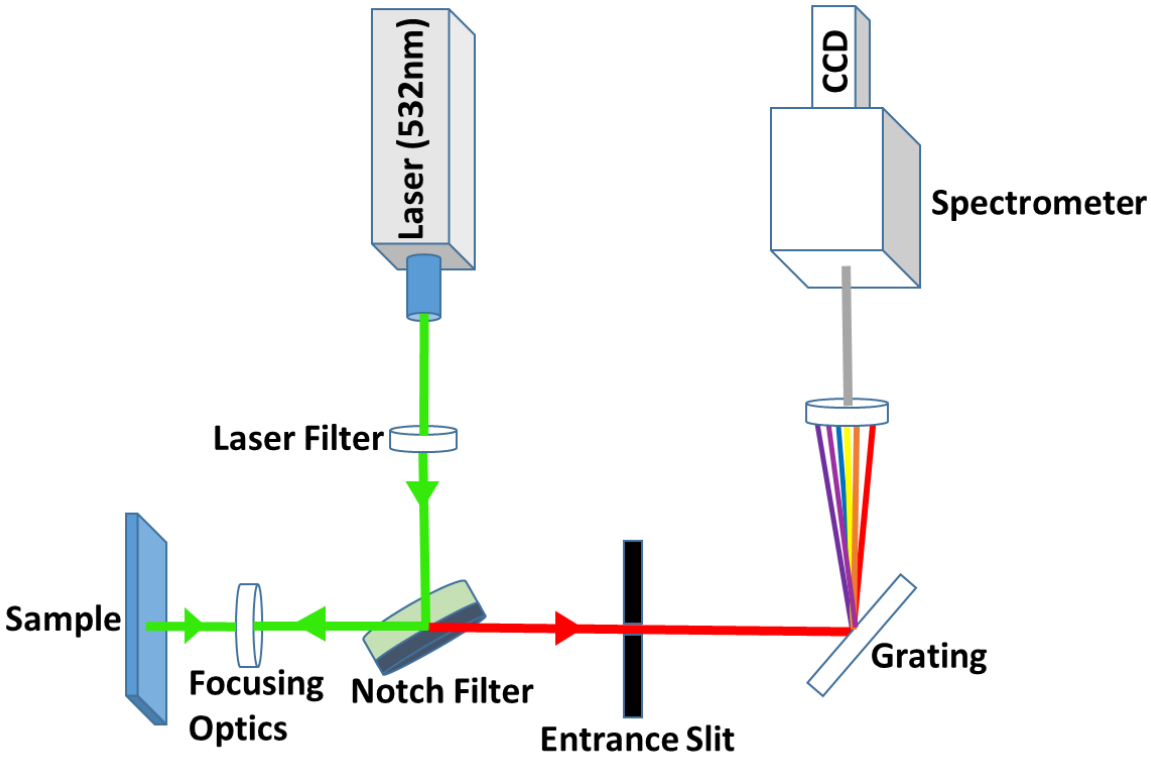

Fig.2.4: Schematic diagram of Raman spectroscopy system.

Fig. 2.4 shows the schematic diagram of a typical Raman scattering system. A 532 nm green laser source was used to acquire data for this dissertation. The incident laser is sent through a collimator, focused through the optical lenses and onto the sample. The back-scattered light from the sample is collected through a notch filter that rejects the primary frequency used to irradiate the sample, thereby filtering out Rayleigh scattered light from entering the spectrometer. The spectrometer collects only stokes and anti-stokes scattered light. From the frequency of stokes or anti-stokes light, the frequency of the vibrational modes of a molecule or material are identified using known standards or reference work.

Raman spectra were acquired with a WITec alpha 300R Raman microscope, equipped with a 532 nm laser. Raman spectrum was collected using a 100× objective lens of 0.9 numerical aperture, 600 lines/mm grating, and 100 μm confocal aperture (fiber) diameter

to identify the presence of α-Fe_2O_3 in the sample. The presence of signature peaks that corresponds to the phonon and magnon vibration modes of α-Fe_2O_3 in the Raman spectroscopy data is clearly observable. This study attempts to show the increment of film thickness with the increment of solution concentration used to fabricate the sample by showing the attenuation in the Raman peak of the Si substrate.

3. Electrical characterizations

To elucidate electrical properties of the samples produced in this dissertation, four different instruments were used for electrical characterizations. A Keithley 2425 source measure unit (SMU) for DC measurements, a PXIe data card for AC measurements, a Moku Lab lock-in amplifier for zero bias photocurrent and BK precision LCR meter model 891 for capacitance measurements were utilized in this study. Custom Labview programs were written by the candidate for data acquisition with all instruments, with the exception of the Moku Lab lock-in amplifier, which comes with its own iOS application.

3.1.Four Point Probe Resistivity

The sheet resistivity (ρ) of a thin film can be measured using a four-point probe method. With this method, four identical and collinear probes are attached with equally spacing between them on the sample, which typically is a thin film. The current is sent through the outer two probes and voltage is measured across the inner two probes, as shown in Fig. 2.5, where I_s and V_m are the sourced current and measured voltage, respectively. The resistivity is calculated using equation 2.2, where k is geometrical correction factor that depends on the tip diameter and wafer diameter, t is the thickness of the sample. For spacing of probes $d >> t$, the correction factor k approaches unity [46], [47], [48].

$$\rho = k\frac{\pi}{\ln(2)}\frac{V_m}{I_s}t \qquad (2.2)$$

The Keithley 2425 SMU is used to source the current, I_s, between the outer probes and measure the voltage difference, V_m, between the two inner probes.

In the current study, the resistivities of the samples were measured as a function of post growth annealing temperature. The samples were annealed at different higher temperatures, brought back to room temperature and then the resistivity was measured. The process continued for subsequent higher temperatures. The result of the resistivity measurement is presented in the electrical characterization section in Chapter III.

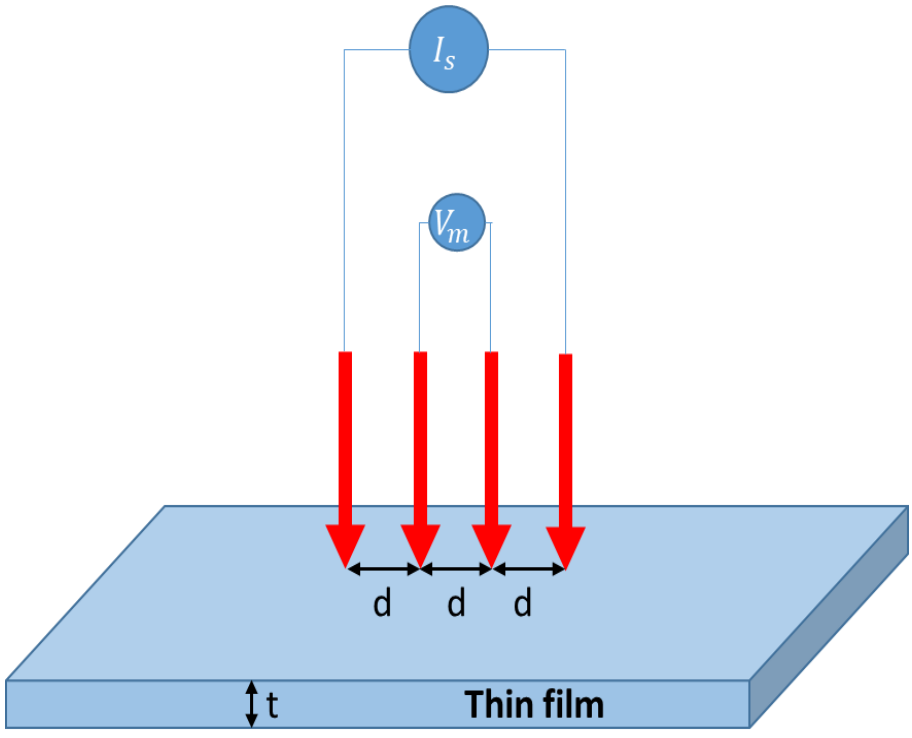

Fig.2.5: Schematic diagram of 4-point probe resistivity measurement setup.

3.2.Voltage divider circuit and AC I-V measurement

The AC electrical properties of ZnO homojunction diodes were evaluated by applying AC voltage and measuring the current using a voltage divider. The measurement circuit consisted of a resistor (275Ω) in series with sample. Fig. 2.6(a) shows the schematic diagram of ZnO bilayer device geometry and the gold probe connected on layers to make the electrical measurements. Fig. 2.6(b) is a voltage divider circuit designed to make AC electrical I-V measurements, where V_{in} and V_1 were measured simultaneously and fed into the post processing using a custom Labview program.

A PXIe 6349 data card from National Instruments interfaced in conjunction with Labview was used for data acquisition. The custom designed Labview program further processes the data using the equations 2.3 and 2.4 to retrieve voltage and current in the sample, respectively.

$$V_{sample} = V_{in} - V_1 \tag{2.3}$$

$$I_{sample} = \frac{V_1}{R} = \frac{V_1}{275} \tag{2.4}$$

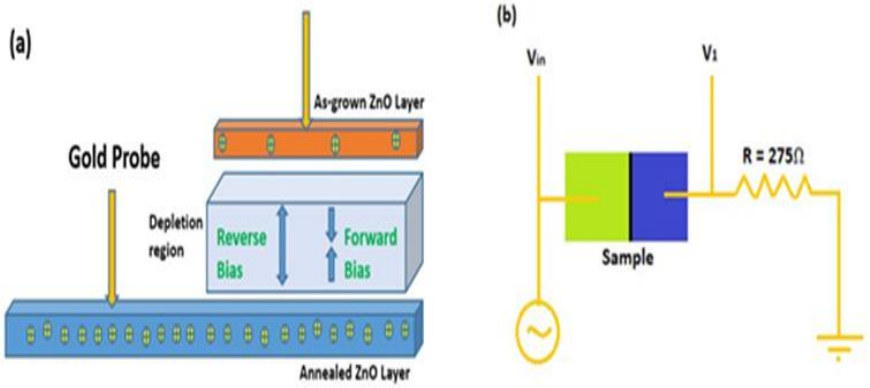

Figure 2.6: (a) Schematic diagram of ZnO bilayer memristor design and geometry, (b) the circuit diagram of the test setup for AC electrical measurements, where V_{in} and V_1 are simultaneously recorded.

3.3.Zero bias photocurrent and responsivity measurement

One of the characteristics of α-Fe_2O_3/p-Si device is its large zero bias photocurrent. The zero-bias photocurrent and the rise and decay time of response were measured with a Moku Lab (Liquid Instruments Inc. California) lock-in amplifier and Tektronix arbitrary function generator (AFG 31052). The AFG generated pulses at a frequency of 11.897 kHz (a prime number frequency that has a period close to 100 µs) with a 10% duty cycle, 1.5 V amplitude, for driving the white LED used as the light source, as well as the reference input to the lock-in amplifier. The Lock-in amplifier measured the voltage across a resistor (R=1.98 MΩ) connected across the photodetector and post-processed the data to give photocurrent. To measure the responsivity as a function of wavelength of light, a solar simulator (Model 66002, Oriel Corporation) was used as a source, which was fed into Monochrometer (Jarrell-Ash) and output light of which was incident on the sample. The power of light was measured using a Thorlabs PM400 optical power meter.

Fig. 2.7 shows the schematic diagram of the experimental setup for the measurement of zero-bias photocurrent and the actual geometry of the sample inside the dark box.

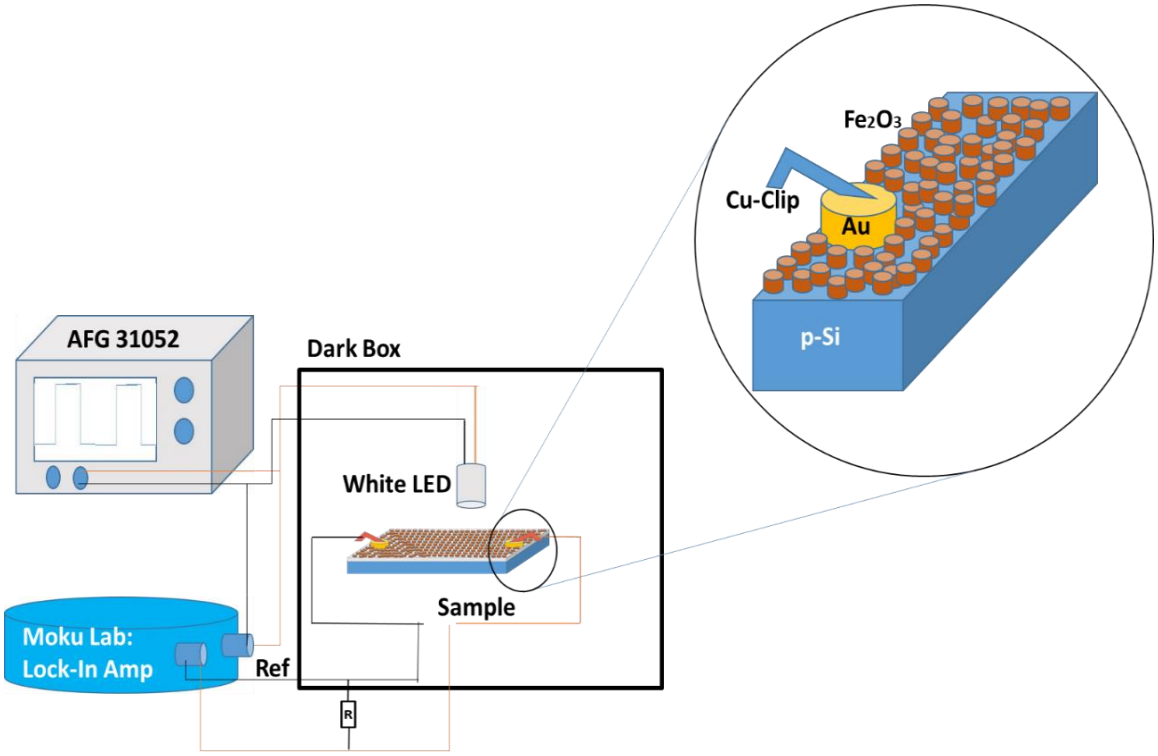

Fig. 2.7: The schematic diagram of the setup for the measurement of zero-bias photocurrent and the time of rise and decay using Moku Lab lock-in amplifier. Function generator AFG 31052 generates pulse of 1.5 V amplitude that drives the white LED on surface of the sample. Zoomed in is the schematics of the sample inside the dark box.

3.4.Synaptic conductance measurement

In order to observe the synaptic potentiation in an α-Fe_2O_3/p-Si device, the conductance as a function of voltage pulses was measured. For this measurement, a Labview program programmed the Keithley 2425 SMU to source a pulse (amplitude, pulse period and width) and measure the conductance when the pulse arrived. A 5 V pulse with 100 ms period and 10 ms width was sent through the device and the conductance was measured

when the voltage reached 5V. For α-Fe_2O_3/glass samples, measurements were conducted in a humid environment (humidity sensing) with a pulse width of 200 ms and a period of 1 s.

3.5.Electrical measurement of humidity sensor

The resistance of humidity sensors was acquired using a Keithley 2425 SMU simultaneously applied a 5 V source voltage and measured the current through the sensor. Once again, a custom Labview program was used for data acquisition and control of the Keithley 2425 SMU. The relative humidity inside the chamber was monitored using a flow meter from CompuFlow, model 8585. Real time capacitance was measured using a BK precision LCR meter model 891 by applying a 1 kHz and 1 V rms signal through the sensor and taking the average of 500 data points at a particular humidity level.

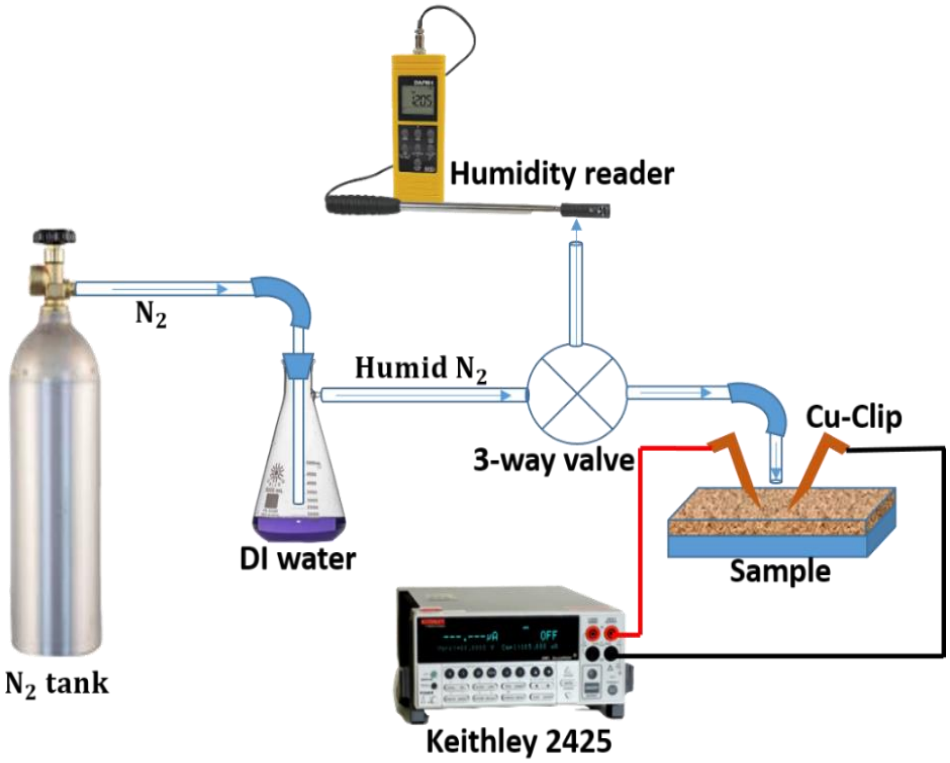

Fig. 2.8: Schematic diagram of the sensor experiment setup (not to scale) where the humid air is produced by bubbling nitrogen gas through a conical flask of DI water. The 3-way switch is manually operated for turning on and off humid air onto the sample.

Fig. 2.8 shows the schematic diagram of the resistance response measurement of the humidity sensor by applying a humid N_2 flow on the sensor and measuring the change in the resistance. The humid N_2 flow was prepared by bubbling dry N_2 into a conical flask filled with DI water which is shown in fig. 2.8. The dry N_2 pressure, temperature at which the conical flask with DI water is heated, controls the amount of water vapor carried by the N_2 gas or the humidity onto the sample. Copper clips were used as contacts because its work function is close to the electron affinity of α-Fe_2O_3 [49], [50].

CHAPTER III

CROSSTALK IN CROSSBAR MEMORY ARRAY AND ZnO HOMOJUNCTION DIODE

1. Introduction

One of the major difficulties faced in crossbar array-based memory devices is "crosstalk" between adjacent cells [51]**,** where crosstalk refers to the backflow of current that alters the state of adjacent cells and subsequently leads to an incorrect reading of the cell's state. To avoid the crosstalk problem, a one-diode-one-resistive-switch (1D1R) model is proposed [52]**,** which is a series combination of a diode and a memristor (resistive switch). The problem is further complicated by the fact that digital memory, memristive or not, is for all intensive purposes, an AC circuit of memory bits that are being accessed at very high rates. This leads to capacitive coupling that adversely impacts the operating speed of the device. As a consequence, memristor design is not solely an architectural challenge, but also a materials' challenge, i.e., identifying materials and combinations thereof that produce memristors with optimal balance of performance and stability. Materials' challenges for the resistive switching devices in RRAM are mostly the spatial (device to device) and temporal (cycle to cycle) stochasticity. Spatial stochasticity arises mainly due to the lack of consistency in the materials fabrication process, leading to variability of electrical characteristics from device to device [53], [54], [55].

Atomic layer deposition (ALD) of ZnO provides precise control of the film properties, such as preferential direction of growth [27], morphology, electrical/optical properties [28] and roughness [29], which are influenced by the growth temperature, ALD soak time and the ratio of precursor purge. Since Al doped ZnO is found to have minimized temporal stochasticity and sufficient endurance characteristics[56], ALD synthesized ZnO has potential for RRAM applications.

There are several studies in ZnO based heterojunction memristors [57],[58] in which two or many different material layers are fabricated and studied. A single layer of ZnO on stainless steel using the gold electrode exhibited characteristics of resistive switching [59]. In thin film ZnO resistive switching devices, it is oxygen vacancies and interstitials that are the primary participants in the resistive switching process [60]. Therefore, through judicious control of the density of oxygen defects in a ZnO thin film, one can construct a double layer homojunction resistive switch device. In effect, different concentrations of defects in two different layers form a homojunction at the interface. This study focuses on the electrical properties showing memristive diode behavior of the double-layered structure having potential applications as 1D1R replacement using the same material.

2. Results and Discussion

2.1.Morphology and Stoichiometry

In order to produce a homojunction memristor, the electrical properties of the two ZnO layers need to differ from one another, such that a depletion layer forms at their interface [61]. This is achieved by controlling their morphology and stoichiometry. Low temperature ALD grown ZnO films have a high density of defects and nanocrystalline

structure[23], [24]. Consequently, deposition rate and thermal annealing of ZnO are variables that can be used to tune the electrical properties of ZnO films and are the approaches utilized in this study to construct the ZnO homojunction memristors. Displayed in Fig. 3.1 are SEM images of the two ZnO layers of the memristor. The contrast of the morphologies of the two layers is apparent at the boundary between them in the SEM image in Figure 3.1(a). The morphology of the first ZnO layer (Fig. 3.1(b)) can be described as a mosaic of ZnO domains with an average diameter of 40 nm separated by on average 15 nm wide voids. It is observed that annealing of the first ZnO layer at 300 ^{o}C had no effect on its morphology (not shown). In contrast, the morphology of the second ZnO layer (Fig. 3.1(c)) consists of large crystals of ZnO with an average length of 115 nm. We attribute the differences between their morphologies to their different deposition rates. Specifically, the deposition rate of 2.2 Å/cycle for the first ZnO layer, as opposed to 1 Å/cycle of the second layer, impedes nucleation of large ZnO crystals in favor of a smoother surface. Also, the voids in the first layer are an order of magnitude smaller than the voids between the ZnO crystals in the second layer.

The stoichiometry of the two ZnO layers have been determined by XPS by measurement and analysis of the Zn 2p and O 1s core levels states, which are displayed in Fig. 3.2. Based on wide XPS scans of the two layers, the calculated atomic percentage ratios of Zn:O are 0.83 and 1.09 for the first and second layers, respectively. The absence of large ZnO crystallites in the SEM image of the first layer (Fig. 3.1(b)), in conjunction with a Zn deficiency, is indicative of highly disordered ZnO and attributable to the high deposition rate of 2.2 Å/cycle. The 1:1 ratio of the top layer is consistent with the observation of large ZnO crystals in Fig. 3.1(c).

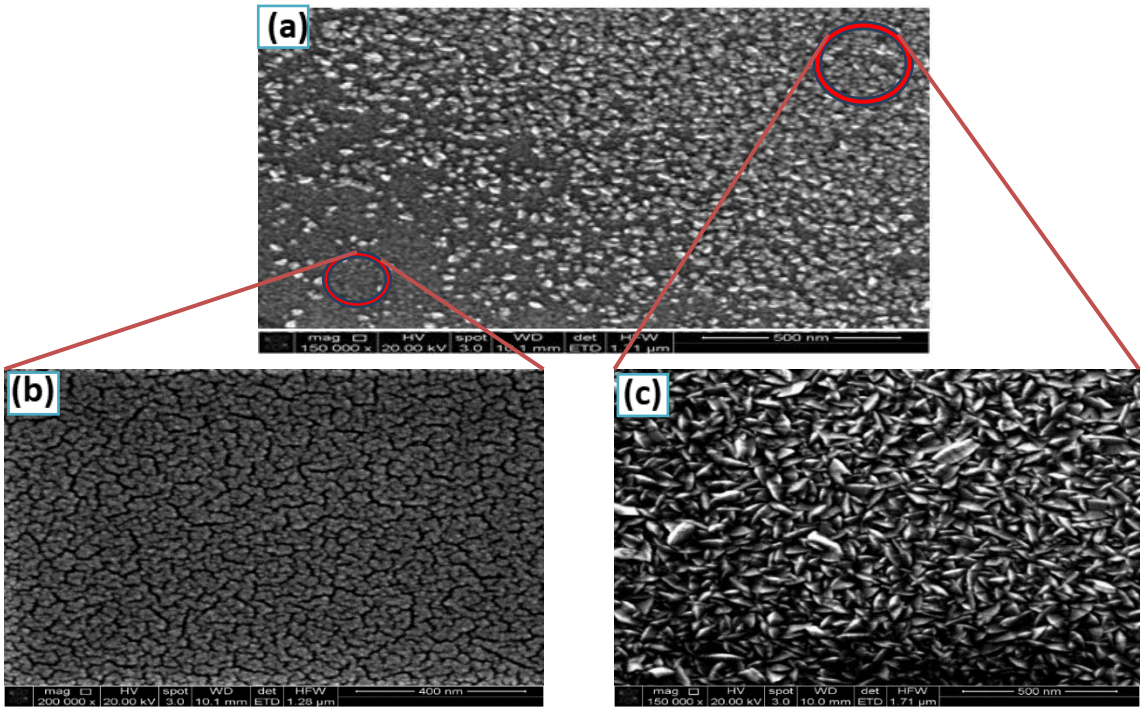

Figure 3.1: SEM images of (a) the boundary between the two layers (b) annealed (300^{o}C) base/first layer and (c) the as-grown top/second layer.

The Zn 2p spectra for of the two layers in Fig. 3.2(a) are almost indistinguishable and, therefore, do not reflect their different morphologies. In contrast, the O 1s core level states of the two layers in Fig. 3.2(b) exhibit distinguishable differences that reflect their different stoichiometries and morphologies. Both have spectral weight at a binding energy of 531 eV that is indicative of O^{2-} and stoichiometric ZnO[62], as well as a spectral weight at ~532.5 eV. We propose that the intensity of the higher binding energy feature of the O 1s can be used as a measure of the relative disorder of the ZnO layer, i.e., $O^{(2-\delta)-}$, where δ is a positive fraction. To quantify the degree of disorder, the O 1s core level states for both layers were fit with two Voight functions, where the FWHM of the

peaks were held equal. The results of the fits for the annealed first layer and the second as-grown layer of ZnO are displayed in Figs. 3.2(c) and (d), respectively. The ratio of the area of the peak at ~532.5 eV to the peak at 531 eV is 1.16 for the first layer, and 0.51 for the second layer, and 0.42 for the single crystal reference (not shown here). The O 1s ratio of the second layer of ZnO of 0.51 is essentially identical to that of the ZnO single crystal. This ratio and the observation of ZnO crystals in the SEM image of the second layer in Fig. 3.2(c) support the conclusion that the second ZnO layer has a low concentration of defects. In contrast, the ratio of 1.16 for the first ZnO layer, along with the lack of large ZnO crystals, suggests that it has a much higher concentration of defects relative to the second layer and the ZnO single crystal. Therefore, we conclude that the first ZnO layer is highly disordered as a consequence of the high deposition rate of 2.2 Å/cycle, as compared to 1 Å/cycle for the second layer.

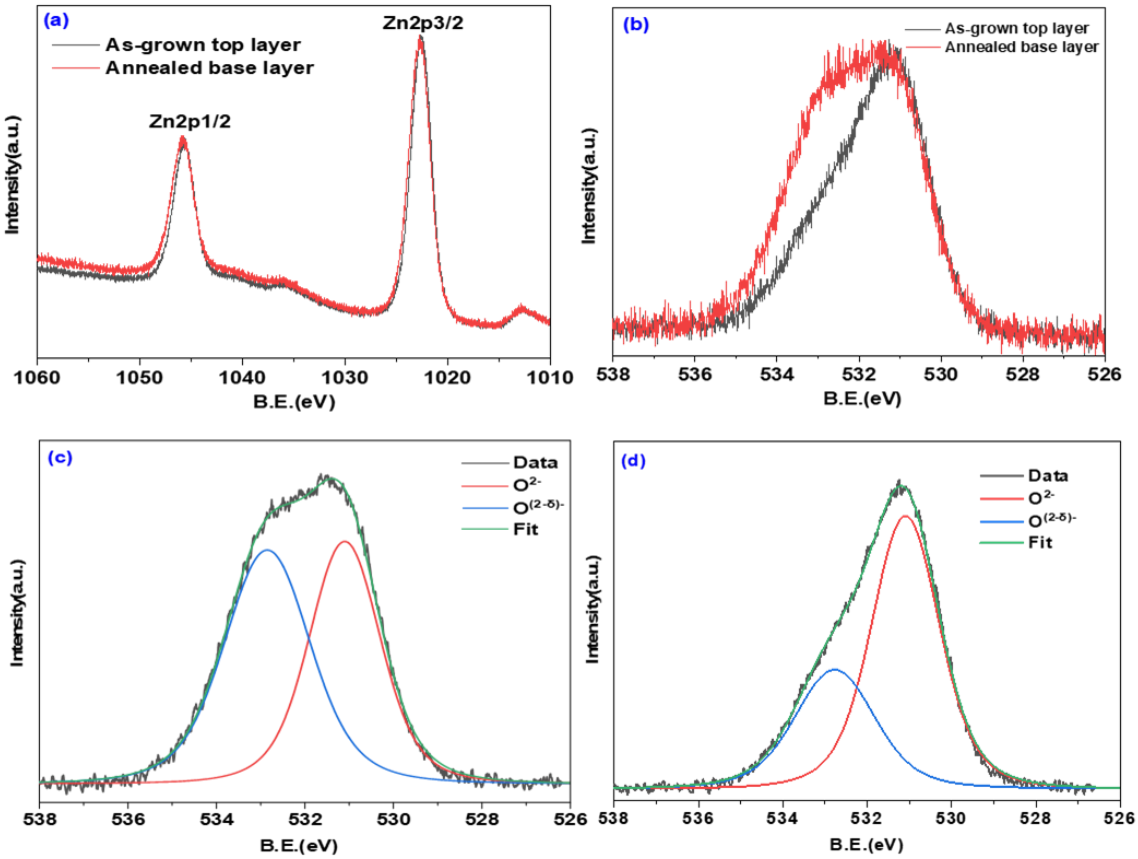

Figure 3.2: (a) The high resolution XPS data for Zn 2p (b) O1S core level data and deconvolution fits for (c) annealed first ZnO layer and (d) as grown second ZnO layer.

2.2.Electrical Characterizations

As-grown low temperature ALD ZnO (T< 200 ^{o}C) is highly conductive due to a high concentration of defects [24]–[26], but the conductivity can evolve over time due to the self-healing characteristics of ZnO [63]. Consequently, the best practice is to post-anneal the films, thereby producing a less conductive (higher resistivity) but more stable ZnO film. Furthermore, the results obtained indicate that a moderately resistive ZnO is desirable for constructing ZnO homojunction memristors. The resistivity vs. post-annealing temperature of a ZnO film grown using the conditions for the first layer is displayed in Fig. 3.3. The sample was annealed at successively higher temperatures at

twenty minutes intervals, where between each interval it was brought back to room temperature and its resistivity was measured. With the initial anneal at 200 ^{o}C, the resistivity rises from it as-grown value of ~3.3x10^{-3}Ω-cm to 9x10^{-2}Ω-cm and then decreases to 2.4x10^{-2}Ω-cm after annealing to 300 ^{o}C, at which point it increases linearly with successively higher annealing, as expected[64], [65]. We have optimized the construction of the memristor with the first layer grown at 2.2 Å/cycle and annealed to 300 ^{o}C based on the results shown in Fig. 3.3. It is clear that annealing at 300 ^{o}C corresponds to a local minimum in the resistivity and that said film would be robust and stable and have the moderate resistivity needed to construct a ZnO homojunction memristor.

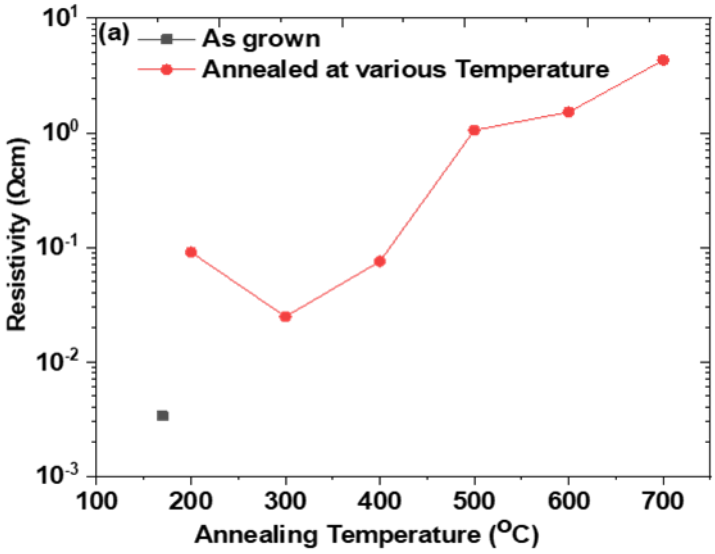

Figure 3.3. The resistivity of a 50 nm ZnO film with a growth rate of 2.2 Å/cycle (soaking) as function of annealing temperature.

The I-V curves of the double layered ZnO homojunction memristor using sinusoidal and triangular waveform voltages are displayed in Fig. 3.4(a). The I-V curves are

characteristic of a diode which is attributed to the formation of n-n junction [66], where current flow is only in the forward direction. From the XPS analysis, it is evident that the annealed base layer of ZnO contains more defects/vacancies relative to the as-grown top layer and therefore at the interface an nn-homojunction is formed. As a consequence, a depletion layer forms at the interface. The resistance for negative bias is of the order of mega ohms (Fig. 3.4(b)) but tracks with the voltage in forward bias. Note that the device can be described as having two different resistive states in a cycle, a prerequisite for a memristor. In the reverse bias, discrete multi-stability of resistive states is observed, a subject of further study. The primary effect of the choice of the waveform of the driving voltage is the shape and size of the hysteresis loop, where, as expected, the area under the curve is larger for a sinusoidal waveform.

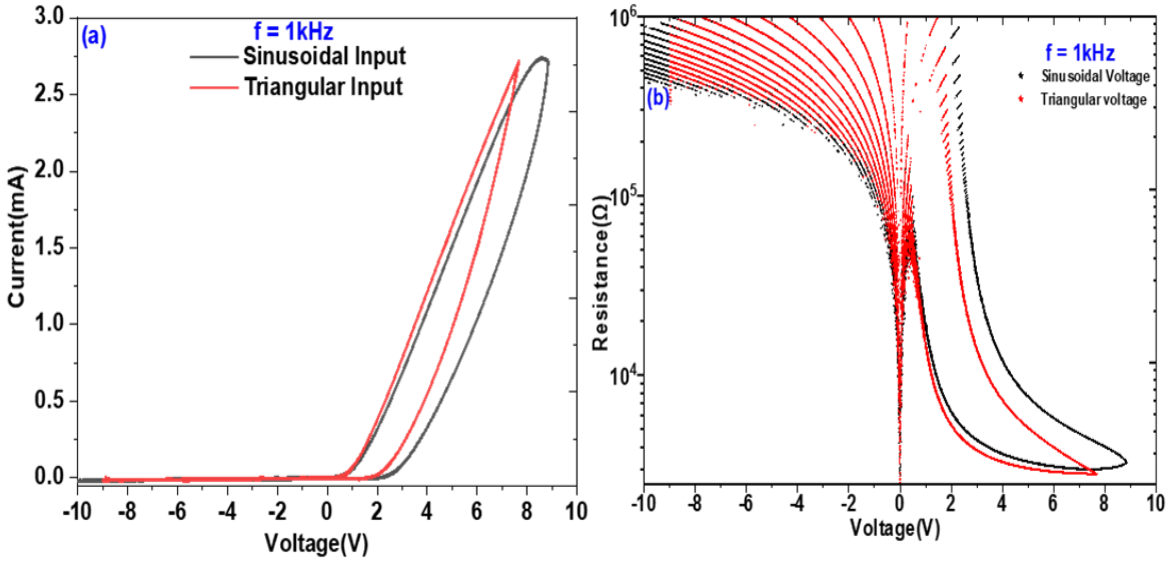

Figure 3.4: (a) I-V plot of the memristor device with a sinusoidal and triangular waveform voltage and (b) the resistance over multiple cycles at a frequency of 1 kHz. (Multiple cycle data shows temporal uniformity).

The I-V characteristics of the memristor at different frequencies (*f*), where the size of the hysteresis loop is a function of the driving frequency, are displayed in Fig. 3.5. The loop area increases steadily with increasing frequency until it reaches a maximum at 1 kHz and decreases again. This frequency dependence is a fingerprint of a memristor[67]. The hysteresis loop area corresponds to the density of charge carriers that remain in the depletion region over one cycle. At low driving frequencies (<100Hz) signal, the current is primarily a function of diffusion and subsequent recombination in the depletion layer. As the driving frequency increases above 100 Hz, space charge builds up in the depletion region due to drift velocity of the majority carriers that are not fully compensated by recombination. The space charge density reaches a maximum at a driving frequency of 1 kHz, where $1/f$ approaches the mean time between collisions (τ) associated with the carrier mobility. For f> 1 kHz, $1/f<\tau$ and the drift velocity approaches zero, at which point diffusion is once again the dominant transport mechanism. As a consequence, diffusion leads to the dissipation of carriers in the depletion region and the subsequent closure of the hysteresis loop with increasing driving frequencies. The area of the hysteresis loop as a function of driving frequency is summarized in Fig 3.5(f).

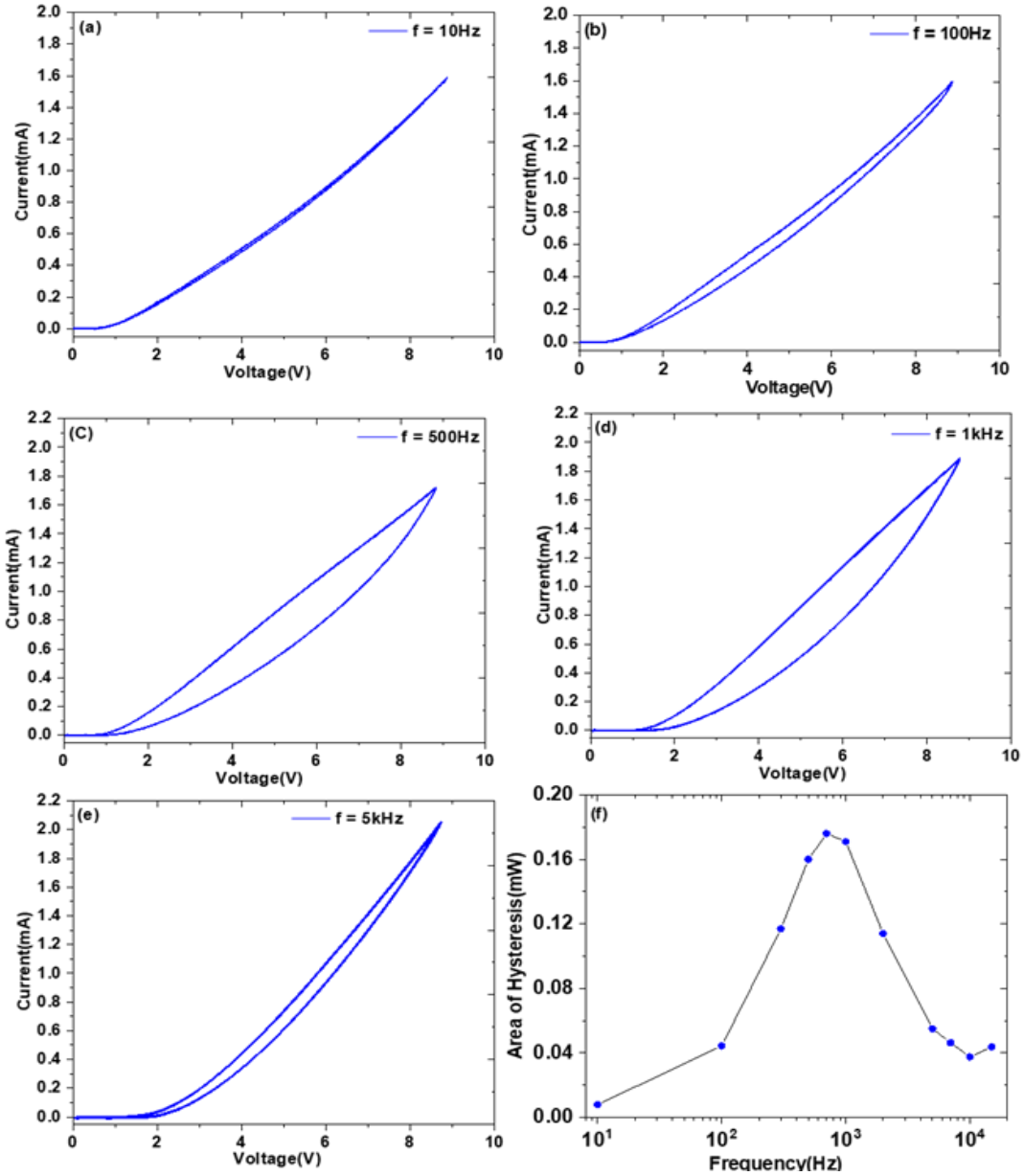

Figure 3.5: I-V curves in forward bias for one cycle of a triangular waveform voltage at frequencies of (a) 10 Hz, (b) 100 Hz, (c) 500 Hz, (d) 1 kHz, and (e) 5 kHz. (f) The frequency dependence of the hysteresis loop for forward bias as a function of frequency for a triangular waveform voltage.

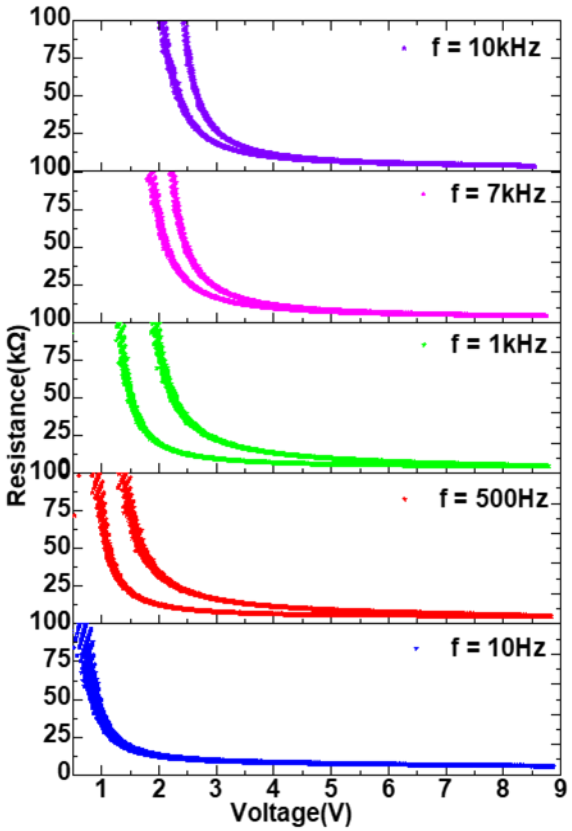

Figure 3.6: The resistance of the memristor in forward bias as a function of frequency for a triangular waveform voltage. Distinct bistability of resistance is observed, as well as a frequency dependent shift of threshold voltage.

Displayed in Fig. 3.6 is the resistance of the memristor for a triangular waveform AC voltage in forward bias as a function of frequency. The device exhibits a bistability in the resistance, i.e., a two state memristive device. The low resistive state is approximately 5 kΩ and the high resistive state is in excess of 100 kΩ. The shift of the threshold voltage as a function of frequency of the voltage source in Figure 3.6 is due to frequency dependence of the dielectric function of ZnO, which decreases with increasing frequency[68]. In turn, this results in an increase in the built-in potential of the nn-junction.

The resistive state of the device is a function of frequency for a given bias. To illustrate this, the frequency dependent low resistive state (LRS) and high resistive state (HRS) at 3 V and their ratio are plotted in Fig. 3.7(a). As expected, LRS and HRS increase with increasing frequency and plateau above 10 kHz. The ratio of HRS/LRS at a 3V bias reaches a maximum of ~2.3 at 1 kHz. In the voltage dependence of HRS, LRS and the ratio HRS/LRS at 1 kHz frequency the ratio of HRS/LRS is a maximum, in Fig. 3.7(b). The ratio HRS/LRS reaches a maximum of ~4 at 2 V and decreases with increasing voltage and below 2 V, the comparative study of HRS/LHR is irrelevant due to threshold voltage shift. Sun et al. showed that the off/on ratio is influenced by carrier concentration [69]. Because the maximum ratio of HRS/LRS of our ZnO homojunction memristor occurs at 1 kHz, the maximum size of the hysteresis loop in Fig. 3.5(f), we have concluded that the off/on ratio of our device depends on the carrier density in the depletion region. Therefore, the off/on ratio of a ZnO homojunction memristor can be tuned/designed by controlling the relative carrier densities of the ZnO layers, which is dependent upon their morphology, stoichiometry, and post preparation.

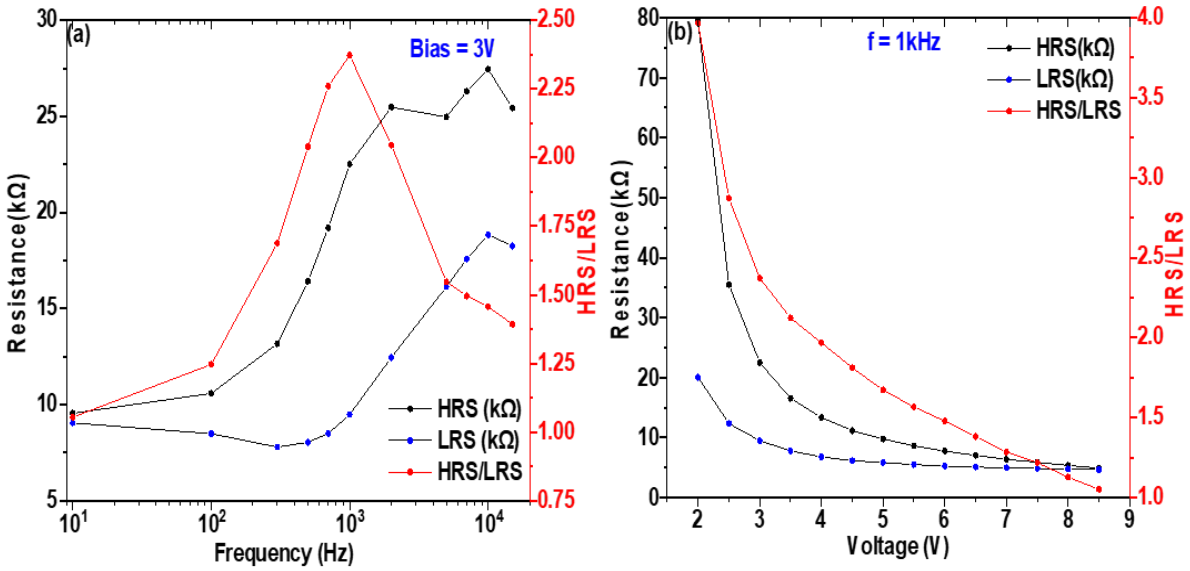

Figure 3.7: (a) The frequency dependence at 3V of the high resistive (HRS) and low resistive state (LHS) and their ratio of the ZnO homojunction memristor and (b) the voltage dependence at 1 kHz of HRS, LHS, and HRS/LRS.

3. Conclusion

A ZnO n-n homojunction memristor device has been constructed using two dissimilar ZnO thin films. The ZnO layers were grown by atomic layer deposition using two different deposition recipes in conjunction with or without annealing. The differences between the two ZnO films manifest in different carrier concentrations, where they form n-n junction relative to one another. When driven with an AC voltage, interfacial charges are swept in and out of the depletion layer formed and is manifested as hysteresis in the forward biased IV characteristics. The maximum area of the hysteresis loop occurs at a driving frequency of 1 kHz, pertaining to a maximum in the space charge within the depletion region of the junction. From the results obtained it is clear that the memristive device can exist in either a high resistive state (HRS) or a low resistive state (LRS), where the maximum of the HRS to LRS ratio occurs at 1 kHz, the frequency that corresponds to the maximum hysteresis in the I-V curve. Based on this correlation, it is

concluded that the resistive states depend on the accumulation of space charge within the depletion region, which can be controlled by tuning the materials properties of the ZnO layers. This study has demonstrated that a memristive device can be constructed by combining dissimilar ZnO thin films.

CHAPTER IV

ULTRA FAST PHOTODETECTION FROM α-Fe_2O_3 ON P-SILICON

1. Introduction

Photodetectors (PD) are devices used for detecting and measuring the characteristics of incident light. They have wide applications in various sectors of modern electronics, such as optical communications [70], [71], photodetector array cameras in space research [72], imaging the hydrogen flames and corona discharge [73], medical applications [74], wearables [75], etc. PDs can detect light by various mechanisms such as a photo-electrochemical cell [76], [77], a photodiode [78], or a phototransistor [79], [80]. Most PDs utilize external power sources to be able to detect light. PDs that do not require an external power source for light detection are a huge advantage in almost all of the applications listed herein.

α-Fe_2O_3 is an excellent absorber of visible light due to its bandgap (~2.2eV) aligning to the center of the visible spectrum [81]. Abundant availability, low cost, non-toxicity, excellent stability in aqueous environment, and environmentally friendly properties make α-Fe_2O_3 naturally preferred semiconductor in many applications, such as photo-electrochemical water splitting [82], gas sensing [83], [84, p. 3], as pigments [85] and in catalysis [86].

However, due to its poor charge carrier mobility [87] and ultrafast recombination rate of photo-generated carriers [88], its use for photodetection is limited.

To address the issue of ultrafast recombination of photo-generated carriers, herein we propose reducing the bulk of the α-Fe_2O_3 layer by reducing the thickness of the α-Fe_2O_3 thin film and create a built-in electric field with a p–n junction at the interface that spontaneously separates photo-generated carriers. Our junction uses p-type silicon substrate as the dominant transport layer due to its large hole mobility [89] and n-type α-Fe_2O_3 layer as a photo-carrier generator. A simple and cheap fabrication process, along with a non-biased operating condition, makes our device an attractive photodetector.

2. Results and Discussion

2.1. Materials' Characterizations

Multiple sets of two types of samples prepared by using different concentration of solutions of organic iron precursor were subjected to characterization. Scanning electron microscope (SEM) micrographs of the typical morphology of the two types of samples prepared using 28 mM and 141 mM solutions are displayed in Figs. 4.1 (a) and (b), respectively. The thin film sample prepared with the 28 mM solution is semi-continuous with voids with an average size of <15nm, whereas the sample prepared with 141 mM solution is highly discontinuous, consisting of bulk crystals with an average size of 175 nm. Figs. 4.2 (a) and (b) show SEM elemental mapping and energy dispersive X-ray (EDX) spectra of the sample prepared with the 28 mM solution. Similarly, Figs. 4.2(c) and (d) show SEM elemental mapping and EDX spectra of the sample prepared with the 141 mM solution. In Figs. 4.2 (a) and (c), the gold electrical contacts are represented by

green, the Si substrate by black, and Fe of α-Fe_2O_3 by red colors. As we can see from the SEM analysis of the samples prepared with the 28 mM solution, the α-Fe_2O_3 film more uniform than the sample prepared with the 141 mM solution, as well as thinner, although not apparent from the SEM micrographs, can be observed in the form of Si peak attenuation in Raman spectra later. It is shown in the later section that the thickness and distribution of α-Fe_2O_3 of the films directly affects the photo-response, as well as the zero-bias photocurrent.

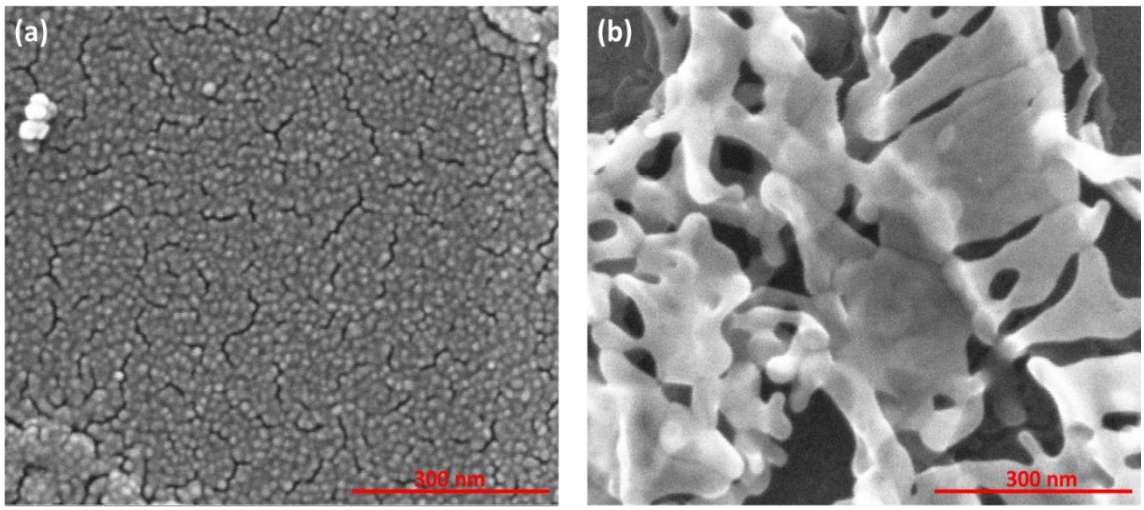

Fig. 4.1: SEM micrographs of sample prepared using (a) 28 mM and (b) 141 mM solutions.

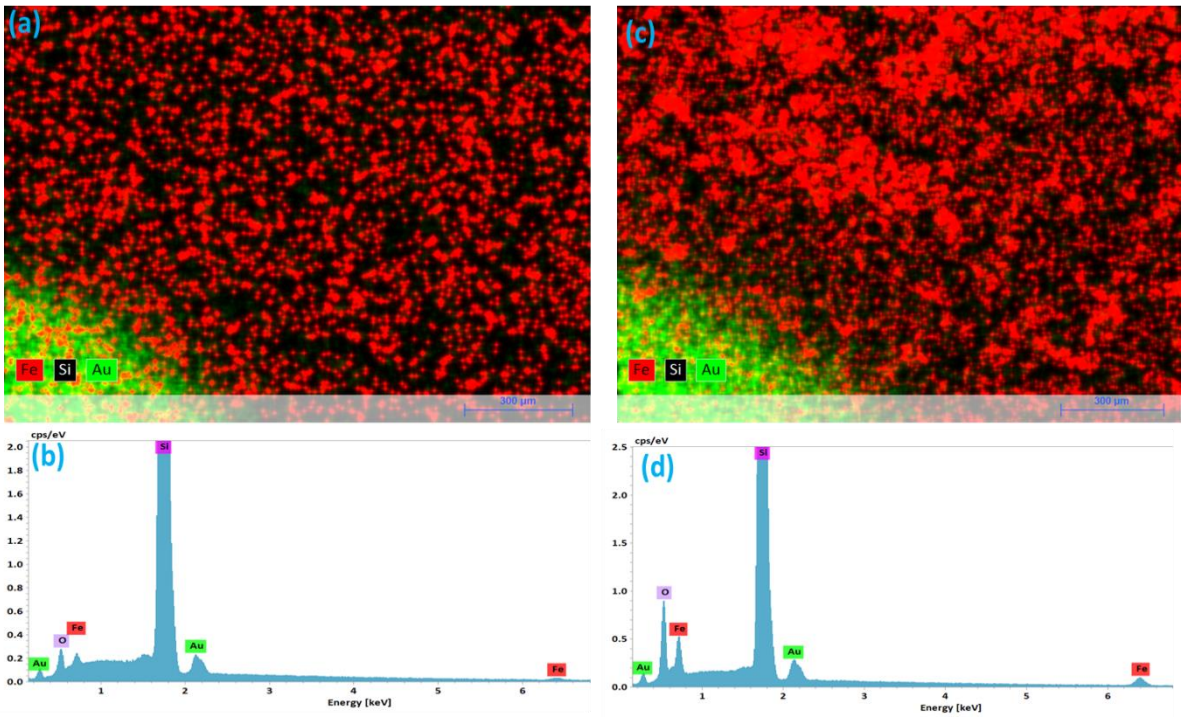

Fig. 4.2: (a) EDX mapping of elements and (b) EDX spectra for sample prepared using 28 mM. (c) EDX mapping of elements and (d) EDX spectra for samples prepared using 141 mM solutions. Higher intensity of Fe peak in (d) shows the increased size of the α-Fe_2O_3 particles in the samples.

Raman spectroscopy of the samples in Fig. 4.3 confirms the presence of Raman modes of α-Fe_2O_3. The peak at 224 cm^{-1} is assigned to the A_{1g} mode of α-Fe_2O_3. Similarly, the peaks at 293 cm^{-1}, 412 cm^{-1}, 613 cm^{-1} are assigned to the E_g modes of α-Fe_2O_3 [90], [91]. However, the peak at 659 cm^{-1} does not correspond to α-Fe_2O_3 and may possibly be due to the disorder [92]. The prominent peak at 1318 cm^{-1} corresponds to an α-Fe_2O_3 (Hematite) two magnon scattering, which is not observed for other forms of iron oxide (Magnetite, Maghemite, etc.) [93]. The peaks at 520 cm^{-1} and 975 cm^{-1} correspond to the scattering of first-order optical phonon and two transverse optical phonons in c-Si [94], where their intensities are significantly less for the sample prepared with the 141 mM

solution and attributed to attenuation associated with the greater thickness of the of α-Fe_2O_3 layer.

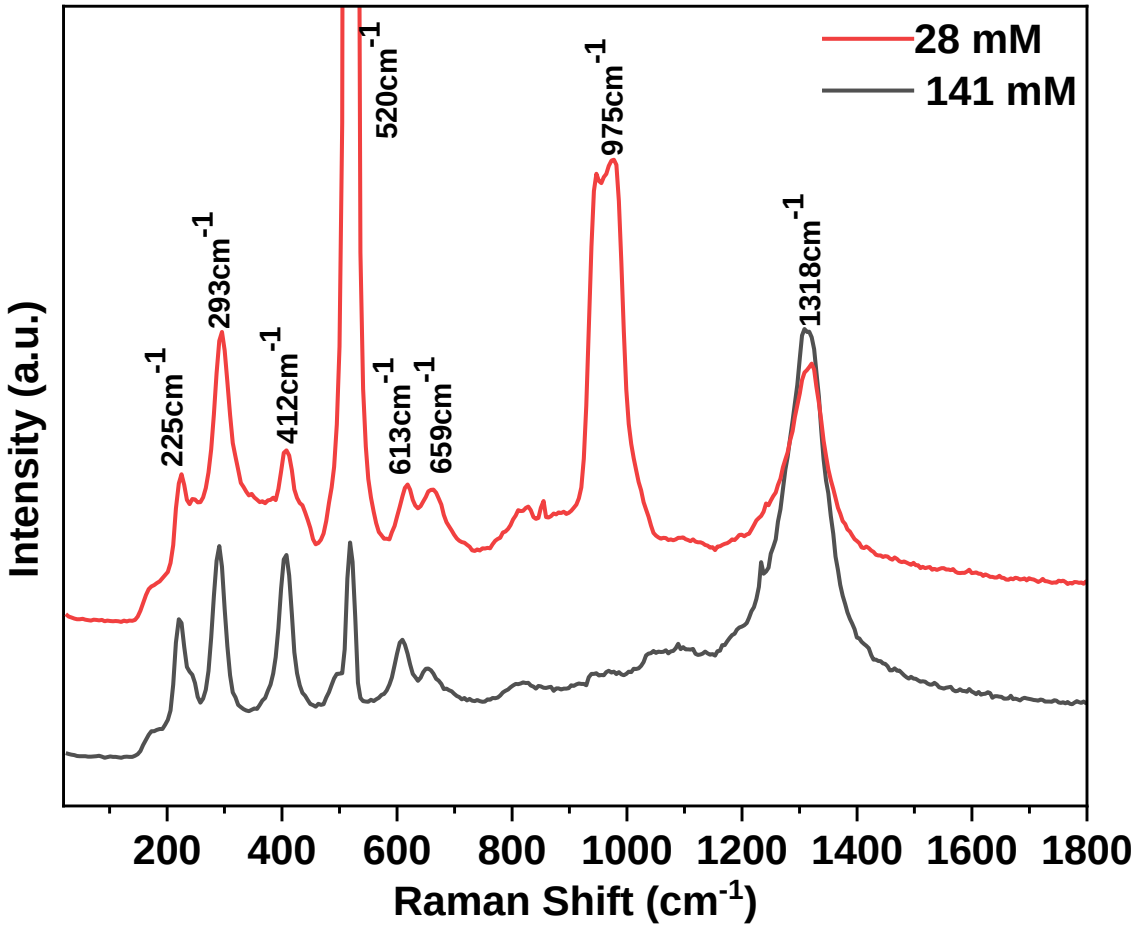

Fig. 4.3: Raman spectra of the samples prepared using the 28 mM and 141 mM solutions.

2.2. Electrical and photoresponse characteristics

The photocurrent response of the device was measured using a lock in detection, schematic of which is displayed in Fig. 2.7 of chapter II. Fig. 4.4 shows the photocurrent response of the device made from two different concentrations of the organic solutions. The devices exhibit excellent photo-responsiveness. The rise and decay periods are defined as the time it takes the signal to increase from 10% to 90% or decrease from 90%

to 10% of the peak photocurrent, respectively [95]. The rise and decay times of the two devices are 8.6 µs and 3.7 µs, respectively, which is faster than many visible light photodetectors [96]. This ultra-fast response is attributed to the fast carrier dynamics and high carrier mobility in p-Si [97], [98]. When a white LED of intensity 268 µW/cm^2 illuminates the surface of the device, the measured zero-bias photocurrent reaches 16.3 nA and 8.0 nA for the samples prepared with the 28 mM and 141 mM solutions, respectively. The decrease in peak photocurrent for the sample prepared with 141 mM is attributed to enhanced carrier recombination in the large crystals of the α-Fe_2O_3 relative to the 28 mM sample.

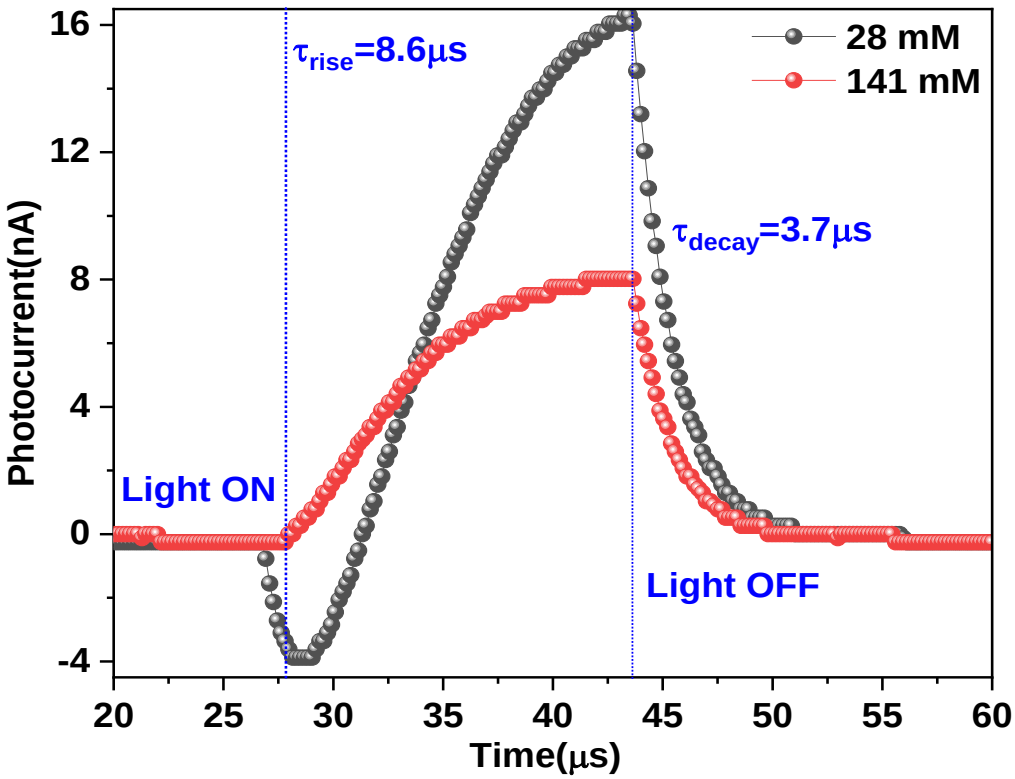

Fig. 4.4: Zero-bias photocurrent of a single pulse of illumination with white light at an intensity of 268 µW/cm^2 of the α-Fe_2O_3/Si(100) devices fabricated with 28 mM and 141 mM solutions.

Sensitivity(S) and Responsivity(R) of a photodetector are defined by the following equations (4.1) and (4.2) [99].

$$S = \frac{I_{ph}}{I_D} = \frac{I_{ill} - I_D}{I_D} \tag{4.1}$$

$$R = \frac{I_{ph}}{P \times A} = \frac{I_{ill} - I_D}{P \times A} \tag{4.2}$$

, where photocurrent $(I_{ph}) = I_{ill} - I_D$ is the difference between photocurrent (I_{ill}) and the dark current (I_D), P and A are the intensity of the light source and effective area of illumination, respectively.

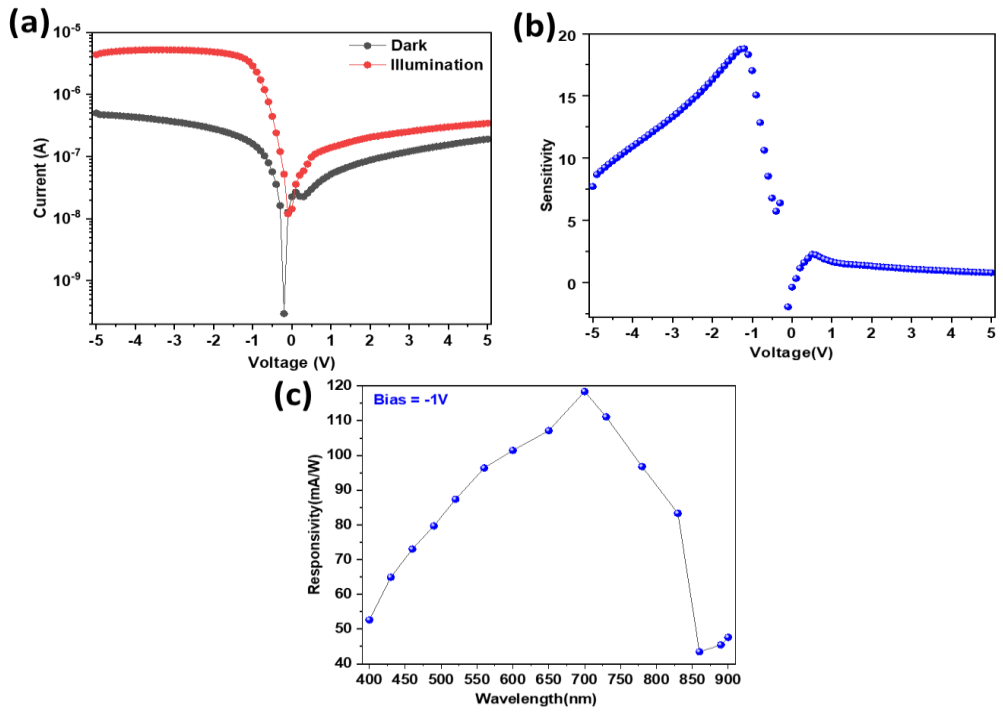

Fig. 4.5: (a) Semi-logarithmic plot of I-V characteristics of sample prepared using 28 mM solution in dark and at 268 μW/cm^2 of white light illumination. (b) Sensitivity of the photodetector as a function of applied bias. (c) The responsivity of the device as a function of wavelength of light.

Fig. 4.5 (a) is the I-V characteristics of the α-Fe_2O_3/Si(100) device fabricated with the 28 mM solution in the dark and illuminated with 268 μW/cm^2 of white light. The sensitivity calculated using equation (4.1) as a function of voltage is plotted in Fig. 4.5 (b). It is apparent that the device is highly sensitive at -1V bias. In order to measure the responsivity of the device, a monochromator sourced with white light was used to produce different wavelengths of light where the power output of the monochromator was in the order of 100 nW. Fig. 4.5 (c) shows the responsivity calculated using equation (4.2) as a function of the wavelength of light. The responsivity was measured by applying -1V bias. The device has the highest responsivity of ~ 120 mA/W at a wavelength of approximately 700 nm, which is the expected absorption peak for α-Fe_2O_3 [100].

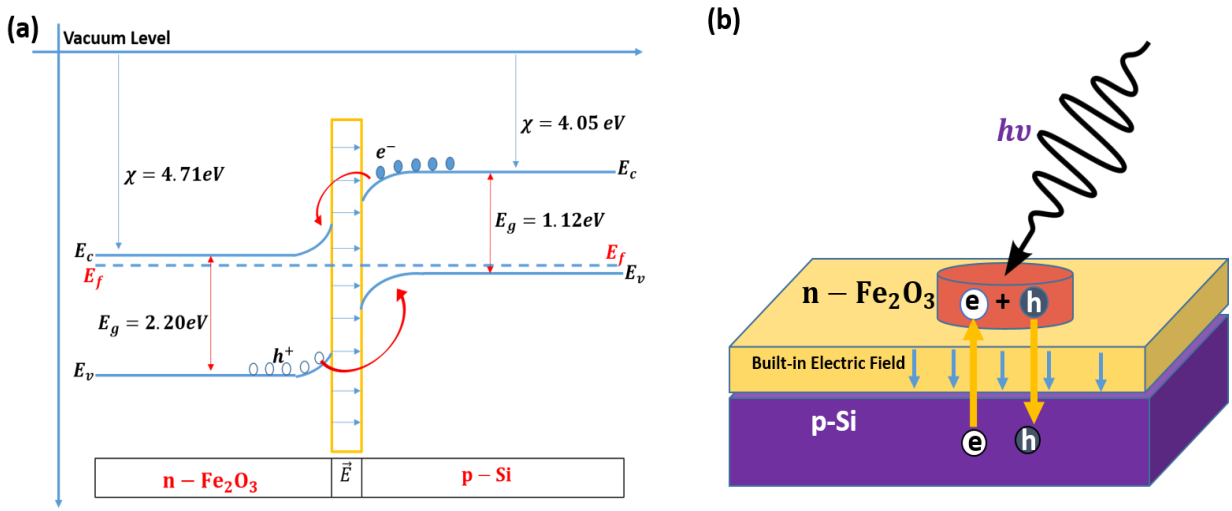

Fig. 4.6: (a) An energy band diagram of the photodetector device showing the effective separation of photogenerated carriers. (b) Schematic diagram of a single α-Fe_2O_3 microcrystalline particle on a p-Si(100) substrate and the built-in electric field formed at the interface that facilitates photogenerated carrier separation.

Fig 4.6 (a) shows the energy band diagram of the interface between α-Fe_2O_3 and p-Si(100), where α-Fe_2O_3 is an n-type semiconductor and results in band bending at the interface with the Si substrate. The conduction band level for p-Si is 4.05 eV [101] and

for α-Fe_2O_3 it is 4.71 eV [50] with respect to the vacuum level. The conduction band minimum and valence band maximum bend upwards to align with those of Si, which creates a built-in electric field that facilitates the movement of electrons towards the α-Fe_2O_3 layer and holes towards the p-Si layer. Also, the gold contact forms a small Schottky Barrier (not shown in the figure) that also inhibits the recombination of the carriers. Fig. 4.6 (b) shows a schematic diagram of a single α-Fe_2O_3 microcrystalline particle on top of p-Si and the mechanism of separation of photo-generated carriers.

3. Conclusion

A simple and easy visible light photodetector was constructed with n-type α-Fe_2O_3 thin films grown on p-Si(100) substrates. Using the fast carrier dynamics (excellent hole mobility) of p-Si and the effective built-in electric field at the interface of n-type α-Fe_2O_3 and p-Si, the photo-generated carrier separation and photoresponse speed are enhanced. We found a fast rise and fall of the photoresponse of 8.6 μs and 3.7 μs, respectively, as well as a large zero-bias photocurrent of 16.3 nA. Future works will further investigate the effect of α-Fe_2O_3 bulk size in the photoresponse.

CHAPTER V

SYNAPTIC POTENTIATION IN α-Fe_2O_3 ON P-SILICON

1. Introduction

With the proposal of the memristor as the fourth fundamental electrical element [102], [103], resistive switching materials, one possible material with which to construct memristors, have been utilized in the construction of artificial electrical synapses that emulate those of the human brain [104]–[107]. An adult human brain contains an estimated 10^{11} neurons and make nearly 10^{15} connections through synapses [108], [109], where a synapse connects two neurons, and depending on the characteristics of the electrical stimulus, the weight of the synapse (conductance) either strengthens (potentiation) or weakens (depression) the connectivity between neurons. The conductance of synaptic switches is an analog process that depends on the strength and polarity of the applied stimulus. Generally, repetitive and identical pulses of stimuli (current or voltage) are applied to the synaptic device in order to modulate its weight [110], [111]. This is similar to the theoretically predicted behavior of memristors and why they are believed to be a fundamental component of artificial synapses. Ultimately, the suitability of the memristor depends upon the properties of the materials used in their construction.

One of the primary requirements of the material used to construct a memristor for use as an artificial synapse switch is that it exhibits at least two resistance states. The mechanism whereby it changes its resistive state varies from material to material, where some examples are valence change [112], electrochemical metallization [113], ferroelectric switching [8], phase change [114], etc. The types of materials used in constructing synaptic devices ranges from 2D materials [115] to conventional metal/ metal oxide systems such as Al:HfO_2 based memristor that has been shown to have good synaptic potentiation and depression behavior [116] or TiO_2 based synaptic devices that have excellent analog memory switching with spike time dependent synaptic plasticity [117]. Other notable material systems are, GdO_x/Cu:MoO_x [118], WO_x [119], HfO_x/AlO_x [120], AlO_x [121], where all of them have been reported to have synaptic potentiation and depression characteristics. The message being that there is almost an infinite combination of materials that can be used in the construction of memristive devices suitable for use as artificial synapses.

Many synaptic devices are comprised of either low abundance materials or require complex fabrication and post processing methods. As an alternative material, Fe and Fe_2O_3 are among the most abundant and non-toxic materials on earth [122]. In addition, the band gap of Fe_2O_3 is centered in the visible range (~2.1 eV) of the light spectrum [123], ergo, suitable for visible light-based applications. Furthermore, it is a low-cost material with fast carrier transport and stability under ambient environment conditions [124]. Consequently, Fe_2O_3 has been used in various applications including photoelectrochemical water splitting [82], gas sensing [125], lithium-ion batteries [84, p. 3], etc.

Due to the aforementioned properties of Fe_2O_3, as well as the fact that oxygen vacancies in metal oxide semiconductors play a vital role in the resistive switching behavior [5], we have used it to construct a heterojunction memristor with p-type Si (100). We report on its memristive properties under dark and illuminated conditions and its suitability for use in a synaptic switch. We also examined oxygen vacancy migration under an applied bias, which is vital to resistive switching behavior of Fe_2O_3 [126]. Lastly, we demonstrate the resistive switching behavior of Fe_2O_3/Si (100) in presence of white light widens the switching window, thus producing a unipolar resistive switch that does not require a pulse of opposite polarity to reset.

2. Results and Discussion

Displayed in Fig. 5.1(a) is a single I-V cycle using a triangular waveform of 5V under dark conditions and illuminated with white light. The I-V characteristics of the device are symmetric in forward and reverse bias (only forward bias region is shown here). The device exhibits a hysteresis loop with unipolar resistive switching, where the area of the loop increases when illuminated with white light with a power density of 268 $\mu W/cm^2$. The ratio of high resistance state (HRS) to the low resistance state (LRS) at 2.5 V bias increased from 1.37 under dark conditions to 1.58 with illumination. Figures 5.1(b) and (c) are the cyclical forward bias voltage and current of the device under dark and illuminated conditions, respectively, where the current progressively increases with each cycle under dark conditions, which is indicative of charge retention [127]. Under illumination, the current initially increases with repeated cycles and then begins to decrease linearly thereafter, which suggests charge trapping that leads to recombination of electron-hole pairs [128]. Illumination also broadens the current response relative to

dark conditions, indicative of greater synaptic habituation [129]. Figure 5.1(d) is the conductance as a function of the number of cycles at a bias of 5V under dark and illuminated conditions. Under dark conditions, the conductance increases linearly until it saturates at 0.11 μS. Under illumination conductance increases and then decreases nonlinearly for approximately 25 cycles, at which point it decreases linearly. Again, an indication of charge trapping leading to electron-hole recombination.

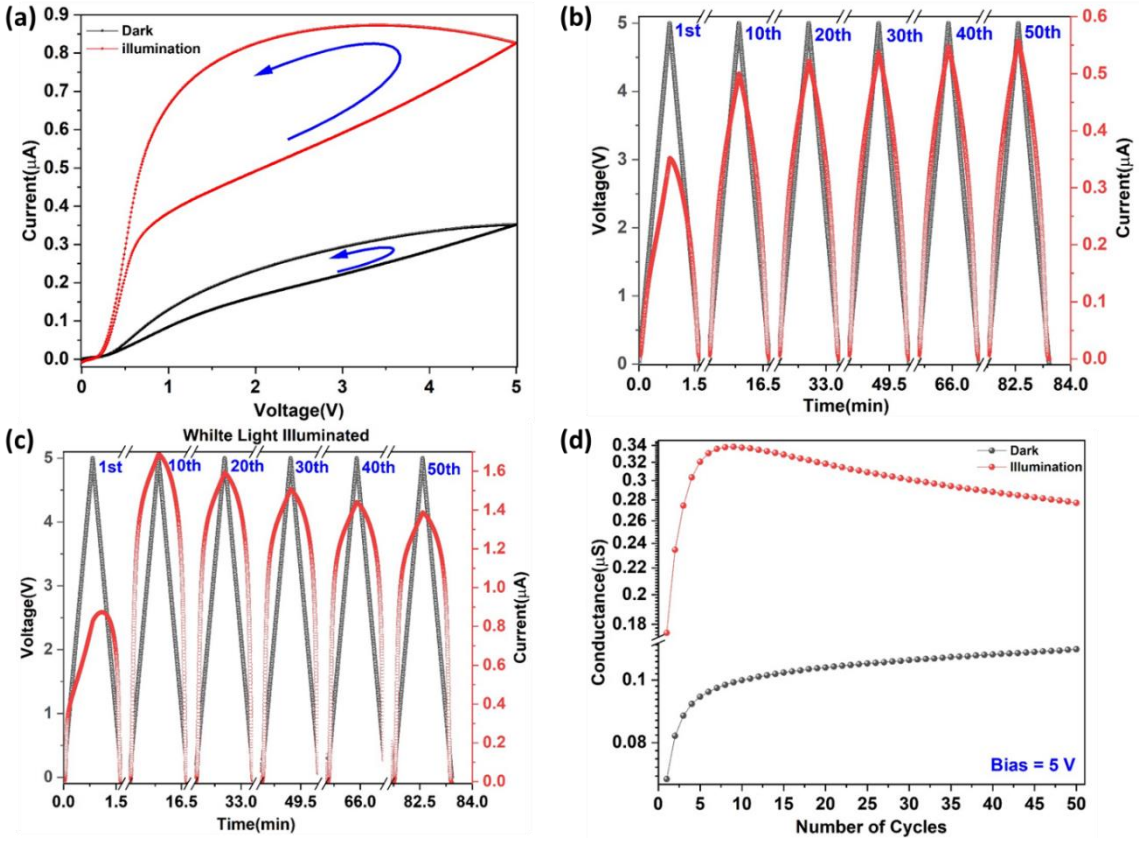

Fig.5.1: (a) I-V graph in dark and under white light illumination of a single cycle (HRS/LRS = 1.37 for dark and 1.58 for illumination at 2.5V bias). Selected cycles of 50 applied voltage and measured current cycles as a function of time in (b) dark and (c) with white light illumination. (d) Conductance as a function of number of cycles at 5 V bias in dark and white light illumination.

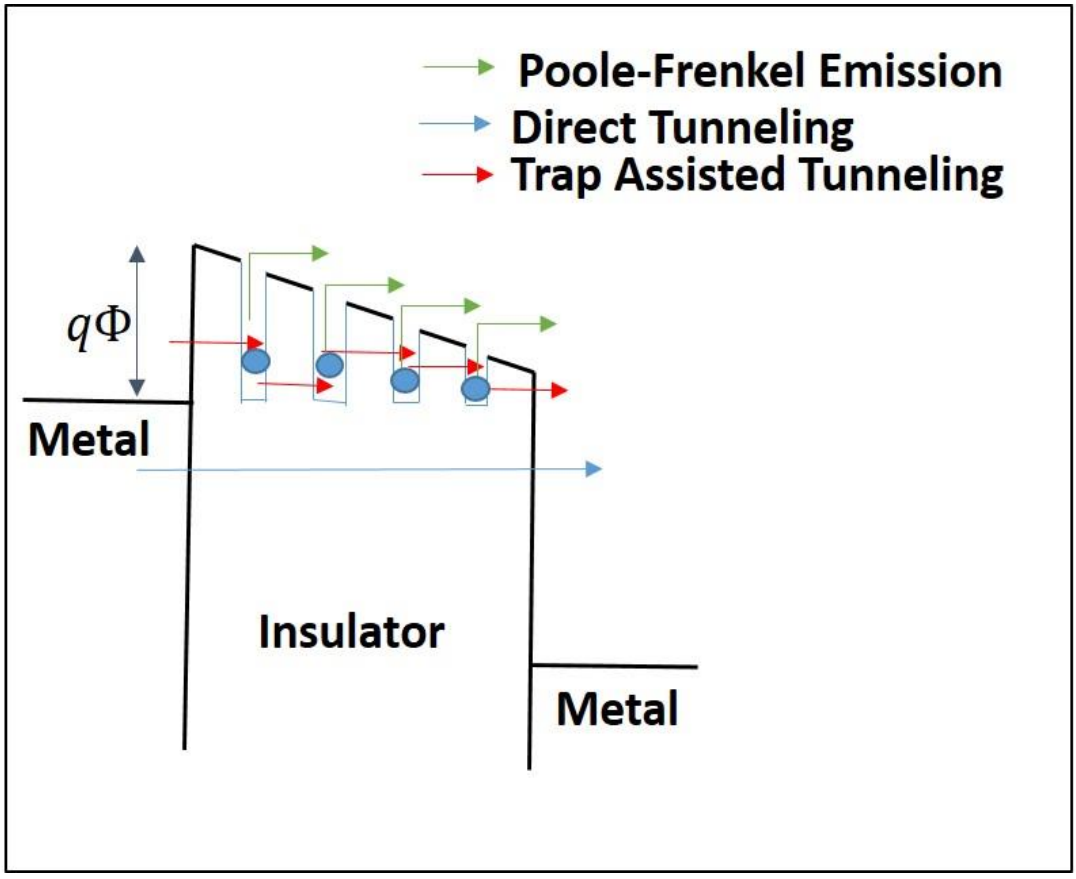

Fig.5.2: Schematic diagram showing the mechanisms of charge transport in a metal-insulator-metal (MIM) structure via Poole-Frenkel emission, trap assisted tunneling and direct tunneling.

The switching behavior in Fig. 5.1 can be understood in the context of valence change resistive switching (VCRS) devices [130]. Conduction in a metal-insulator-metal (MIM) VCRS device is a function of the bulk properties of the dielectric (bulk limited) and the electrode–dielectric interfaces (electrode limited). In the dielectric, Poole-Frenkel emission (PFE), hopping conduction, ohmic conduction, space charge limited conduction, ionic conduction and trap assisted tunneling (TAT) are conduction limiting mechanisms [131], while Schottky emission, direct tunneling (DT), Fowler-Nordheim tunneling, and thermionic-field emission are conduction limiting mechanisms of the electrode-dielectric interfaces. TAT, PFE, and DT conduction mechanisms are

schematically represented in Fig. 5.2. We will show that the predominant transport mechanisms in the α-Fe_2O_3/p-Si device are TAT and PFE.

The trap assisted tunneling mechanism, unlike DT, is a two-step process in which the carriers are initially trapped by defects or oxygen vacancies and then tunnel through the barrier to another trap and tunnel, etc., where multiple TAT events enable the carrier to cross the insulator, i.e., the carriers tunnel from one trap to another, where each tunneling event is over a fraction of the width of the metal oxide [132]. The generalized equation for TAT current density (J_{TAT}) is a function of the applied electric field(E) and given by Eq. (5.1),

$$J_{TAT} = A \exp\left[\frac{-8\pi\sqrt{2qm^*}}{3hE}\phi_T^{3/2}\right] \quad (5.1)$$

, where A is a constant and ϕ_T is the energy of the trap with respect to the conduction band edge of the metal oxide, q is the charge of an electron, m* the electron effective mass in the oxide, h is Planck's constant and E is the electric field in the metal [133]. For TAT conduction at a constant temperature, the I-V curve can be fit with Eq. (5.2),

$$y(x) = y_0 e^{\frac{-\alpha}{x}} \quad (5.2)$$

, a more generalized form of equation (5.1), where y and x are current and voltage, respectively.

For conduction by Poole-Frenkel emission, trapped carriers are excited into the conduction band of the metal oxide due to the lowering of the Coulomb barrier by the application of a sufficiently strong electric field. The current density by PFE (J_{PF}) is given by Eq (5.3),

$$J_{PF} = q\mu N_c E \exp\left[\frac{-q(\phi_T - \sqrt{qE/\pi\varepsilon})}{kT}\right] \quad (5.3)$$

, where N_c is the density of states in conduction band, E is the applied electric field, μ is electronic drift mobility, ϕ_T is the depth of the potential of the traps and T is the absolute temperature, k is Boltzmann's constant and q is the charge of an electron [131]. For PFE at a constant temperature, the I-V curve can be fit with Eq. (5.4),

$$y(x) = y_0 x e^{\alpha\sqrt{x}} \tag{5.4}$$

, a more general form of Eq. (5.3), where once again y and x are current and voltage, respectively.

Figure 5.3(a) is the I-V curve of the α-Fe_2O_3/p-Si device for a single cycle with illumination, which can be divided into two regions where either TAT or PFE dominates the conduction. The fit of Eq. (5.2) (TAT) of I-V curve in the voltage range of 0-0.7V for both ascending and descending bias is displayed in Fig. 5.3(b). The fits with Eq. (5.2) up to 0.6V are excellent for the ascending and descending bias but diverge slightly thereafter, which is attributed to the transition to or from PFE transport, respectively, i.e., 0.6-0.7V is a region of mixed TAT and PFE carrier conduction. The fit of Eq. (5.4) (PFE) of I-V curve in the voltage range of 0.7-5.0V for ascending and descending bias is displayed in Fig. 5.3(c) and is an excellent fit with the experimental data. Based on the qualities of the fits, the conclusion is that trap assisted tunneling is the primary conduction mechanism below 0.7V and Poole-Frenkel conduction above 0.7V, regardless of whether in ascent or descent. The same fits and arguments are true for the I-V curve under no illumination, which is not shown here for the sake of brevity.

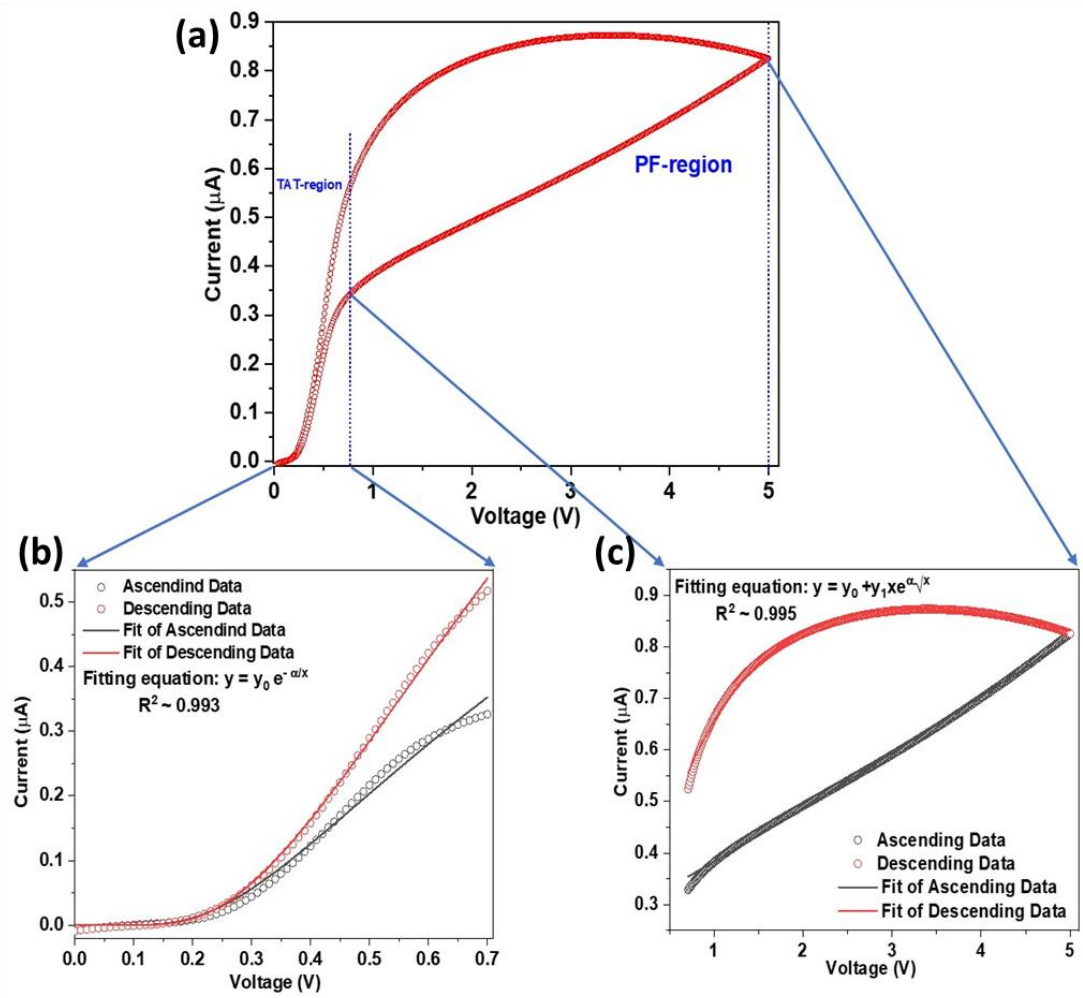

Fig.5.3: (a) One I-V cycle of the α-Fe_2O_3/p-Si device with white light illumination. (b) The fitting of the curve in (a) in the range of 0-0.7V with trap assisted tunneling conduction and (c) in the range of 0.7- 5V with Poole-Frenkel emission conduction. The goodness of the fits (R^2) is 99%.

Now that the transport properties of a single cycle of the α-Fe_2O_3/p-Si device is satisfactorily explained, we turn our attention to the cycle dependence of the device. The hysteresis of the I-V curves of the device under dark conditions or illuminated suggests that the device has memristive characteristics [134], [135] and, therefore, useful in the construction of artificial synaptic circuits [136]–[139]. As a consequence, we use the Hill equation (Eq. (5.5)) [140],

$$y = y_{max} \frac{x^n}{K^n + x^n} \tag{5.5}$$

, which is a three-parameter nonlinear equation, where K indicates the threshold of the independent variable(x) at which the dependent variable(y) reaches half of its maximum(y_{max}) and n is called the Hill coefficient or cooperativity that indicates the steepness of the curve. This equation is commonly used to describe the drug dose, drug concentration and effect over time in pharmacology [141] [142], [143]. It is also used in modeling the binding of ligands to a protein molecule, where the Hill coefficient(n) becomes significant. If $n > 1$, binding of one ligand increases the affinity of binding for further ligands and it is called positive cooperation or cooperative binding, and if $n < 1$, binding of one ligand decreases the affinity of binding for further ligands, which is called negative cooperation or non-cooperative binding [144]. In the present case, we hypothesize that each pulse excites trapped carriers to the conduction band of the Fe_2O_3, which inhibits further excitation of the carriers due to the fermionic nature of the carriers and provided they are not excitons [145]. The inhibition of further excitation is modelled

as a negative cooperative excitation and fitted to the data by fixing the Hill coefficient to n=0.4 (negative cooperation) for the best fits.

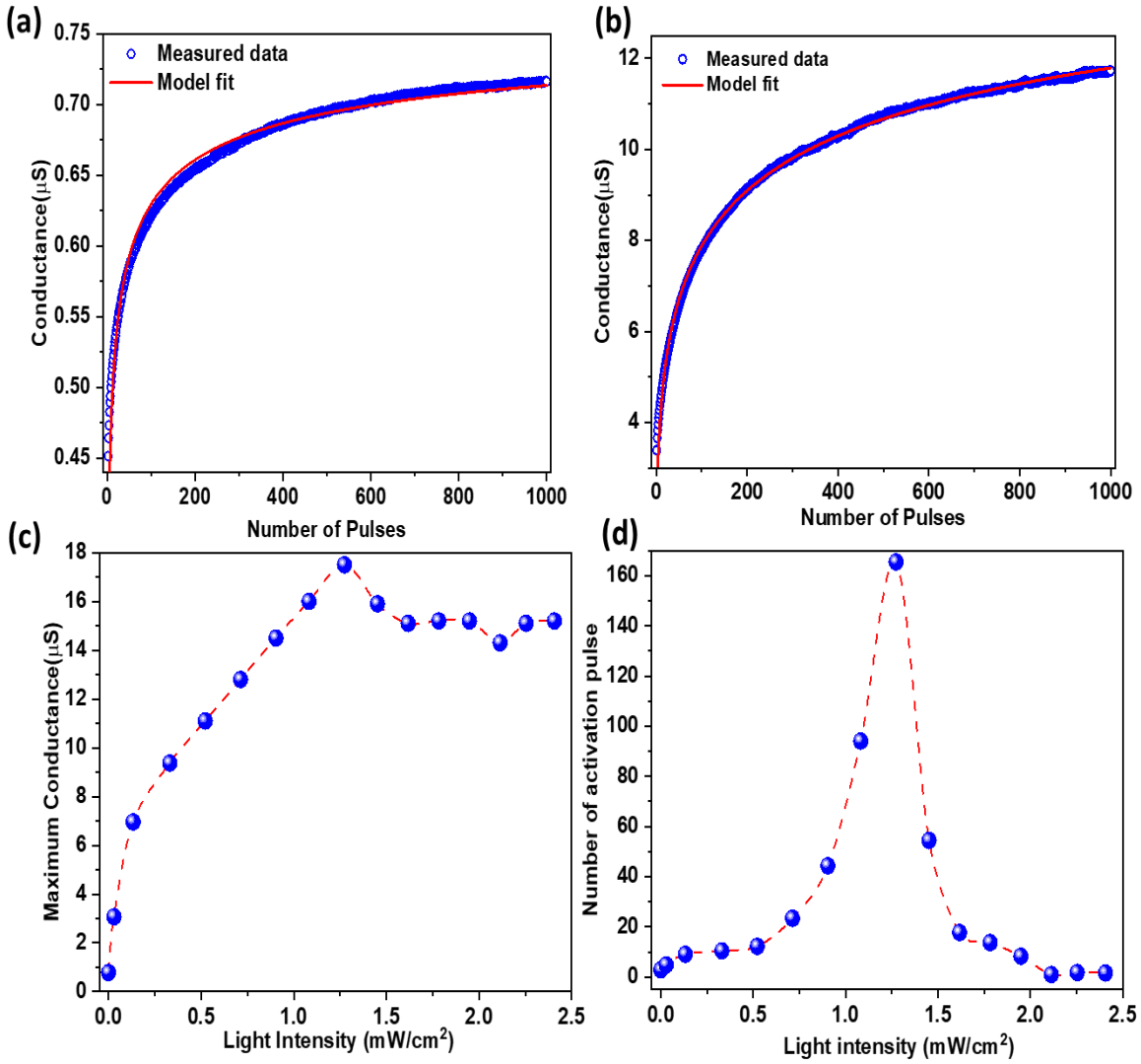

Fig.5.4: The conductance as a function of number of pulses for $\alpha - Fe_2O_3$/p-Si device when measured (a) under dark conditions, (b) white light illumination with an intensity of 1.27 mW/cm^2, (c) maximum conductance based on the fit with the Hill equation as a function of light intensity, and (d) the number of activation pulses for the conductance to plateau as a function of light intensity, also based on the fit with the Hill equation fit. The Hill coefficient was held at 0.4 for the fits used to obtain the data in (c) and (d). The triangular electrical pulses with an amplitude of 5V, a width of 10 ms, and a period of 100 ms were used for all the measurements.

Table 5.1: The fitting parameters of the Hill equation used to fit the conductance as a function of the number of pulses under dark conditions and with white light illumination of 1.27 mW/cm^2, as well as the corresponding statistics of the fits.

Parameters	Dark	Illumination
Reduced χ^2	5.73×10^{-17}	8.25×10^{-15}
Adjusted R^2	0.97	0.99
y_{max}(S)	$7.82 \times 10^{-7} \pm 8.01 \times 10^{-10}$	$1.75 \times 10^{-5} \pm 2.90 \times 10^{-8}$
K	2.88 ± 0.05	165.56 ± 1.70
n	0.40 ± 0.00	0.40 ± 0.00

The cooperativity constant (n) was held at 0.4 for the analysis. The fit of the Hill equation of the conductance as a function of number of pulses for the dark and illuminated conditions is plotted in Figs. 5.4(a) and (b), respectively, with statistics and extracted parameters listed in Table 5.1. The threshold (K) is found to be ~3 pulses in dark and ~166 pulses when illuminated with white light with an intensity 1.27 mW/cm^2. The threshold can be thought of as the synaptic activation of the device, i.e., the device activates after 3 and 166 pulses of voltage under dark and illuminated conditions, respectively. The maximum conductance, where the conductance begins to plateau, is determined by fitting with the Hill equation. Fig. 4(c) is the maximum of the conductance extracted from the Hill equation fit as a function of incident light intensity, which demonstrates that the maximum conductance increases with increasing intensity of light, reaching a maximum at approximately 1.3 mW/cm^2, followed by a decrease to a constant value of approximately 15 μS. Charge trapping and de-trapping is believed to be the mechanism responsible for conductance switching, where light enhances the phenomena [146]. The presence of different types of trap states (deep and shallow) can have

competitive effects on the rate of the number of carries trapping/de-trapping and, hence, conductance saturation since shallow and deep traps are faster and slower to trap and de-trap the carries, respectively [147], [148]. Light intensity not only dictates the number of photo-generated carries but also helps in de-trapping the carries along with phonon and tunneling assisted de-trapping mechanisms [149]. A 5V pulse, which is in PFE region, excites the carriers from the trap to the conduction band of the oxide, thereby increasing the conductance with each pulse, but is limited by the finite density of trap states and trapped carriers. The hypothesis is that the maximum conductance increases with increasing intensity of light as long as the available and accessible trap states are available to be filled, where after that the conductance is no longer intensity dependent and increasing the intensity further only increases the probability of carrier recombination, thereby decreasing the conductance from the maximum and eventually plateaus. The rational for using the Hill equation to derive the data in Fig. 5.4(c) is that it better incorporates the competing mechanisms that affect trapping/de-trapping and excitation/recombination of carriers. The number of voltage pulses as a function of illumination intensity is plotted in Fig. 5.4(d), which shows that the activation of the device is programmable and controlled by the intensity of illumination. As the intensity of light incident on the device increases, the number of pulses of synaptic activation increases, reaches a maximum at 1.3 mW/m^2, the corresponding maximum of the maximum conductance in Fig. 5.4(c), and subsequently declines with increasing light intensity. The rise and fall of the number of pulses as a function of light intensity is nonlinear, which is expected because the conductance window is widest at the maximum of the maximum conductance.

The programmability of the synaptic activation of this device using light intensity, along with the synaptic potentiation with number of electrical pulses through the device, suggests that this device can be used in artificial synaptic electronics. Although, various attributes (pulse period, width, and amplitude dependence) of the synaptic potentiation shown by the device have yet to be investigated, this work serves as a starting point using the synaptic behavior of α-Fe_2O_3/p-Si device in future synaptic electronics.

3. Conclusion

We successfully fabricated a device with promising synaptic electrical character using α-Fe_2O_3 microcrystalline films on p-type Si(100). Using trap assisted tunneling and Poole-Frenkel emission models fit to the experimental data, we have demonstrated that the device has two different conduction mechanisms when operated in low (0 V - 0.7 V) and high (0.7 V – 5 V) voltage ranges. Specifically, between 0 – 0.7 V range, the dominant conduction mechanism is trap assisted tunneling, and as the voltage surpasses 0.7 V, carriers trapped in defect sites are excited into the conduction band of α-Fe_2O_3, at which point Poole-Frenkel emission conduction mechanism dominates the carrier transport. Based on an analogy to protein-ligand binding, the Hill function has been used to demonstrate the voltage pulse induced activation of the device under dark conditions is three, while with illumination with a white light of intensity 1.27 mW/cm^2 it is 166 pulses. The synaptic potentiation of the device is very interesting and worthy of further investigation. Future studies will examine the temporal variations of the activation with ultra-fast electrical pulses.

CHAPTER VI

RESISTIVE SWITCHING AND NEGATIVE DIFFERENTIAL RESISTANCE IN α-Fe_2O_3 NANO POROUS THIN FILMS

1. Introduction

A nonlinear transport effect, where the current decreases with increasing voltage in a current voltage curve, is called negative differential resistance (NDR) phenomena [150]. Although, there is a debate on a statement "when a current voltage characteristic is measured and the curve is a pinched hysteresis loop then it is a memristor" [2], [151], a hysteresis in the I-V curve does indicate resistive switching (RS) behavior. NDR phenomena has attracted attention due to its applicability in memory applications [152], resonant tunneling and fast switching [153], [154] frequency multiplier [155], high frequency oscillator [156] and other types of electrical circuits [157].

Transition metal oxides (TMOs) have shown many interesting electrical properties, including resistive switching with a homojuction diode in double layered ZnO [158], coexistence of unipolar and bipolar resistive switching in ZnO thin films [159], memory and threshold in NiO_2 [160] etc. One of the interesting properties shown by TMOs is coexistence of RS and NDR. Many material systems, for example, Cu_2S [161], ZnO [162], Fe_2O_3 [163], TiO_2 [164], h-$LuFeO_3$/$CoFe_2O_4$ [165], $Cu_2ZnSnSe_4$ [166] and several other metal oxides [167], [168] have shown RS with NDR phenomena.

Most of the RS behavior and NDR phenomena reported in the literature have shown poor reproducibility because of their accidental occurrence or poor stability at room temperature.

RS and NDR phenomena arise due to charge storage [164], polarization relaxation [169], SCLC [170], [171], magnetoresistive dielectric breakdown [172] and combination of thermal, chemical, or electronic effects [112]. Moisture also plays an important role while taking electrical measurement in ambient environments. Carbon nanotube field effect transistors have shown a hysteresis due to charge trapping by water molecules [173]. Similarly, ionization and deionization of water was found to be responsible for the current collapse at the device surface of AlGaN/GaN transistors [174]. The effects could be non-intrinsic rather than a combined effect of environmental and material.

In this chapter, we have shown a highly reproducible co-occurrence of symmetrical RS and NDR phenomena in a nanoporous and discontinuous α-Fe_2O_3 thin films in a humid environment. Since the electrical measurements were performed in a controlled environment, we propose the decomposition of water molecules and formation of space charge region at the electrodes, which increases the barrier heights, thereby giving rise to the NDR effect. In a single I-V cycle, the adsorption and desorption of water molecules causes the symmetric I-V with RS and NDR.

2. Results and discussion

The SEM micrograph in Fig. 6.1(a) reveals a discontinuous and porous iron oxide film on a glass substrate. See Ch. 2 for details on the growth of the iron oxide film. The voids are as large as 200 nm. The highly resistive nature of the film in vacuum arises from the

discontinuous morphology of the film. Raman spectra peaks in Fig. 6.1(b) shows the presence of E_g phonon modes of α-Fe_2O_3 at 220 cm^{-1}, 408 cm^{-1}, 613 cm^{-1} [91], [175] and A_{1g} phonon mode at 498 cm^{-1} [90]. The peaks at 659 cm^{-1} and 817 cm^{-1} may be due to the disorder and a single magnon process [92]. The prominent peak at 1318 cm^{-1} is indicative of two magnon scattering process, which is a typical characteristic of α-Fe_2O_3 that distinguishes from other phases of iron oxides (β-Fe_2O_3, γ-Fe_2O_3, etc.) [93]. Fig. 6.2(a) shows the EDX elemental map of the sample on the glass substrate. The map shows sparse distribution of Fe. Similarly, The EDX Spectra in Fig. 6.2(b) shows the relative amount of Fe along with other elements present on the glass substrate. We hypothesize that the voids are sites for the water adsorption that bridge the gap between regions of the film and make the film less resistive in the presence of humid air.

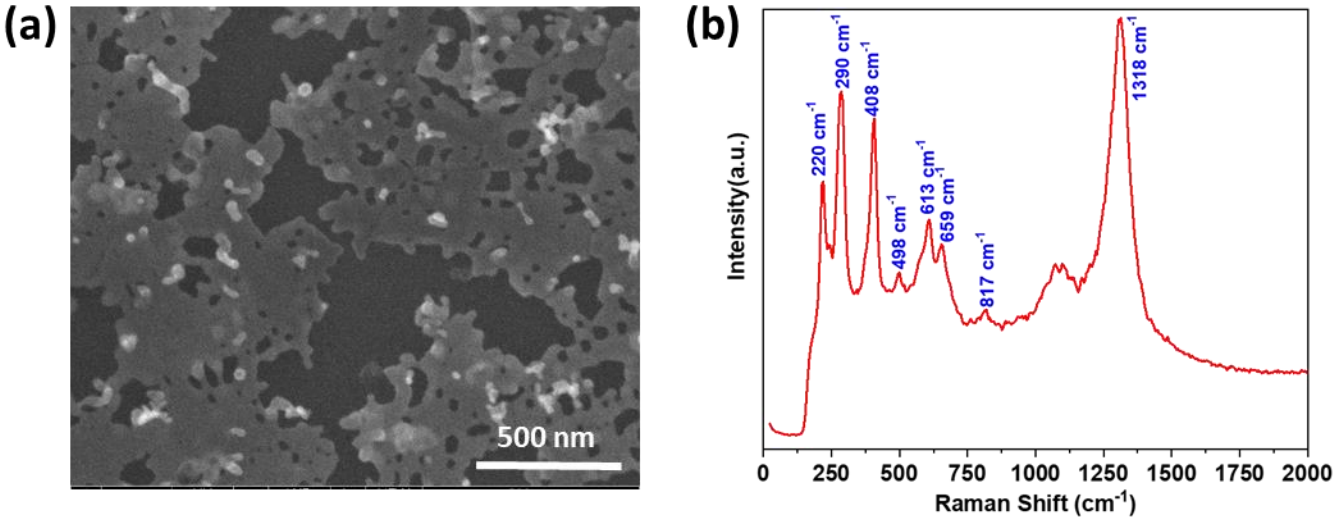

Fig. 6.1: (a) SEM micrograph of an α-Fe_2O_3 sample showing the porous and discontinuous thin film. (b) Raman spectra of α-Fe_2O_3 porous thin film on glass substrate showing the signature modes of α-Fe_2O_3.

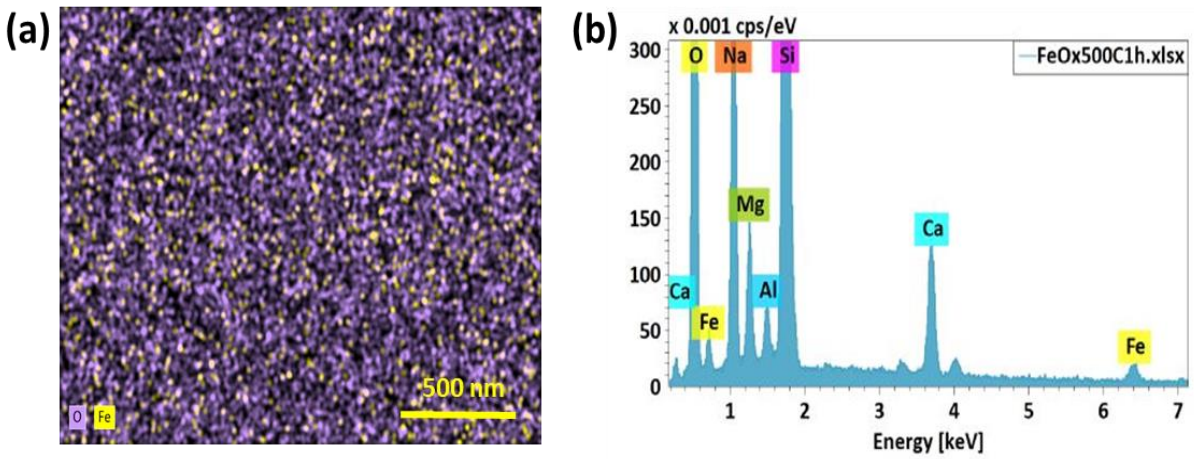

Fig. 6.2: (a) EDX micrograph of an α-Fe_2O_3 sample showing the distribution of α-Fe_2O_3 in porous thin film. (b) The spectra of the sample shows the presence of Fe and O along with elements in the glass substrate.

The I-V characteristics of the samples taken by sweeping the voltage from 0 V to 10 V, 10 V to -10 V and -10 V to 0 V cycle, at the rate of 0.2 V/s for 100 cycles in a humid environment of relative humidity (RH) of 98% are displayed in Fig. 6.3(a). The current first increases with increasing voltage up to a peak current at 4.5 V and then starts to decrease sharply, which is the signature of NDR. The I-Vs are symmetric and highly repeatable. The small discrepancy with successive I-V cycles is attributed to the current resolution of Keithley SMU, small fluctuations in the humidity level and possibly condensation of water droplets on the sample. From the I-V graphs, the values of the high resistant state (HRS) and low resistance state (LRS) at 2 V bias were extracted and plotted in Fig. 6.3(b). The HRS consistently decreases with increasing number of I-V cycles, which could be due to the hydroxylation of α-Fe_2O_3 [176] inside the film, thereby decreasing its resistance at each cycle. The sample shows an average ratio HRS/LRS of ~12 over the 100 cycles of a triangular voltage sweep at RH 98%.

Fig. 6.4 shows the conductance change as a function of applied voltage pulse in an environment of 90% relative humidity. The 5 V pulse of width 200ms applied at 1s interval shows an exponential decrease in conductance of the sample from ~1.39 nS to ~0.22 nS. When the polarity is flipped from positive to negative after 500 pulses, the conductance goes back to its original state at ~1.39 nS, and the trend repeated. The identical trend of decrease in conductance for both polarities' pulses and the symmetrical I-V curves suggests that a resistive switching mechanism of charge trapping and de-trapping at the interface is at play [164].

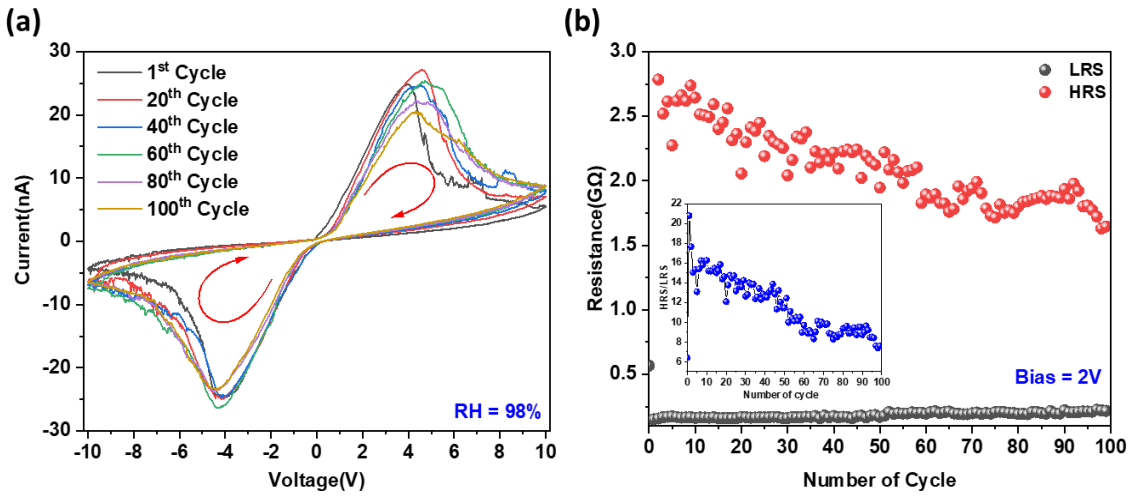

Fig. 6.3: (a) Selected cycles from 100 triangular I-V cycles in α-Fe_2O_3 porous thin film in an environment of relative humidity 98%. (b) High and low resistance states in α-Fe_2O_3 porous thin film at 2 V bias in the humid environment for 100 cycles of triangular I-V. Inset shows the ratio HRS/LRS for all 100 cycles.

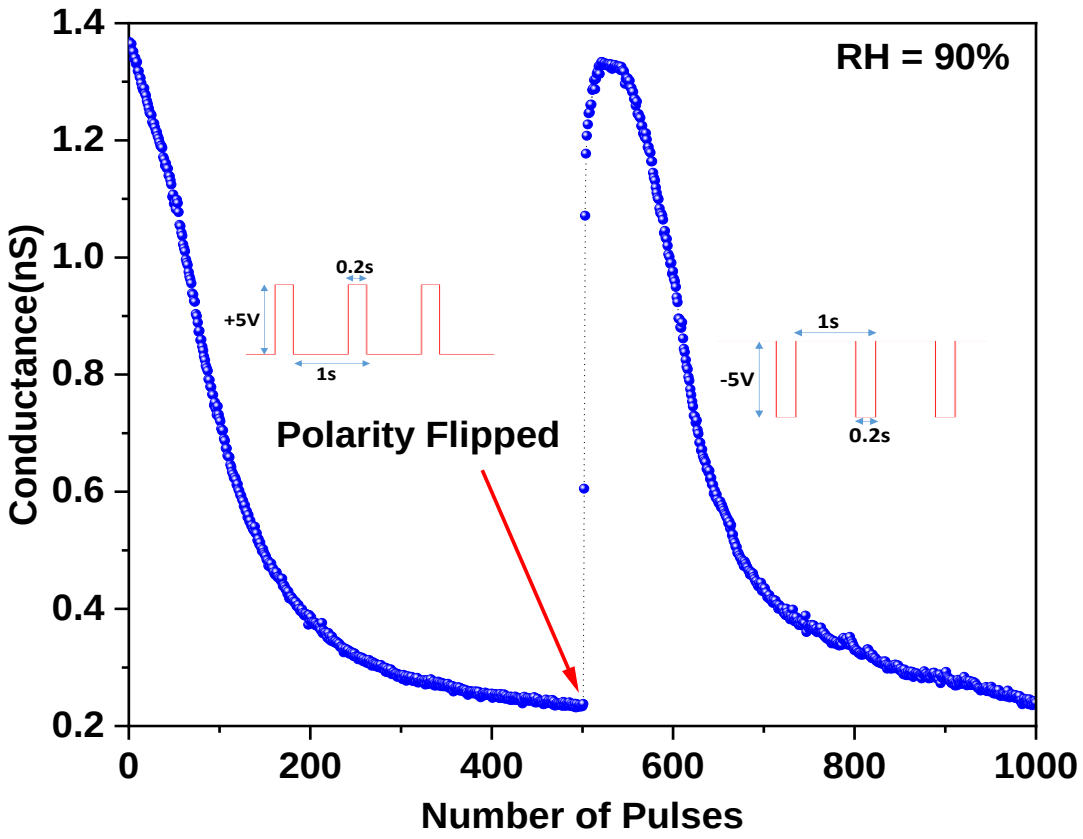

Fig. 6.4: Conductance as a function of number of pulses applied through the α-Fe_2O_3 porous thin film for 1000 pulses at relative humidity of 90%. The polarity of the pulse is flipped at 500 pulses.

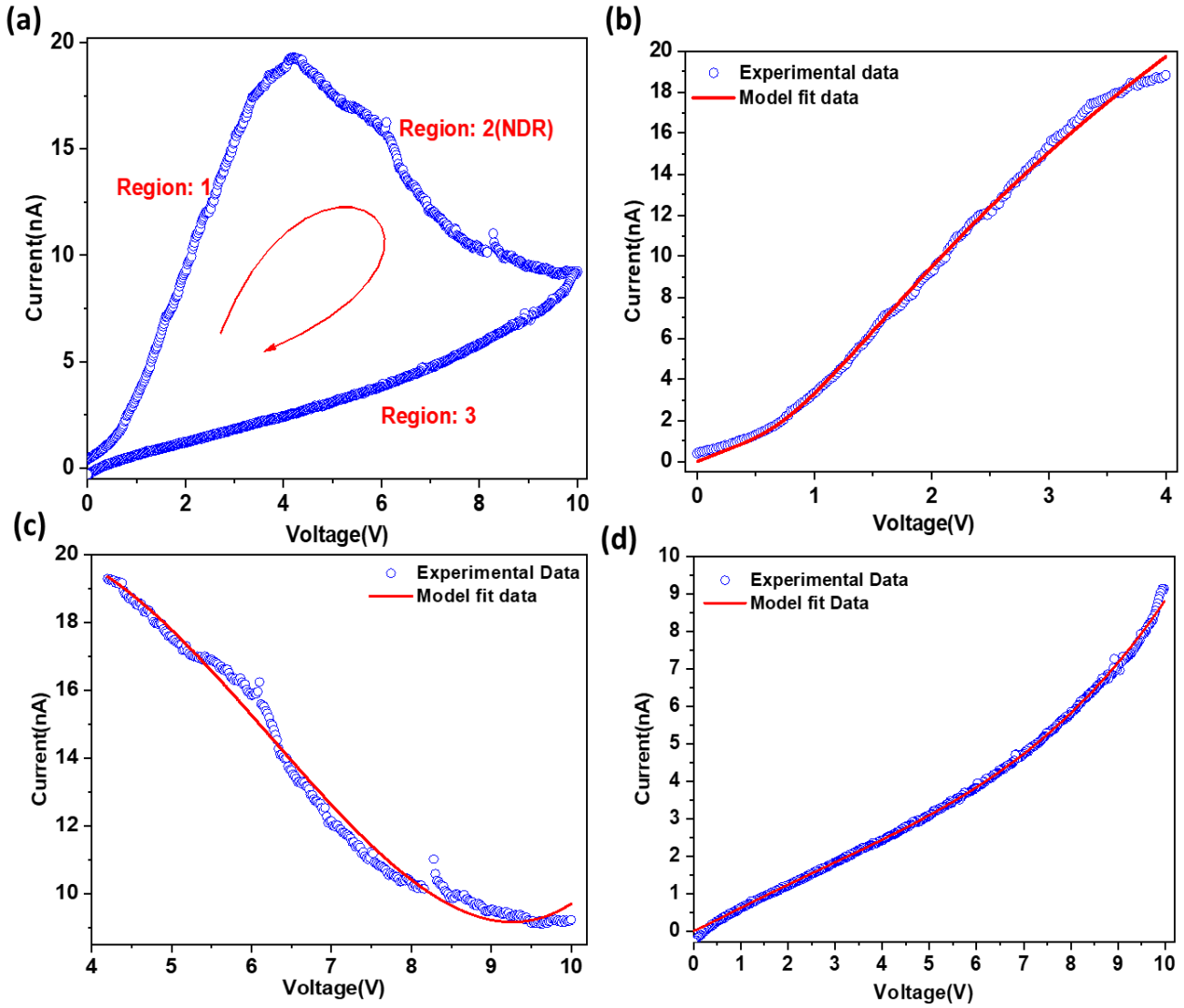

Fig. 6.5: (a) One I-V in forward bias of α-Fe_2O_3 porous thin film in the humid environment. These regions are fitted with different conduction mechanisms. (b) Region 1 is fitted with ohmic and trap assisted tunneling, a positive contribution of current comes from both mechanisms. (c) Region 2 is fitted with a positive contribution of Poole-Frenkel emission (PFE) and a negative contribution of space charge limited current (SCLC). (d) Region 3 also fits well with a positive contribution from PFE and a negative contribution from SCLC. Corresponding equations for fitting the data, values of the fitting parameters and the statistics of the fits are summarized in Table 6.1.

To understand the mechanism of charge transport in the porous film in the presence of water molecules, attempts have been made to model the forward bias portion of a I-V curve since the I-V curve is symmetric and the transport phenomena is equivalent to that

of the forward bias region of the I-V curve. A well-known ohmic equation (V = IR or y = y_0x) is used to fit the region of the I-V where ohmic conduction is expected. The trap assisted tunneling (TAT) and Poole-Frenkel emission (PFE), with their general equations, are described in chapter V. For space charge limited conduction (SCLC), if electron injecting from the contact to the Fe_2O_3 insulator, electrons travel from the metal to the conduction band of the insulator and form a space charge region analogous to a thermionic cathode in vacuum [177]. For a single discrete trapping level, the current density for SCLC is given by the following equation [178],[179],

$$J_{SCLC} = \frac{9}{8}\varepsilon_i \mu \theta \frac{V^2}{d^3} \tag{6.1}$$

, where ε_i is the permittivity of the oxide, μ is the mobility, θ is the ratio of free and shallow trapped charge, d is the thickness of the oxide and V being the applied voltage. During the fitting, a more general equation of the form, $y = y_2x^2$ is used.

Fig. 6.5(a) shows the division of a single cycle of I-V in a forward bias into three different regions where multiple conduction phenomena are present. Fitting is performed by combining the two different transport mechanisms in a single function. Fig. 6.5(b) shows the fit of the data for region 1 with an equation formed by combining ohmic and TAT mechanisms. The fits of regions 2 and 3 are fit with a combination of PFE and SCLC are shown in Fig. 6.5(c) and 6.5(d), respectively. When voltage across the sample is gradually increased, the current is due to the positive contributions of ohmic and TAT conduction. As for the role of humidity, the expectation is that water molecules are adsorbed at oxygen vacancies [180]. The adsorbed water molecules subsequently decompose once the voltage reaches its threshold or breakdown voltage of water [181], at

which point the ions (H_3O^+ and OH^-) begin to migrate towards the electrode (metal contact) and forms a space charge region that increases the barrier height to conduction. This hinders the diffusion of electrons and decreases the current showing NDR phenomena in region 2. Coefficients y_1 and y_2 in Table 6.1 for regions 2 and 3 indicate the strengths of PFE and SCLC contribution in the conduction mechanisms, respectively. The large negative coefficient (y_2) in Table 1 for region 2 indicates the formation of a space charge region that hinders the diffusion of electrons, which greatly reduces the current in region 3 when the voltage is swept from 10 V to 0 V.

Table 6.1: The fitting equations, fitted parameters and statistics of all three regions shown in the I-V curve in Fig. 6.5.

Regions	**1**	**2**	**3**
Fitting equation	$\mathbf{y = y_0 x + y_1 e^{\frac{-c}{x}}}$	$\mathbf{y = y_0 + y_1 x e^{c\sqrt{x}} + y_2 x^2}$	$\mathbf{y = y_1 x e^{c\sqrt{x}} + y_2 x^2}$
Reduced χ^2	$\mathbf{7.02 \times 10^{-20}}$	$\mathbf{1.26 \times 10^{-19}}$	$\mathbf{5.31 \times 10^{-21}}$
Adjusted R^2	**0.99**	**0.98**	**0.99**
$\mathbf{y_0}$	$\mathbf{2.22 \times 10^{-9}}$ $\mathbf{\pm 8.06 \times 10^{-11}}$	$\mathbf{1.26 \times 10^{-8}}$ $\mathbf{\pm 1.55 \times 10^{-9}}$	**NA**
$\mathbf{y_1}$	$\mathbf{2.33 \times 10^{-8}}$ $\mathbf{\pm 5.43 \times 10^{-10}}$	$\mathbf{3.88 \times 10^{-9}}$ $\mathbf{\pm 4.42 \times 10^{-10}}$	$\mathbf{4.63 \times 10^{-10}}$ $\mathbf{\pm 3.38 \times 10^{-12}}$
c	$\mathbf{3.07 \pm 0.04}$	$\mathbf{0.67 \pm 0.01}$	$\mathbf{0.64 \pm 0.01}$
$\mathbf{y_2}$	**NA**	$\mathbf{-3.29 \times 10^{-8}}$ $\mathbf{\pm 2.77 \times 10^{-10}}$	$\mathbf{-2.69 \times 10^{-10}}$ $\mathbf{\pm 3.87 \times 10^{-12}}$

3. Conclusion

We prepared and studied the resistive switching phenomena of discontinuous α-Fe_2O_3 thin films in the humid environment. The device exhibits negative differential resistance (NDR) in its I-V curve. With increasing voltage across the sample, the current increases and at ~4 V, starts to decline, i.e., NDR, which is not seen with a low humidity environment. The NDR phenomena is attributed to accumulation of water molecules and their subsequent breakdown, which produces a space charge limited region of the electrode (metal contact). Over the course of 100 cycles of a triangular voltage sweep, the HRS/LRS decreased with the number of cycles, which is attributed to the continuous formation of hydrated α-Fe_2O_3, thereby reducing the HRS over each cycle. Further studies will examine the lifetime of resistive switching and possible causes of the decreasing HRS/LRS over multiple cycles. Furthermore, the sample preparation temperature and the thickness of the film can provide further insights to explain whether the RS and NDR properties are due to bulk or surface in future studies.

CHAPTER VII

QUANTIFICATION OF RELATIVE HUMIDITY BY α-Fe_2O_3 SENSOR

1. Introduction

A humidity sensor is a device that detects and measures the moisture in the environment, which is a complex and difficult problem due to its poor recovery, limited selectivity, limited accuracy, and difficulty in calibration in air [182], [183]. Electrical devices are sensitive to environmental humidity and the device performance would be unintended in the presence of humid air [184], [185] which requires the detection of humidity in air, an application of humidity sensor. The measurement and control of humidity is important to both human comfort and industrial applications [186]–[189]. Humidity sensors are designed to monitor the humidity level by observing the changes in its electrical, optical, or mechanical properties [190]. Examples include changes in resistance [191], [192], capacitance [193]–[195], impedance [186], [196], refractive index [197], [198], phase of surface acoustic wave [199], [200], etc.

A good humidity sensor is characterized by its sensitivity, reversibility, fast response time, long lifetime, high humidity selectivity, chemical and thermal stability [201].

Many material systems have been utilized to construct humidity sensors including ceramics [202], metal oxide/nanocomposites [203]–[205], polyelectrolyte cell [206], and organic polymers [207]–[209]. Due to the easy fabrication, ample abundance, stability in aqueous environment and low cost, spin coated Fe_2O_3 thin films are widely used to construct gas sensors, photoelectrochemical (PEC) cells, and photodetectors [100], [125], [210]–[212].

Examples of humidity sensor using Fe_2O_3 have been reported in the literature [190], [213]–[215]. Chani et al. proposed a simulation that can be used to quantify the relative humidity by using an exponential form of equation [216, p. 3]. In this work, we prepared α- Fe_2O_3 nano porous thin film by using spin coating and introduced a novel way of quantifying humidity in air by the sweeping I-V method by applying a triangular voltage sweep and simultaneously measuring the current. The ratio of high to low resistance state is a change produced by the change in relative humidity of the environment and by using an exponential equation, the relative humidity can be calculated.

2. Results and discussion

The sensor consists of a discontinuous and porous thin film of α-Fe_2O_3. The SEM micrograph in Fig.6.1 (a) and Raman spectra in Fig. 6.1(b) of Chapter VI shows the presence of voids up to ~200 nm size and the presence of α-Fe_2O_3 but not the other forms of iron oxides, respectively. Furthermore, EDX mapping in Fig. 6.2 in chapter VI shows the sparsely distributed α-Fe_2O_3 on glass substrate. Figure 2.8 in Chapter II is a schematic of the sensor experimental setup.

When humid N_2 with relative humidity of 80% is flown on the sensor, it responds with a reduction in resistance. Fig. 7.1 shows the resistance response of the sensor in real time and when the humid N_2 is flown on the sensor. Initially, in the absence of moisture, the resistance of the sensor is in the order of 55 GΩ, but in the presence of H_2O molecules the resistance plummets down to ~5 GΩ. Fig. 7.1 (a) shows the absolute variation of the resistance when exposed to humid N_2 and Fig. 7.1(b) is the relative change in resistance from the baseline, which is over -90%.

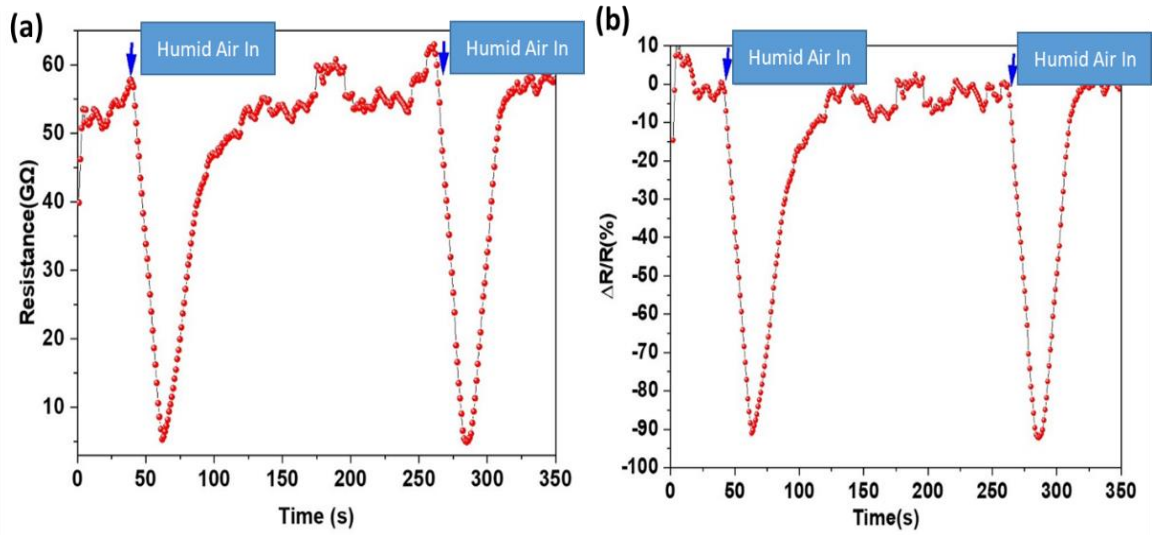

Fig. 7.1: (a) Resistance response of humidity sensor. (b) Relative change in the resistance of the sensor when humid air is introduced.

The sensor response in different humidity environment shows interesting features. I-V characteristics taken in RH 10% to 100% environments by sweeping a triangular voltage at 0.2 V/s shows a hysteresis loop. After RH ~70%, the hysteresis loop is prominently visible which indicates the charge accumulation at the material electrode interface [217], [218]. During the sweep when voltage is increased linearly from 0 V to higher voltages, the sensor takes a LRS initially and at ~4.5 V, for this particular sample, where the

current drops sharply. And while descending from the higher voltage, the sensor takes HRS as shown in fig. 7.2(a). The ratio HRS/LRS for different humidity levels are plotted against relative humidity in fig. 7.2(b).

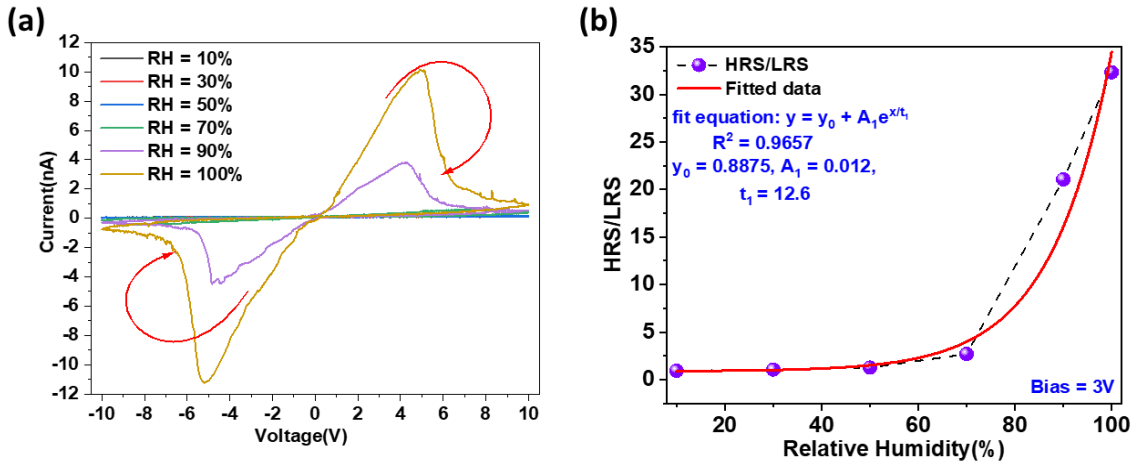

Fig. 7.2: (a) Sweeping I-V curves at different humidity levels of the sensor. (b) Exponential fit of HRS/LRS data from the sweeping I-V for quantification of relative humidity.

In order to quantify the relative humidity, the ratio of HRS/LRS was fitted with an exponential function of the form given by equation (7.1).

$$y = y_0 + A_1 e^{\frac{x}{t_1}} \tag{7.1}$$

In equation (7.1) the independent variable(x) is the relative humidity of the environment and dependent variable(y) is the ratio HRS/LRS. Also, y_0 and A_1 are constants and t_1 is a rate determining parameter. The curve fits well with goodness of fit being > 96%. Solving equation (7.1) for x, we can get equation (7.2) from which the relative humidity of the environment can be quantified.

$$x = t_1 \ln\left(\frac{y - y_0}{A_1}\right) \tag{7.2}$$

Displayed in fig. 7.3 is the capacitance of the sensor as a function of relative humidity. The capacitance of the sensor in dry environment is ~65 pF and increases exponentially with increasing humidity to a high of 77 pF at relative humidity of 100% following an exponential function. The capacitance as a function of relative humidity is also fit with Eq. (7.1), keeping the exponential rate defining parameter constant at t_1= 12.6, as obtained from the fit of the data in Fig. 7.2(b). The data fits with high confidence, implying that the mechanism of sensing is because of charge accumulation at the electrode/metal oxide interface.

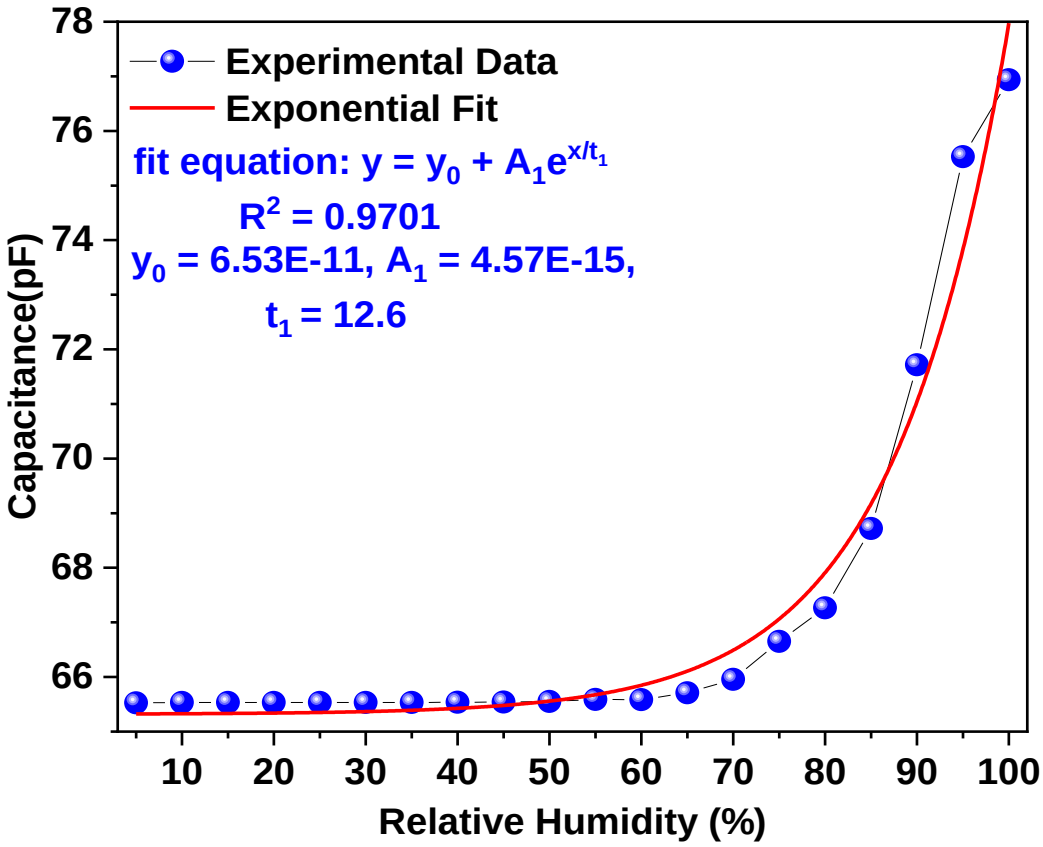

Fig. 7.3: The measured capacitance of the sensor as a function of humidity at 1 kHz and 1 V rms signal.

Once again, the proposed response mechanism is that during the voltage sweep, the H_2O molecules adsorbed onto the sensor and decompose with the application of a sufficiently larger voltages ($\geq$ 1.23 V). The ions, H_3O^+ and OH^-, formed by the decomposition of the H_2O molecules travel towards the respective electrodes and form a space charge region or the charges are trapped at the electrode/metal oxide interface.

3. Conclusion

A porous thin film of α-Fe_2O_3 deposited on glass substrate exhibits excellent humidity sensing capabilities. A novel technique of quantifying the relative humidity of the environment has been applied and successfully validated. With the application of sweeping I-V method, we are able to show that charge trapping at the electrode/metal oxide interface, which corresponds to the area inside the hysteresis formed in the I-V curve, increases exponentially with increasing relative humidity. Capacitance as a function of relative humidity data supports the claim of charge trapping mechanism of sensing in this study. One can fit the data to create a calibration function for the sensor, which can then be used to measure the relative humidity of an unknown environment.

CHAPTER VIII

CONCLUSION

In this dissertation, we studied the electrical and optical properties of ZnO and Fe_2O_3 resistive switching devices on silicon and glass substrates. ZnO double layer device was fabricated using atomic layer deposition and Fe_2O_3 thin film by spin coating. The overall aim of this work is to study the resistive switching behavior of the device, along with its applications in synaptic conductance, photo-detection, and gas sensing. ZnO double layer devices show good diode behavior and are a potential solution for the crosstalk problem in crossbar memory arrays. Fe_2O_3 on p-Si device has excellent visible light photo-detection properties and synaptic potentiation of conductance, whereas Fe_2O_3 on glass substrate has resistive switching behavior with negative differential resistance and is a good humidity sensor.

The ZnO homojunction diode was designed using two electrically dissimilar ZnO thin films, which results in an nn-homojunction with a gradient of vacancies at the interface. The I-V curves of the diode were acquired at different AC frequencies, which exhibited hysteresis in forward bias, a threshold voltage, and rectification in reverse bias - a desired characteristics of a cell in cross bar memory array. The area of the hysteresis loop as a function of bias frequency initially increases, reaches a maximum, and subsequently decreases.

The frequency at which the area of the hysteresis is maximized occurs when a balance of diffusion at lower frequencies is transitioning charge freezing at higher frequencies.

Fe_2O_3 samples grown on p-Si(100) substrates form a p-n junction with excellent, broad photoresponse in the visible range of the light spectrum and with a large zero bias photocurrent and an ultra-fast response time. The p-Si(100) substrate is the dominant carrier transport path because the large resistance of Fe_2O_3 thin film in the order of 50 GΩ, as compared to 500 kΩ of the Si substrate. Increasing the thickness of the Fe_2O_3 layer results in a reduction of the zero-bias photocurrent. This reduction is attributed to the bulk-like nature of the film and favors recombination of carriers before they can diffuse out of the depletion layer of the p-n junction. The ultra-fast response time is due to the fast carrier dynamics in the p-Si(100) substrate. When a periodic voltage (pulse) is applied, the conductance of the sample increases with increasing number of pulses and eventually saturates. This characteristic is analogous to the synaptic potentiation of neurons. A theoretical transport model based on trap assisted tunneling (TAT) and Poole Frenkel emission (PFE) was used to the I-V curve of the junction. We found that at lower voltages (<0.7 V), TAT mechanism dominates, whereas at higher voltages PFE dominates the carrier transport. In addition, we fit the conductance as a function of number of voltage pulses applied in dark and illuminated conditions using the Hill equation in order to extract the number of pulses for synaptic activation. Ultimately, we determined that the device is programmable using the intensity of light illumination. Specifically, the number of voltage pulses first to activate the devices increase with increasing light intensity reaches a maximum and then decreases. The device not only has synaptic potentiation which is the programmability of conductance state with applied

number of electric pulses, but it has programmability of synaptic activation by controlling the intensity of light illumination. The two degrees of programmability show its potential applications in artificial synaptic electronics.

The final study was on Fe_2O_3 thin films grown on glass substrates. Scanning electron microscopy revealed that the films are porous and discontinuous. The I-V characteristics of the device acquired in vacuum and with a triangular voltage waveform is linear (Ohmic) with a resistance in the GΩ range. When the same measurements are acquired in a humid environment, the I-V curve exhibits hysteresis with negative differential resistance (NDR) phenomenon. Based on the theoretical modeling, we have concluded that the hysteresis and NDR behavior is a consequence of space charge limited current arising from the accumulation of charge at the interface between the Fe_2O_3 film and the electrode (electrical contact) due to the electrical breakdown of water molecules. This was verified by the exponential increase in the capacitance of the device as a function of device, i.e., the capacitance as a function of RH can be fit with the same exponential function following the same rate determining parameter or the coefficient in exponent which implies the sensing mechanism to be the accumulation of charge at the sample electrode interface.

We proposed a novel method to quantify relative humidity using the sweeping I-V method. The Fe_2O_3/glass samples show an exponential increase in the ratio of the high resistive state (HRS) to the low resistive state (LRS) with increasing relative humidity (RH). By fitting an exponential growth function to the HRS/LRS ratio as a function of RH, we can extract calibration parameters, thereby quantifying the RH in terms of the HRS/LRS ratio of an unknown environment.

REFERENCES

[1] L. Chua, “Memristor-The missing circuit element,” *IEEE Trans. Circuit Theory*, vol. 18, no. 5, pp. 507–519, 1971, doi: 10.1109/TCT.1971.1083337.

[2] L. Chua, “If it’s pinched it’s a memristor,” *Semicond. Sci. Technol.*, vol. 29, no. 10, p. 104001, Oct. 2014, doi: 10.1088/0268-1242/29/10/104001.

[3] R. S. Williams, “A short history of memristor development.” HP Labs. [Online]. Available: https://regmedia.co.uk/2011/12/22/hp_memristor_history.pdf

[4] C. Ye *et al.*, “Physical Mechanism and Performance Factors of Metal Oxide Based Resistive Switching Memory: A Review,” *J. Mater. Sci. Technol.*, vol. 32, no. 1, pp. 1–11, Jan. 2016, doi: 10.1016/j.jmst.2015.10.018.

[5] A. Sawa, “Resistive switching in transition metal oxides,” *Mater. Today*, vol. 11, no. 6, pp. 28–36, Jun. 2008, doi: 10.1016/S1369-7021(08)70119-6.

[6] M. J. Rozenberg, M. J. Sánchez, R. Weht, C. Acha, F. Gomez-Marlasca, and P. Levy, “Mechanism for bipolar resistive switching in transition-metal oxides,” *Phys. Rev. B*, vol. 81, no. 11, p. 115101, Mar. 2010, doi: 10.1103/PhysRevB.81.115101.

[7] S. La Barbera, D. Vuillaume, and F. Alibart, “Filamentary Switching: Synaptic Plasticity through Device Volatility,” *ACS Nano*, vol. 9, no. 1, pp. 941–949, Jan. 2015, doi: 10.1021/nn506735m.

[8] A. Chanthbouala *et al.*, “A ferroelectric memristor,” *Nat. Mater.*, vol. 11, no. 10, pp. 860–864, Oct. 2012, doi: 10.1038/nmat3415.

[9] M. A. Caldwell, R. G. D. Jeyasingh, H.-S. P. Wong, and D. J. Milliron, “Nanoscale phase change memory materials,” *Nanoscale*, vol. 4, no. 15, p. 4382, 2012, doi: 10.1039/c2nr30541k.

[10] S. Raoux, F. Xiong, M. Wuttig, and E. Pop, “Phase change materials and phase change memory,” *MRS Bull.*, vol. 39, no. 8, pp. 703–710, Aug. 2014, doi: 10.1557/mrs.2014.139.

[11] H.-S. P. Wong *et al.*, “Phase Change Memory,” *Proc. IEEE*, vol. 98, no. 12, pp. 2201–2227, Dec. 2010, doi: 10.1109/JPROC.2010.207005.

[12] T. Prodromakis and C. Toumazou, “A review on memristive devices and applications,” in *2010 17th IEEE International Conference on Electronics, Circuits and Systems*, Athens, Greece, Dec. 2010, pp. 934–937. doi: 10.1109/ICECS.2010.5724666.

[13] D. Sacchetto, P. Gaillardon, M. Zervas, S. Carrara, G. De Micheli, and Y. Leblebici, “Applications of Multi-Terminal Memristive Devices: A Review,” *IEEE Circuits Syst. Mag.*, vol. 13, no. 2, pp. 23–41, 2013, doi: 10.1109/MCAS.2013.2256258.

[14] Sangho Shin, Kyungmin Kim, and Sung-Mo Kang, “Memristor Applications for Programmable Analog ICs,” *IEEE Trans. Nanotechnol.*, vol. 10, no. 2, pp. 266–274, Mar. 2011, doi: 10.1109/TNANO.2009.2038610.

[15] Y. V. Pershin and M. Di Ventra, “Practical Approach to Programmable Analog Circuits With Memristors,” *IEEE Trans. Circuits Syst. Regul. Pap.*, vol. 57, no. 8, pp. 1857–1864, Aug. 2010, doi: 10.1109/TCSI.2009.2038539.

[16] S. Kvatinsky *et al.*, “MAGIC—Memristor-Aided Logic,” *IEEE Trans. Circuits Syst. II Express Briefs*, vol. 61, no. 11, pp. 895–899, Nov. 2014, doi: 10.1109/TCSII.2014.2357292.

[17] S. H. Jo, T. Chang, I. Ebong, B. B. Bhadviya, P. Mazumder, and W. Lu, “Nanoscale Memristor Device as Synapse in Neuromorphic Systems,” *Nano Lett.*, vol. 10, no. 4, pp. 1297–1301, Apr. 2010, doi: 10.1021/nl904092h.

[18] B. Linares-Barranco and T. Serrano-Gotarredona, “Memristance can explain Spike-Time-Dependent-Plasticity in Neural Synapses,” *Nat. Preced.*, Mar. 2009, doi: 10.1038/npre.2009.3010.1.

[19] T. Serrano-Gotarredona, T. Masquelier, T. Prodromakis, G. Indiveri, and B. Linares-Barranco, “STDP and STDP variations with memristors for spiking neuromorphic learning systems,” *Front. Neurosci.*, vol. 7, 2013, doi: 10.3389/fnins.2013.00002.

[20] Y. V. Pershin and M. D. Ventra, “Experimental demonstration of associative memory with memristive neural networks,” *Nat. Preced.*, p. 19, 2009.

[21] X. Liu, Z. Zeng, and S. Wen, “Implementation of Memristive Neural Network With Full-Function Pavlov Associative Memory,” *IEEE Trans. Circuits Syst. Regul. Pap.*, vol. 63, no. 9, pp. 1454–1463, Sep. 2016, doi: 10.1109/TCSI.2016.2570819.

[22] R. Jiang, P. Ma, Z. Han, and X. Du, “Habituation/Fatigue behavior of a synapse memristor based on IGZO–HfO2 thin film,” *Sci. Rep.*, vol. 7, no. 1, p. 9354, Dec. 2017, doi: 10.1038/s41598-017-09762-5.

[23] L. D. Bastatas, E. Echeverria-Mora, P. Wagle, P. Mainali, A. Austin, and D. N. McIlroy, “Emergent Electrical Properties of Ensembles of 1D Nanostructures and Their Impact on Room Temperature Electrical Sensing of Ammonium Nitrate Vapor,” *ACS Sens.*, vol. 3, no. 11, pp. 2367–2374, Nov. 2018, doi: 10.1021/acssensors.8b00746.

[24] S. J. Lim, S. Kwon, and H. Kim, “ZnO thin films prepared by atomic layer deposition and rf sputtering as an active layer for thin film transistor,” *Thin Solid Films*, vol. 516, no. 7, pp. 1523–1528, Feb. 2008, doi: 10.1016/j.tsf.2007.03.144.

[25] Y.-C. Cheng, K.-Y. Yuan, and M.-J. Chen, “ZnO thin films prepared by atomic layer deposition at various temperatures from 100 to 180 °C with three-pulsed precursors in every growth cycle,” *J. Alloys Compd.*, vol. 685, pp. 391–394, Nov. 2016, doi: 10.1016/j.jallcom.2016.05.289.

[26] D. Kim, H. Kang, J.-M. Kim, and H. Kim, “The properties of plasma-enhanced atomic layer deposition (ALD) ZnO thin films and comparison with thermal ALD,” *Appl. Surf. Sci.*, vol. 257, no. 8, pp. 3776–3779, Feb. 2011, doi: 10.1016/j.apsusc.2010.11.138.

[27] S.-Y. Pung, K.-L. Choy, X. Hou, and C. Shan, “Preferential growth of ZnO thin films by the atomic layer deposition technique,” *Nanotechnology*, vol. 19, no. 43, p. 435609, Oct. 2008, doi: 10.1088/0957-4484/19/43/435609.

[28] K.-M. Kang and H.-H. Park, “Effect of Atomic Layer Deposition Temperature on the Growth Orientation, Morphology, and Electrical, Optical, and Band-Structural Properties of ZnO and Fluorine-Doped ZnO Thin Films,” *J. Phys. Chem. C*, vol. 122, no. 1, pp. 377–385, Jan. 2018, doi: 10.1021/acs.jpcc.7b08943.

[29] B. Weng, J. Wang, P. Larson, and Y. Liu, “Growth process optimization of ZnO thin film using atomic layer deposition,” *Mater. Res. Express*, vol. 3, no. 12, p. 126402, Dec. 2016, doi: 10.1088/2053-1591/3/12/126402.

[30] A. B. Arons and M. B. Peppard, “Einstein’s Proposal of the Photon Concept—a Translation of the Annalen der Physik Paper of 1905,” *Am. J. Phys.*, vol. 33, no. 5, pp. 367–374, May 1965, doi: 10.1119/1.1971542.

[31] S. Hofmann, “Practical surface analysis: state of the art and recent developments in AES, XPS, ISS and SIMS,” *Surf. Interface Anal.*, vol. 9, no. 1, pp. 3–20, Jul. 1986, doi: 10.1002/sia.740090104.

[32] J. Lefebvre, F. Galli, C. L. Bianchi, G. S. Patience, and D. C. Boffito, “Experimental methods in chemical engineering: X-ray photoelectron spectroscopy-XPS,” *Can. J. Chem. Eng.*, vol. 97, no. 10, pp. 2588–2593, Oct. 2019, doi: 10.1002/cjce.23530.

[33] R. Morent, N. De Geyter, C. Leys, L. Gengembre, and E. Payen, “Comparison between XPS- and FTIR-analysis of plasma-treated polypropylene film surfaces,” *Surf. Interface Anal.*, vol. 40, no. 3–4, pp. 597–600, Mar. 2008, doi: 10.1002/sia.2619.

[34] G. Greczynski and L. Hultman, “X-ray photoelectron spectroscopy: Towards reliable binding energy referencing,” *Prog. Mater. Sci.*, vol. 107, p. 100591, Jan. 2020, doi: 10.1016/j.pmatsci.2019.100591.

[35] S. Hofmann, *Auger- and X-Ray Photoelectron Spectroscopy in Materials Science*, vol. 49. Berlin, Heidelberg: Springer Berlin Heidelberg, 2013. doi: 10.1007/978-3-642-27381-0.

[36] E. Echeverría *et al.*, “Strong binding at the gold (Au) boron carbide interface,” *Surf. Coat. Technol.*, vol. 314, pp. 51–54, Mar. 2017, doi: 10.1016/j.surfcoat.2016.08.081.

[37] N. Fairly, “CasaXPS: processing software for XPS, AES, SIMS and More.” http://www.casaxps.com/

[38] J. Végh, “The Shirley background revised,” *J. Electron Spectrosc. Relat. Phenom.*, vol. 151, no. 3, pp. 159–164, May 2006, doi: 10.1016/j.elspec.2005.12.002.

[39] “Scanning Electron Microscope A To Z,” p. 32.

[40] A. Mohammed and A. Abdullah, “SCANNING ELECTRON MICROSCOPY (SEM): A REVIEW,” p. 9.

[41] J. I. Goldstein *et al.*, *Scanning Electron Microscopy and X-ray Microanalysis*. Boston, MA: Springer US, 2003. doi: 10.1007/978-1-4615-0215-9.

[42] M. Abd Mutalib, M. A. Rahman, M. H. D. Othman, A. F. Ismail, and J. Jaafar, “Scanning Electron Microscopy (SEM) and Energy-Dispersive X-Ray (EDX) Spectroscopy,” in *Membrane Characterization*, Elsevier, 2017, pp. 161–179. doi: 10.1016/B978-0-444-63776-5.00009-7.

[43] R. K. Mishra, A. K. Zachariah, and S. Thomas, “Energy-Dispersive X-ray Spectroscopy Techniques for Nanomaterial,” in *Microscopy Methods in Nanomaterials Characterization*, Elsevier, 2017, pp. 383–405. doi: 10.1016/B978-0-323-46141-2.00012-2.

[44] G. S. Bumbrah and R. M. Sharma, “Raman spectroscopy – Basic principle, instrumentation and selected applications for the characterization of drugs of abuse,” *Egypt. J. Forensic Sci.*, vol. 6, no. 3, pp. 209–215, Sep. 2016, doi: 10.1016/j.ejfs.2015.06.001.

[45] J. R. Ferraro, K. Nakamoto, and C. W. Brown, *Introductory Raman spectroscopy*, 2nd ed. Amsterdam ; Boston: Academic Press, 2003.

[46] Y. Singh, "ELECTRICAL RESISTIVITY MEASUREMENTS: A REVIEW," *Int. J. Mod. Phys. Conf. Ser.*, vol. 22, pp. 745–756, Jan. 2013, doi: 10.1142/S2010194513010970.

[47] F. M. Smits, "Measurement of Sheet Resistivities with the Four-Point Probe," p. 8.

[48] L. J. Swartzendruber, "Four-point probe measurement of non-uniformities in semiconductor sheet resistivity," *Solid-State Electron.*, vol. 7, no. 6, pp. 413–422, Jun. 1964, doi: 10.1016/0038-1101(64)90038-3.

[49] H. B. Michaelson, "The work function of the elements and its periodicity," *J Appl Phys*, vol. 48, no. 11, p. 6, 1977.

[50] M. A. Butler and D. S. Ginley, "Prediction of Flatband Potentials at Semiconductor-Electrolyte Interfaces from Atomic Electronegativities," *J. Electrochem. Soc.*, vol. 125, no. 2, pp. 228–232, Feb. 1978, doi: 10.1149/1.2131419.

[51] W. Lu, K.-H. Kim, T. Chang, and S. Gaba, "Two-terminal resistive switches (memristors) for memory and logic applications," in *16th Asia and South Pacific Design Automation Conference (ASP-DAC 2011)*, Yokohama, Japan, Jan. 2011, pp. 217–223. doi: 10.1109/ASPDAC.2011.5722187.

[52] M.-J. Lee *et al.*, "2-stack ID-IR Cross-point Structure with Oxide Diodes as Switch Elements for High Density Resistance RAM Applications," p. 4.

[53] Y. Li, Z. Wang, R. Midya, Q. Xia, and J. J. Yang, "Review of memristor devices in neuromorphic computing: materials sciences and device challenges," *J. Phys. Appl. Phys.*, vol. 51, no. 50, p. 503002, Dec. 2018, doi: 10.1088/1361-6463/aade3f.

[54] X. Guan and S. Yu, "On the Switching Parameter Variation of Metal-Oxide RRAM—Part I: Physical Modeling and Simulation Methodology," *IEEE Trans. ELECTRON DEVICES*, vol. 59, no. 4, p. 11, 2012.

[55] S. Yu, "On the Switching Parameter Variation of Metal Oxide RRAM—Part II: Model Corroboration and Device Design Strategy," *IEEE Trans. ELECTRON DEVICES*, vol. 59, no. 4, p. 6, 2012.

[56] D. Lee *et al.*, "Excellent uniformity and reproducible resistance switching characteristics of doped binary metal oxides for non-volatile resistance memory

applications," in *2006 International Electron Devices Meeting*, San Francisco, CA, USA, 2006, pp. 1–4. doi: 10.1109/IEDM.2006.346733.

[57] S.-M. Lin *et al.*, "Single-Step Formation of ZnO/ZnWO $_x$ Bilayer Structure via Interfacial Engineering for High Performance and Low Energy Consumption Resistive Memory with Controllable High Resistance States," *ACS Appl. Mater. Interfaces*, vol. 5, no. 16, pp. 7831–7837, Aug. 2013, doi: 10.1021/am4016928.

[58] R. Mundle, C. Carvajal, and A. K. Pradhan, "ZnO/Al:ZnO Transparent Resistive Switching Devices Grown by Atomic Layer Deposition for Memristor Applications," *Langmuir*, vol. 32, no. 19, pp. 4983–4995, May 2016, doi: 10.1021/acs.langmuir.6b01014.

[59] S. Lee, H. Kim, D.-J. Yun, S.-W. Rhee, and K. Yong, "Resistive switching characteristics of ZnO thin film grown on stainless steel for flexible nonvolatile memory devices," *Appl. Phys. Lett.*, vol. 95, no. 26, p. 262113, Dec. 2009, doi: 10.1063/1.3280864.

[60] N. Xu *et al.*, "Characteristics and mechanism of conduction/set process in TiN⁄ZnO⁄Pt resistance switching random-access memories," *Appl Phys Lett*, p. 4.

[61] K. Mohanta, S. K. Batabyal, and A. J. Pal, "*pn* -Junction Rectifiers Based on *p* -ZnO and *n* -ZnO Nanoparticles," *Chem. Mater.*, vol. 19, no. 15, pp. 3662–3666, Jul. 2007, doi: 10.1021/cm070258p.

[62] L. G. Mar, P. Y. Timbrell, and R. N. Lamb, "An XPS study of zinc oxide thin film growth on copper using zinc acetate as a precursor," *Thin Solid Films*, vol. 223, no. 2, pp. 341–347, Feb. 1993, doi: 10.1016/0040-6090(93)90542-W.

[63] J. Zang, Z.-H. Xu, R. A. Webb, and X. Li, "Electrical Self-Healing of Mechanically Damaged Zinc Oxide Nanobelts," *Nano Lett.*, vol. 11, no. 1, pp. 241–244, Jan. 2011, doi: 10.1021/nl103637k.

[64] L. D. Bastatas, P. Wagle, E. Echeverria, J. D. Slinker, and D. N. McIlroy, "Electrical characterization of ZnO-coated nanospring ensemble by impedance spectroscopy: probing the effect of thermal annealing," *Nanotechnology*, vol. 30, no. 23, p. 234006, Jun. 2019, doi: 10.1088/1361-6528/ab087c.

[65] H. S. Kang, J. S. Kang, S. S. Pang, E. S. Shim, and S. Y. Lee, "Variation of light emitting properties of ZnO thin films depending on post-annealing temperature," *Mater. Sci. Eng. B*, vol. 102, no. 1–3, pp. 313–316, Sep. 2003, doi: 10.1016/S0921-5107(02)00730-4.

[66] A. Pérez-Tomás *et al.*, “Characterization and modeling of n-n Si⁄SiC heterojunction diodes,” *J. Appl. Phys.*, vol. 102, no. 1, p. 014505, Jul. 2007, doi: 10.1063/1.2752148.

[67] S. P. Adhikari, M. Pd. Sah, H. Kim, and L. O. Chua, “Three Fingerprints of Memristor,” *IEEE Trans. Circuits Syst. Regul. Pap.*, vol. 60, no. 11, pp. 3008–3021, Nov. 2013, doi: 10.1109/TCSI.2013.2256171.

[68] I. Orak, A. Kocyigit, and Ş. Alindal, “Electrical and dielectric characterization of Au/ZnO/n–Si device depending frequency and voltage,” *Chin. Phys. B*, vol. 26, no. 2, p. 028102, Feb. 2017, doi: 10.1088/1674-1056/26/2/028102.

[69] Y. Sun, X. Yan, X. Zheng, Y. Liu, Y. Shen, and Y. Zhang, “Influence of carrier concentration on the resistive switching characteristics of a ZnO-based memristor,” *Nano Res.*, vol. 9, no. 4, pp. 1116–1124, Apr. 2016, doi: 10.1007/s12274-016-1006-0.

[70] C. Bao *et al.*, “High Performance and Stable All-Inorganic Metal Halide Perovskite-Based Photodetectors for Optical Communication Applications,” *Adv. Mater.*, vol. 30, no. 38, p. 1803422, Sep. 2018, doi: 10.1002/adma.201803422.

[71] C. Danakis, M. Afgani, G. Povey, I. Underwood, and H. Haas, “Using a CMOS camera sensor for visible light communication,” in *2012 IEEE Globecom Workshops*, Anaheim, CA, USA, Dec. 2012, pp. 1244–1248. doi: 10.1109/GLOCOMW.2012.6477759.

[72] A. Poglitsch *et al.*, “The Photodetector Array Camera and Spectrometer (PACS) on the *Herschel* Space Observatory,” *Astron. Astrophys.*, vol. 518, p. L2, Jul. 2010, doi: 10.1051/0004-6361/201014535.

[73] T. Okino *et al.*, “A Real-Time Ultraviolet Radiation Imaging System Using an Organic Photoconductive Image Sensor,” *Sensors*, vol. 18, no. 1, p. 314, Jan. 2018, doi: 10.3390/s18010314.

[74] G. Llosá, “Recent developments in photodetection for medical applications,” *Nucl. Instrum. Methods Phys. Res. Sect. Accel. Spectrometers Detect. Assoc. Equip.*, vol. 787, pp. 353–357, Jul. 2015, doi: 10.1016/j.nima.2015.01.071.

[75] S. Cai, X. Xu, W. Yang, J. Chen, and X. Fang, “Materials and Designs for Wearable Photodetectors,” *Adv. Mater.*, vol. 31, no. 18, p. 1808138, May 2019, doi: 10.1002/adma.201808138.

[76] S. Ng *et al.*, “Photoelectrochemical ultraviolet photodetector by anodic titanium dioxide nanotube layers,” *Sens. Actuators Phys.*, vol. 279, pp. 263–271, Aug. 2018, doi: 10.1016/j.sna.2018.06.030.

[77] M. I. Zappia *et al.*, “Solution-Processed GaSe Nanoflake-Based Films for Photoelectrochemical Water Splitting and Photoelectrochemical-Type Photodetectors,” *Adv. Funct. Mater.*, vol. 30, no. 10, p. 1909572, Mar. 2020, doi: 10.1002/adfm.201909572.

[78] A. Bera, A. Das Mahapatra, S. Mondal, and D. Basak, “Sb $_2$ S $_3$ /Spiro-OMeTAD Inorganic–Organic Hybrid p–n Junction Diode for High Performance Self-Powered Photodetector,” *ACS Appl. Mater. Interfaces*, vol. 8, no. 50, pp. 34506–34512, Dec. 2016, doi: 10.1021/acsami.6b09943.

[79] L. Hu *et al.*, “Defect Reconstruction Triggered Full-Color Photodetection in Single Nanowire Phototransistor,” *ACS Photonics*, vol. 6, no. 4, pp. 886–894, Apr. 2019, doi: 10.1021/acsphotonics.8b01471.

[80] C. Xie, C. Liu, H. Loi, and F. Yan, “Perovskite-Based Phototransistors and Hybrid Photodetectors,” *Adv. Funct. Mater.*, vol. 30, no. 20, p. 1903907, May 2020, doi: 10.1002/adfm.201903907.

[81] M. F. Al-Kuhaili, M. Saleem, and S. M. A. Durrani, “Optical properties of iron oxide (α-Fe2O3) thin films deposited by the reactive evaporation of iron,” *J. Alloys Compd.*, vol. 521, pp. 178–182, Apr. 2012, doi: 10.1016/j.jallcom.2012.01.115.

[82] K. Sivula, F. Le Formal, and M. Grätzel, “Solar Water Splitting: Progress Using Hematite (α-Fe2O3) Photoelectrodes,” *ChemSusChem*, vol. 4, no. 4, pp. 432–449, Apr. 2011, doi: 10.1002/cssc.201000416.

[83] S. Saritas, M. Kundakci, O. Coban, S. Tuzemen, and M. Yildirim, “Ni: Fe 2 O 3 , Mg: Fe 2 O 3 and Fe 2 O 3 thin films gas sensor application,” *Phys. B Condens. Matter*, vol. 541, pp. 14–18, Jul. 2018, doi: 10.1016/j.physb.2018.04.028.

[84] J. Chen, L. Xu, W. Li, and X. Gou, ?“-Fe2O3 Nanotubes in Gas Sensor and Lithium-Ion Battery Applications,” *Adv. Mater.*, vol. 17, no. 5, pp. 582–586, Mar. 2005, doi: 10.1002/adma.200401101.

[85] F. Bondioli, A. M. Ferrari, C. Leonelli, and T. Manfredini, “Syntheses of Fe2O3/Silica Red Inorganic Inclusion Pigments for Ceramic Applications,” *Mater. Res. Bull.*, vol. 33, no. 5, pp. 723–729, May 1998, doi: 10.1016/S0025-5408(98)00047-6.

[86] Q. Liu, Z.-M. Cui, Z. Ma, S.-W. Bian, W.-G. Song, and L.-J. Wan, “Morphology control of Fe $_2$ O $_3$ nanocrystals and their application in catalysis,” *Nanotechnology*, vol. 18, no. 38, p. 385605, Sep. 2007, doi: 10.1088/0957-4484/18/38/385605.

[87] F. J. Morin, “Electrical Properties of α - Fe 2 O 3,” *Phys. Rev.*, vol. 93, no. 6, pp. 1195–1199, Mar. 1954, doi: 10.1103/PhysRev.93.1195.

[88] N. J. Cherepy, D. B. Liston, J. A. Lovejoy, H. Deng, and J. Z. Zhang, “Ultrafast Studies of Photoexcited Electron Dynamics in γ- and r-Fe2O3 Semiconductor Nanoparticles,” p. 7.

[89] T. Sa, G. Wu, N. Qin, and D. Bao, “Solution processed highly sensitive visible-light photodetectors based on α-Fe2O3/p-Si heterojunctions,” *Sens. Actuators B Chem.*, vol. 173, pp. 414–418, Oct. 2012, doi: 10.1016/j.snb.2012.07.027.

[90] I. Chamritski and G. Burns, “Infrared- and Raman-Active Phonons of Magnetite, Maghemite, and Hematite: A Computer Simulation and Spectroscopic Study,” *J. Phys. Chem. B*, vol. 109, no. 11, pp. 4965–4968, Mar. 2005, doi: 10.1021/jp048748h.

[91] S. Das and M. J. Hendry, “Application of Raman spectroscopy to identify iron minerals commonly found in mine wastes,” *Chem. Geol.*, vol. 290, no. 3–4, pp. 101–108, Nov. 2011, doi: 10.1016/j.chemgeo.2011.09.001.

[92] D. Bersani, P. P. Lottici, and A. Montenero, “Micro-Raman investigation of iron oxide films and powders produced by sol–gel syntheses,” *J Raman Spectrosc*, p. 6, 1999.

[93] “Raman microspectroscopy of some iron oxides and oxyhydroxides,” *J Raman Spectrosc*, vol. 28, p. 6, 1997.

[94] B. Li, D. Yu, and S.-L. Zhang, “Raman spectral study of silicon nanowires,” p. 4.

[95] Y. Zhao, C. Li, and L. Shen, “Recent research process on perovskite photodetectors: A review for photodetector—materials, physics, and applications,” *Chin. Phys. B*, vol. 27, no. 12, p. 127806, Dec. 2018, doi: 10.1088/1674-1056/27/12/127806.

[96] J. Yao, Z. Deng, Z. Zheng, and G. Yang, “Stable, Fast UV–Vis–NIR Photodetector with Excellent Responsivity, Detectivity, and Sensitivity Based on α-In_2Te_3 Films with a Direct Bandgap,” *ACS Appl. Mater. Interfaces*, vol. 8, no. 32, pp. 20872–20879, Aug. 2016, doi: 10.1021/acsami.6b06222.

[97] M. van Exter and D. Grischkowsky, “Carrier dynamics of electrons and holes in moderately doped silicon,” *Phys. Rev. B*, vol. 41, no. 17, pp. 12140–12149, Jun. 1990, doi: 10.1103/PhysRevB.41.12140.

[98] F. E. Rougieux *et al.*, “Electron and hole mobility reduction and Hall factor in phosphorus-compensated p-type silicon,” *J. Appl. Phys.*, vol. 108, no. 1, p. 013706, Jul. 2010, doi: 10.1063/1.3456076.

[99] P.-H. Chung, C.-T. Kuo, T.-H. Wang, Y.-Y. Lu, C.-I. Liu, and T.-R. Yew, “A Sensitive Visible Light Photodetector Using Cobalt-Doped Zinc Ferrite Oxide Thin

Films," *ACS Appl. Mater. Interfaces*, vol. 13, no. 5, pp. 6411–6420, Feb. 2021, doi: 10.1021/acsami.0c20487.

[100] A. D. Nusseif, A. M. Abdul-Majeed, and N. S. Hameed, "Synthesis and Characterization of α- Fe2O3 NPs/P-Si Heterojunction for High Sensitive Photodetector," *Silicon*, vol. 14, no. 4, pp. 1817–1821, Feb. 2022, doi: 10.1007/s12633-021-00971-2.

[101] N. Kamarulzaman, N. Badar, N. F. Chayed, and M. F. Kasim, "Band gap widening and quantum tunnelling effects of Ag/MgO/p-Si MOS structure," *Mater. Res. Express*, vol. 3, no. 10, p. 106401, Oct. 2016, doi: 10.1088/2053-1591/3/10/106401.

[102] D. Seok Jeong, I. Kim, M. Ziegler, and H. Kohlstedt, "Towards artificial neurons and synapses: a materials point of view," *RSC Adv.*, vol. 3, no. 10, p. 3169, 2013, doi: 10.1039/c2ra22507g.

[103] D. Kuzum, S. Yu, and H.-S. Philip Wong, "Synaptic electronics: materials, devices and applications," *Nanotechnology*, vol. 24, no. 38, p. 382001, Sep. 2013, doi: 10.1088/0957-4484/24/38/382001.

[104] D. Li *et al.*, "MoS_2 Memristors Exhibiting Variable Switching Characteristics toward Biorealistic Synaptic Emulation," *ACS Nano*, vol. 12, no. 9, pp. 9240–9252, Sep. 2018, doi: 10.1021/acsnano.8b03977.

[105] X. Yang *et al.*, "An organic terpyridyl-iron polymer based memristor for synaptic plasticity and learning behavior simulation," *RSC Adv.*, vol. 6, no. 30, pp. 25179–25184, 2016, doi: 10.1039/C6RA02915A.

[106] G. Lee, J. Baek, F. Ren, S. J. Pearton, G. Lee, and J. Kim, "Artificial Neuron and Synapse Devices Based on 2D Materials," *Small*, vol. 17, no. 20, p. 2100640, May 2021, doi: 10.1002/smll.202100640.

[107] C. Zhang *et al.*, "Recent progress in memristors for stimulating synaptic plasticity," *Sci. Sin. Informationis*, vol. 48, no. 2, pp. 115–142, Feb. 2018, doi: 10.1360/N112017-00022.

[108] F. A. C. Azevedo *et al.*, "Equal numbers of neuronal and nonneuronal cells make the human brain an isometrically scaled-up primate brain," *J. Comp. Neurol.*, vol. 513, no. 5, pp. 532–541, Apr. 2009, doi: 10.1002/cne.21974.

[109] S. Brotherson, "Understanding Brain Development in Young Children," p. 8.

[110] L. Zhao *et al.*, “Multi-level control of conductive nano-filament evolution in HfO 2 ReRAM by pulse-train operations,” *Nanoscale*, vol. 6, no. 11, pp. 5698–5702, 2014, doi: 10.1039/C4NR00500G.

[111] S. Park *et al.*, “Neuromorphic speech systems using advanced ReRAM-based synapse,” in *2013 IEEE International Electron Devices Meeting*, Washington, DC, USA, Dec. 2013, p. 25.6.1-25.6.4. doi: 10.1109/IEDM.2013.6724692.

[112] R. Waser, R. Dittmann, G. Staikov, and K. Szot, “Redox-Based Resistive Switching Memories - Nanoionic Mechanisms, Prospects, and Challenges,” *Adv. Mater.*, vol. 21, no. 25–26, pp. 2632–2663, Jul. 2009, doi: 10.1002/adma.200900375.

[113] I. Valov and M. N. Kozicki, “Cation-based resistance change memory,” *J. Phys. Appl. Phys.*, vol. 46, no. 7, p. 074005, Feb. 2013, doi: 10.1088/0022-3727/46/7/074005.

[114] T. Tuma, A. Pantazi, M. Le Gallo, A. Sebastian, and E. Eleftheriou, “Stochastic phase-change neurons,” *Nat. Nanotechnol.*, vol. 11, no. 8, pp. 693–699, Aug. 2016, doi: 10.1038/nnano.2016.70.

[115] L. Sun, W. Wang, and H. Yang, “Recent Progress in Synaptic Devices Based on 2D Materials,” *Adv. Intell. Syst.*, vol. 2, no. 5, p. 1900167, May 2020, doi: 10.1002/aisy.201900167.

[116] E. Covi, S. Brivio, M. Fanciulli, and S. Spiga, “Synaptic potentiation and depression in Al:HfO2-based memristor,” *Microelectron. Eng.*, vol. 147, pp. 41–44, Nov. 2015, doi: 10.1016/j.mee.2015.04.052.

[117] K. Seo *et al.*, “Analog memory and spike-timing-dependent plasticity characteristics of a nanoscale titanium oxide bilayer resistive switching device,” *Nanotechnology*, vol. 22, no. 25, p. 254023, Jun. 2011, doi: 10.1088/0957-4484/22/25/254023.

[118] H. Choi *et al.*, “An electrically modifiable synapse array of resistive switching memory,” *Nanotechnology*, vol. 20, no. 34, p. 345201, Aug. 2009, doi: 10.1088/0957-4484/20/34/345201.

[119] T. Chang, S.-H. Jo, and W. Lu, “Short-Term Memory to Long-Term Memory Transition in a Nanoscale Memristor,” *ACS Nano*, vol. 5, no. 9, pp. 7669–7676, Sep. 2011, doi: 10.1021/nn202983n.

[120] S. Yu, Y. Wu, R. Jeyasingh, D. Kuzum, and H.-S. P. Wong, “An Electronic Synapse Device Based on Metal Oxide Resistive Switching Memory for Neuromorphic Computation,” *IEEE Trans. Electron Devices*, vol. 58, no. 8, pp. 2729–2737, Aug. 2011, doi: 10.1109/TED.2011.2147791.

[121] Y. Wu *et al.*, "AlOx-Based Resistive Switching Device with Gradual Resistance Modulation for Neuromorphic Device Application," in *2012 4th IEEE International Memory Workshop*, Milan, Italy, May 2012, pp. 1–4. doi: 10.1109/IMW.2012.6213663.

[122] "An Overview of the Abundance, Relative Mobility, Bioavailability, and Human Toxicity of Metals," in *The Environmental Geochemistry of Mineral Deposits*, Society of Economic Geologists, 1997, pp. 29–70. doi: 10.5382/Rev.06.02.

[123] C. Xia, Y. Jia, M. Tao, and Q. Zhang, "Tuning the band gap of hematite α-Fe2O3 by sulfur doping," *Phys. Lett. A*, vol. 377, no. 31–33, pp. 1943–1947, Oct. 2013, doi: 10.1016/j.physleta.2013.05.026.

[124] P. Sharma, J. Jang, and J. S. Lee, "Key Strategies to Advance the Photoelectrochemical Water Splitting Performance of α-Fe $_2$ O $_3$ Photoanode," *ChemCatChem*, vol. 11, no. 1, pp. 157–179, Jan. 2019, doi: 10.1002/cctc.201801187.

[125] A. Mirzaei, B. Hashemi, and K. Janghorban, "α-Fe2O3 based nanomaterials as gas sensors," *J. Mater. Sci. Mater. Electron.*, vol. 27, no. 4, pp. 3109–3144, Apr. 2016, doi: 10.1007/s10854-015-4200-z.

[126] G. Zhou, X. Yang, L. Xiao, B. Sun, and A. Zhou, "Investigation of a submerging redox behavior in Fe $_2$ O $_3$ solid electrolyte for resistive switching memory," *Appl. Phys. Lett.*, vol. 114, no. 16, p. 163506, Apr. 2019, doi: 10.1063/1.5089147.

[127] X. Ji *et al.*, "Mimicking associative learning using an ion-trapping non-volatile synaptic organic electrochemical transistor," *Nat. Commun.*, vol. 12, no. 1, p. 2480, Dec. 2021, doi: 10.1038/s41467-021-22680-5.

[128] G.-J. A. H. Wetzelaer, M. Scheepers, A. M. Sempere, C. Momblona, J. Ávila, and H. J. Bolink, "Trap-Assisted Non-Radiative Recombination in Organic-Inorganic Perovskite Solar Cells," *Adv. Mater.*, vol. 27, no. 11, pp. 1837–1841, Mar. 2015, doi: 10.1002/adma.201405372.

[129] Z. Wu *et al.*, "A Habituation Sensory Nervous System with Memristors," *Adv. Mater.*, vol. 32, no. 46, p. 2004398, Nov. 2020, doi: 10.1002/adma.202004398.

[130] E. Lim and R. Ismail, "Conduction Mechanism of Valence Change Resistive Switching Memory: A Survey," *Electronics*, vol. 4, no. 3, pp. 586–613, Sep. 2015, doi: 10.3390/electronics4030586.

[131] F.-C. Chiu, "A Review on Conduction Mechanisms in Dielectric Films," *Adv. Mater. Sci. Eng.*, vol. 2014, pp. 1–18, 2014, doi: 10.1155/2014/578168.

[132] A. Gehring, “ausgeführt zum Zwecke der Erlangung des akademischen Grades eines Doktors der technischen Wissenschaften,” p. 178.

[133] M. P. Houng, Y. H. Wang, and W. J. Chang, “Current transport mechanism in trapped oxides: A generalized trap-assisted tunneling model,” *J. Appl. Phys.*, vol. 86, no. 3, pp. 1488–1491, Aug. 1999, doi: 10.1063/1.370918.

[134] I. Vourkas, A. Batsos, and G. Ch. Sirakoulis, “SPICE modeling of nonlinear memristive behavior: MEMRISTOR SPICE MODELING,” *Int. J. Circuit Theory Appl.*, vol. 43, no. 5, pp. 553–565, May 2015, doi: 10.1002/cta.1957.

[135] B. Sun, M. Xiao, G. Zhou, Z. Ren, Y. N. Zhou, and Y. A. Wu, “Non–zero-crossing current-voltage hysteresis behavior in memristive system,” *Mater. Today Adv.*, vol. 6, p. 100056, Jun. 2020, doi: 10.1016/j.mtadv.2020.100056.

[136] W. Huh, D. Lee, and C. Lee, “Memristors Based on 2D Materials as an Artificial Synapse for Neuromorphic Electronics,” *Adv. Mater.*, vol. 32, no. 51, p. 2002092, Dec. 2020, doi: 10.1002/adma.202002092.

[137] S. G. Hu *et al.*, “Emulating the paired-pulse facilitation of a biological synapse with a NiO_x -based memristor,” *Appl. Phys. Lett.*, vol. 102, no. 18, p. 183510, May 2013, doi: 10.1063/1.4804374.

[138] J. M. Cruz-Albrecht, T. Derosier, and N. Srinivasa, “A scalable neural chip with synaptic electronics using CMOS integrated memristors,” *Nanotechnology*, vol. 24, no. 38, p. 384011, Sep. 2013, doi: 10.1088/0957-4484/24/38/384011.

[139] K. Liao *et al.*, “Memristor Based on Inorganic and Organic Two-Dimensional Materials: Mechanisms, Performance, and Synaptic Applications,” *ACS Appl. Mater. Interfaces*, vol. 13, no. 28, pp. 32606–32623, Jul. 2021, doi: 10.1021/acsami.1c07665.

[140] R. Gesztelyi, J. Zsuga, A. Kemeny-Beke, B. Varga, B. Juhasz, and A. Tosaki, “The Hill equation and the origin of quantitative pharmacology,” *Arch. Hist. Exact Sci.*, vol. 66, no. 4, pp. 427–438, Jul. 2012, doi: 10.1007/s00407-012-0098-5.

[141] S. Goutelle *et al.*, “The Hill equation: a review of its capabilities in pharmacological modelling,” *Fundam. Clin. Pharmacol.*, vol. 22, no. 6, pp. 633–648, Dec. 2008, doi: 10.1111/j.1472-8206.2008.00633.x.

[142] J. G. Wagner, “Kinetics of pharmacologic response I. Proposed relationships between response and drug concentration in the intact animal and man,” *J. Theor. Biol.*, vol. 20, no. 2, pp. 173–201, Aug. 1968, doi: 10.1016/0022-5193(68)90188-4.

[143] D. E. Mager, E. Wyska, and W. J. Jusko, “Diversity of Mechanism-Based Pharmacodynamic Models,” *Drug Metab. Dispos.*, vol. 31, no. 5, pp. 510–518, May 2003, doi: 10.1124/dmd.31.5.510.

[144] C. A. Hunter and H. L. Anderson, “What is Cooperativity?,” *Angew. Chem. Int. Ed.*, vol. 48, no. 41, pp. 7488–7499, Sep. 2009, doi: 10.1002/anie.200902490.

[145] M.A. Grado-Caffaro and M. Grado-Caffaro- Scientific Consultants, C/ Julio Palacios 11, 9-B, 28029-Madrid, Spain, M. A. Grado-Caffaro, M. Grado-Caffaro, and M.A. Grado-Caffaro and M. Grado-Caffaro- Scientific Consultants, C/ Julio Palacios 11, 9-B, 28029-Madrid, Spain, “Fermionic Behaviour of Excitons in Both Paraboli and Non-Parabolic Semiconductors,” *Theor. Phys.*, Mar. 2017, doi: 10.22606/tp.2017.21005.

[146] Z. Lv *et al.*, “Phototunable Biomemory Based on Light-Mediated Charge Trap,” *Adv. Sci.*, vol. 5, no. 9, p. 1800714, Sep. 2018, doi: 10.1002/advs.201800714.

[147] G. Chen and Z. Xu, “Charge trapping and detrapping in polymeric materials,” *J. Appl. Phys.*, vol. 106, no. 12, p. 123707, Dec. 2009, doi: 10.1063/1.3273491.

[148] T. Zhou, G. Chen, R. Liao, and Z. Xu, “Charge trapping and detrapping in polymeric materials: Trapping parameters,” *J. Appl. Phys.*, vol. 110, no. 4, p. 043724, Aug. 2011, doi: 10.1063/1.3626468.

[149] C. K. Williams, “Kinetics of trapping, detrapping, and trap generation,” *J. Electron. Mater.*, vol. 21, no. 7, pp. 711–720, Jul. 1992, doi: 10.1007/BF02655601.

[150] C. Zeng, H. Wang, B. Wang, J. Yang, and J. G. Hou, “Negative differential-resistance device involving two C60 molecules,” *Appl. Phys. Lett.*, vol. 77, no. 22, pp. 3595–3597, Nov. 2000, doi: 10.1063/1.1328773.

[151] Y. V. Pershin and M. D. Ventra, “Comment on ‘If it’s pinched it’s a memristor,’” *Semicond. Sci. Technol.*, vol. 34, no. 9, p. 098001, Sep. 2019, doi: 10.1088/1361-6641/ab3584.

[152] S.-L. Chen, P. B. Griffin, and J. D. Plummer, “Negative Differential Resistance Circuit Design and Memory Applications,” *IEEE Trans. Electron Devices*, vol. 56, no. 4, pp. 634–640, Apr. 2009, doi: 10.1109/TED.2009.2014194.

[153] F. Capasso and R. A. Kiehl, “Resonant tunneling transistor with quantum well base and high-energy injection: A new negative differential resistance device,” *J. Appl. Phys.*, vol. 58, no. 3, pp. 1366–1368, Aug. 1985, doi: 10.1063/1.336109.

[154] S. Bhattacharyya, S. J. Henley, E. Mendoza, L. Gomez-Rojas, J. Allam, and S. R. P. Silva, “Resonant tunnelling and fast switching in amorphous-carbon quantum-well structures,” *Nat. Mater.*, vol. 5, no. 1, pp. 19–22, Jan. 2006, doi: 10.1038/nmat1551.

[155] A. Semenov, O. Semenova, K. Koval, D. Havrilov, A. Volovyk, and D. Kozin, “Frequency Multiplier Based on Field-Effect Transistor Structure with Negative Differential Resistance for Infocommunication System Facilities,” in *2021 IEEE 8th International Conference on Problems of Infocommunications, Science and Technology (PIC S&T)*, Kharkiv, Ukraine, Oct. 2021, pp. 429–433. doi: 10.1109/PICST54195.2021.9772189.

[156] E. Alekseev and D. Pavlidis, “Large-signal microwave performance of GaN-based NDR diode oscillators,” *Solid-State Electron.*, vol. 44, no. 6, pp. 941–947, Jun. 2000, doi: 10.1016/S0038-1101(00)00011-3.

[157] V. Ulansky, A. Raza, and H. Oun, “Electronic Circuit with Controllable Negative Differential Resistance and its Applications,” *Electronics*, vol. 8, no. 4, p. 409, Apr. 2019, doi: 10.3390/electronics8040409.

[158] P. Mainali, L. D. Bastatas, E. Echeverria, P. Wagle, P. Sankaran, and D. N. Mcilroy, “Addressing crosstalk in crossbar memory arrays with a resistive switching ZnO homojunction diode,” *J. Appl. Phys.*, vol. 129, no. 20, p. 205106, May 2021, doi: 10.1063/5.0050564.

[159] S. Lee, H. Kim, J. Park, and K. Yong, “Coexistence of unipolar and bipolar resistive switching characteristics in ZnO thin films,” *J. Appl. Phys.*, vol. 108, no. 7, p. 076101, Oct. 2010, doi: 10.1063/1.3489882.

[160] L. He *et al.*, “Memory and Threshold Resistance Switching in Ni/NiO Core–Shell Nanowires,” *Nano Lett.*, vol. 11, no. 11, pp. 4601–4606, Nov. 2011, doi: 10.1021/nl202017k.

[161] X. Liu, M. T. Mayer, and D. Wang, “Negative differential resistance and resistive switching behaviors in Cu2S nanowire devices,” *Appl. Phys. Lett.*, vol. 96, no. 22, p. 223103, May 2010, doi: 10.1063/1.3442919.

[162] M. S. Kadhim *et al.*, “A resistive switching memory device with a negative differential resistance at room temperature,” *Appl. Phys. Lett.*, vol. 113, no. 5, p. 053502, Jul. 2018, doi: 10.1063/1.5037191.

[163] Y. Cai, Q. Yuan, Y. Ye, J. Liu, and C. Liang, “Coexistence of resistance switching and negative differential resistance in the α-Fe $_2$ O $_3$ nanorod film,” *Phys. Chem. Chem. Phys.*, vol. 18, no. 26, pp. 17440–17445, 2016, doi: 10.1039/C6CP02192A.

[164] Y. Du *et al.*, “Symmetrical Negative Differential Resistance Behavior of a Resistive Switching Device,” *ACS Nano*, vol. 6, no. 3, pp. 2517–2523, Mar. 2012, doi: 10.1021/nn204907t.

[165] X. Ran, P. Hou, J. Song, H. Song, X. Zhong, and J. Wang, “Negative differential resistance effect in resistive switching devices based on h-LuFeO $_3$ /CoFe $_2$ O $_4$ heterojunctions,” *Phys. Chem. Chem. Phys.*, vol. 22, no. 10, pp. 5819–5825, 2020, doi: 10.1039/D0CP00530D.

[166] T. Guo, B. Sun, Y. Zhou, H. Zhao, M. Lei, and Y. Zhao, “Overwhelming coexistence of negative differential resistance effect and RRAM,” *Phys. Chem. Chem. Phys.*, vol. 20, no. 31, pp. 20635–20640, 2018, doi: 10.1039/C8CP03492C.

[167] T. W. Hickmott, “Potential Distribution and Negative Resistance in Thin Oxide Films,” *J. Appl. Phys.*, vol. 35, no. 9, pp. 2679–2689, Sep. 1964, doi: 10.1063/1.1713823.

[168] T. W. Hickmott, “Impurity Conduction and Negative Resistance in Thin Oxide Films,” *J. Appl. Phys.*, vol. 35, no. 7, pp. 2118–2122, Jul. 1964, doi: 10.1063/1.1702801.

[169] J. F. Scott *et al.*, “Negative differential resistivity in ferroelectric thin-film current-voltage relationships,” *Integr. Ferroelectr.*, vol. 4, no. 1, pp. 85–92, Feb. 1994, doi: 10.1080/10584589408018662.

[170] K. Watanabe, A. J. Hartmann, R. N. Lamb, and J. F. Scott, “Electronic characteristics of the SrBi2Ta2O9–Pt junction,” *J. Appl. Phys.*, vol. 84, no. 4, pp. 2170–2175, Aug. 1998, doi: 10.1063/1.368279.

[171] M. Sajedi Alvar, P. W. M. Blom, and G.-J. A. H. Wetzelaer, “Space-charge-limited electron and hole currents in hybrid organic-inorganic perovskites,” *Nat. Commun.*, vol. 11, no. 1, p. 4023, Dec. 2020, doi: 10.1038/s41467-020-17868-0.

[172] A. Asamitsu, Y. Tomioka, H. Kuwahara, and Y. Tokura, “Current switching of resistive states in magnetoresistive manganites,” *Nature*, vol. 388, no. 6637, pp. 50–52, Jul. 1997, doi: 10.1038/40363.

[173] W. Kim, A. Javey, O. Vermesh, Q. Wang, Y. Li, and H. Dai, “Hysteresis Caused by Water Molecules in Carbon Nanotube Field-Effect Transistors,” *Nano Lett.*, vol. 3, no. 2, pp. 193–198, Feb. 2003, doi: 10.1021/nl0259232.

[174] F. Gao *et al.*, “Impact of Moisture and Fluorocarbon Passivation on the Current Collapse of AlGaN/GaN HEMTs,” *IEEE Electron Device Lett.*, vol. 33, no. 10, pp. 1378–1380, Oct. 2012, doi: 10.1109/LED.2012.2206556.

[175] M. Legodi and D. Dewaal, “The preparation of magnetite, goethite, hematite and maghemite of pigment quality from mill scale iron waste,” *Dyes Pigments*, vol. 74, no. 1, pp. 161–168, 2007, doi: 10.1016/j.dyepig.2006.01.038.

[176] S. Yin, X. Ma, and D. E. Ellis, “Initial stages of H2O adsorption and hydroxylation of Fe-terminated α-Fe2O3(0001) surface,” *Surf. Sci.*, vol. 601, no. 12, pp. 2426–2437, Jun. 2007, doi: 10.1016/j.susc.2007.04.059.

[177] M. Lampert, “Injection Currents in Insulators,” *Proc. IRE*, vol. 50, no. 8, pp. 1781–1796, Aug. 1962, doi: 10.1109/JRPROC.1962.288218.

[178] P. N. Murgatroyd, “Theory of space-charge-limited current enhanced by Frenkel effect,” *J. Phys. Appl. Phys.*, vol. 3, no. 2, pp. 151–156, Feb. 1970, doi: 10.1088/0022-3727/3/2/308.

[179] Y. Seo, S. Lee, I. An, C. Song, and H. Jeong, “Conduction mechanism of leakage current due to the traps in ZrO $_2$ thin film,” *Semicond. Sci. Technol.*, vol. 24, no. 11, p. 115016, Nov. 2009, doi: 10.1088/0268-1242/24/11/115016.

[180] X. Wang *et al.*, “Oxygen vacancy defects engineering on Ce-doped α-Fe2O3 gas sensor for reducing gases,” *Sens. Actuators B Chem.*, vol. 302, p. 127165, Jan. 2020, doi: 10.1016/j.snb.2019.127165.

[181] J. Li, H.-F. Zhang, G.-Q. Shao, B.-L. Wu, and S.-X. Ouyang, “Negative differential resistance: Another banana?,” *EPL Europhys. Lett.*, vol. 108, no. 2, p. 27005, Oct. 2014, doi: 10.1209/0295-5075/108/27005.

[182] S. Sikarwar and B. C. Yadav, “Opto-electronic humidity sensor: A review,” *Sens. Actuators Phys.*, vol. 233, pp. 54–70, Sep. 2015, doi: 10.1016/j.sna.2015.05.007.

[183] A. Sett, K. Biswas, S. Majumder, A. Datta, and T. Kanti Bhattacharyya, “Graphene and Its Nanocomposites Based Humidity Sensors: Recent Trends and Challenges,” in *Humidity Sensors [Working Title]*, IntechOpen, 2021. doi: 10.5772/intechopen.98185.

[184] D. Li, E.-J. Borkent, R. Nortrup, H. Moon, H. Katz, and Z. Bao, “Humidity effect on electrical performance of organic thin-film transistors,” *Appl. Phys. Lett.*, vol. 86, no. 4, p. 042105, Jan. 2005, doi: 10.1063/1.1852708.

[185] Y. Yao, X. Chen, J. Zhu, B. Zeng, Z. Wu, and X. Li, “The effect of ambient humidity on the electrical properties of graphene oxide films,” *Nanoscale Res. Lett.*, vol. 7, no. 1, p. 363, Dec. 2012, doi: 10.1186/1556-276X-7-363.

[186] A. Sun, L. Huang, and Y. Li, “Study on humidity sensing property based on TiO2 porous film and polystyrene sulfonic sodium,” *Sens. Actuators B Chem.*, vol. 139, no. 2, pp. 543–547, Jun. 2009, doi: 10.1016/j.snb.2009.03.064.

[187] E. Traversa, “Ceramic sensors for humidity detection: the state-of-the-art and future developments,” *Sens. Actuators B Chem.*, vol. 23, no. 2–3, pp. 135–156, Feb. 1995, doi: 10.1016/0925-4005(94)01268-M.

[188] C.-D. Feng, S.-L. Sun, H. Wang, C. U. Segre, and J. R. Stetter, “Humidity sensing properties of Nation and sol-gel derived SiO2/Nation composite thin films,” p. 6.

[189] R. Fenner and E. Zdankiewicz, “Micromachined water vapor sensors: a review of sensing technologies,” *IEEE Sens. J.*, vol. 1, no. 4, pp. 309–317, Dec. 2001, doi: 10.1109/7361.983470.

[190] P. Singh, C. Shekhar Kushwaha, S. K. Shukla, and G. C. Dubey, “Synthesis and humidity sensing property of α-Fe 2 O 3 and polyaniline composite,” *Mater. Today Proc.*, vol. 5, no. 3, pp. 9118–9125, 2018, doi: 10.1016/j.matpr.2017.10.030.

[191] A. D. Smith *et al.*, “Resistive graphene humidity sensors with rapid and direct electrical readout,” *Nanoscale*, vol. 7, no. 45, pp. 19099–19109, 2015, doi: 10.1039/C5NR06038A.

[192] H. M. Zeeshan Yousaf, S. W. Kim, G. Hassan, K. Karimov, K. H. Choi, and M. Sajid, “Highly sensitive wide range linear integrated temperature compensated humidity sensors fabricated using Electrohydrodynamic printing and electrospray deposition,” *Sens. Actuators B Chem.*, vol. 308, p. 127680, Apr. 2020, doi: 10.1016/j.snb.2020.127680.

[193] M. U. Khan, Q. M. Saqib, G. Hassan, and J. Bae, “All printed organic humidity sensor based on egg albumin,” *Sens. Bio-Sens. Res.*, vol. 28, p. 100337, Jun. 2020, doi: 10.1016/j.sbsr.2020.100337.

[194] M. U. Khan, G. Hassan, and J. Bae, “Bio-compatible organic humidity sensor based on natural inner egg shell membrane with multilayer crosslinked fiber structure,” *Sci. Rep.*, vol. 9, no. 1, p. 5824, Dec. 2019, doi: 10.1038/s41598-019-42337-0.

[195] M. Awais, M. U. Khan, A. Hassan, J. Bae, and T. E. Chattha, “Printable Highly Stable and Superfast Humidity Sensor Based on Two Dimensional Molybdenum Diselenide,” *Sci. Rep.*, vol. 10, no. 1, p. 5509, Dec. 2020, doi: 10.1038/s41598-020-62397-x.

[196] A. M. Soomro, F. Jabbar, M. Ali, J.-W. Lee, S. W. Mun, and K. H. Choi, “All-range flexible and biocompatible humidity sensor based on poly lactic glycolic acid

(PLGA) and its application in human breathing for wearable health monitoring," *J. Mater. Sci. Mater. Electron.*, vol. 30, no. 10, pp. 9455–9465, May 2019, doi: 10.1007/s10854-019-01277-1.

[197] S. Muto, O. Suzuki, T. Amano, and M. Morisawa, "A plastic optical fibre sensor for real-time humidity monitoring," *Meas. Sci. Technol.*, vol. 14, no. 6, pp. 746–750, Jun. 2003, doi: 10.1088/0957-0233/14/6/306.

[198] Yinping Miao *et al.*, "Relative Humidity Sensor Based on Tilted Fiber Bragg Grating With Polyvinyl Alcohol Coating," *IEEE Photonics Technol. Lett.*, vol. 21, no. 7, pp. 441–443, Apr. 2009, doi: 10.1109/LPT.2009.2013185.

[199] C. Caliendo, E. Verona, A. D'Amico, A. Furlani, G. Iucci, and M. V. Russo, "Surface acoustic wave humidity sensor," *Sens. Actuators B Chem.*, vol. 16, no. 1–3, pp. 288–292, Oct. 1993, doi: 10.1016/0925-4005(93)85197-I.

[200] M. Penza and V. I. Anisimkin, "Surface acoustic wave humidity sensor using polyvinyl-alcohol film," *Sens. Actuators Phys.*, vol. 76, no. 1–3, pp. 162–166, Aug. 1999, doi: 10.1016/S0924-4247(99)00004-7.

[201] Y.-C. Yeh, T.-Y. Tseng, and D.-A. Chang, "Electrical Properties of Porous Titania Ceramic Humidity Sensors," *J. Am. Ceram. Soc.*, vol. 72, no. 8, pp. 1472–1475, Aug. 1989, doi: 10.1111/j.1151-2916.1989.tb07679.x.

[202] W. Qu and J.-U. Meyer, "A novel thick-film ceramic humidity sensor," *Sens. Actuators B Chem.*, vol. 40, no. 2–3, pp. 175–182, May 1997, doi: 10.1016/S0925-4005(97)80258-4.

[203] B. C. Yadav, R. C. Yadav, and P. K. Dwivedi, "Sol–gel processed (Mg–Zn–Ti) oxide nanocomposite film deposited on prism base as an opto-electronic humidity sensor," *Sens. Actuators B Chem.*, vol. 148, no. 2, pp. 413–419, Jul. 2010, doi: 10.1016/j.snb.2010.05.046.

[204] B. C. Yadav, P. Sharma, and P. K. Khanna, "Morphological and humidity sensing characteristics of SnO2-CuO, SnO2-Fe2O3 and SnO2-SbO2 nanocooxides," *Bull. Mater. Sci.*, vol. 34, no. 4, pp. 689–698, Jul. 2011, doi: 10.1007/s12034-011-0183-4.

[205] J. J. Steele, M. T. Taschuk, and M. J. Brett, "Nanostructured Metal Oxide Thin Films for Humidity Sensors," *IEEE Sens. J.*, vol. 8, no. 8, pp. 1422–1429, Aug. 2008, doi: 10.1109/JSEN.2008.920715.

[206] M.-R. Yang and K.-S. Chen, "Humidity sensors using polyvinyl alcohol mixed with electrolytes," *Sens. Actuators B Chem.*, vol. 49, no. 3, pp. 240–247, Jul. 1998, doi: 10.1016/S0925-4005(98)00134-8.

[207] Y. Sakai, Y. Sadaoka, and M. Matsuguchi, “Humidity sensors based on polymer thin films,” *Sens. Actuators B Chem.*, vol. 35, no. 1–3, pp. 85–90, Sep. 1996, doi: 10.1016/S0925-4005(96)02019-9.

[208] Q. Zafar and K. Sulaiman, “Utility of PCDTBT polymer for the superior sensing parameters of electrical response based relative humidity sensor,” *React. Funct. Polym.*, vol. 105, pp. 45–51, Aug. 2016, doi: 10.1016/j.reactfunctpolym.2016.05.014.

[209] K. Jiang, T. Fei, and T. Zhang, “Humidity sensor using a Li-loaded microporous organic polymer assembled by 1,3,5-trihydroxybenzene and terephthalic aldehyde,” *RSC Adv.*, vol. 4, no. 54, p. 28451, 2014, doi: 10.1039/c4ra02763a.

[210] M. Muhajir, P. Puspitasari, and J. A. Razak, “Synthesis and Applications of Hematite α-Fe2O3 : a Review,” *J. Mech. Eng. Sci. Technol.*, vol. 3, no. 2, pp. 51–58, Nov. 2019, doi: 10.17977/um016v3i22019p051.

[211] W. R. W. Ahmad, M. H. Mamat, A. S. Zoolfakar, Z. Khusaimi, and M. Rusop, “A review on hematite α-Fe2O3 focusing on nanostructures, synthesis methods and applications,” in *2016 IEEE Student Conference on Research and Development (SCOReD)*, Kuala Lumpur, Malaysia, Dec. 2016, pp. 1–6. doi: 10.1109/SCORED.2016.7810090.

[212] Y. Lin, G. Yuan, S. Sheehan, S. Zhou, and D. Wang, “Hematite-based solar water splitting: challenges and opportunities,” *Energy Environ. Sci.*, vol. 4, no. 12, p. 4862, 2011, doi: 10.1039/c1ee01850g.

[213] K. P. Patil, K. V.R, M. K. B, and W. R. B., “Hydrothermal Synthesis of Fe2O3 for the Humidity Sensing Application,” *Int. Res. J. Adv. Sci. Hub*, vol. 2, no. Special Issue ICAET 11S, pp. 56–60, Dec. 2020, doi: 10.47392/irjash.2020.234.

[214] M. U. Khan, G. Hassan, M. Awais, and J. Bae, “All printed full range humidity sensor based on Fe2O3,” *Sens. Actuators Phys.*, vol. 311, p. 112072, Aug. 2020, doi: 10.1016/j.sna.2020.112072.

[215] V. Manikandan, “Real environment humidity-sensing ability of Nd-doped Fe2O3 sensor,” *Sens. Bio-Sens. Res.*, vol. 33, p. 100439, Aug. 2021, doi: 10.1016/j.sbsr.2021.100439.

[216] M. T. S. Chani, K. S. Karimov, S. B. Khan, A. M. Asiri, M. Saleem, and M. M. Bashir, “Fe2O3–silicone adhesive composite based humidity sensors,” p. 6.

[217] A. Miura, Y. Uraoka, T. Fuyuki, S. Yoshii, and I. Yamashita, “Floating nanodot gate memory fabrication with biomineralized nanodot as charge storage node,” *J. Appl. Phys.*, vol. 103, no. 7, p. 074503, Apr. 2008, doi: 10.1063/1.2888357.

[218] M. Ambrico *et al.*, “Hysteresis-type current–voltage characteristics in Au/eumelanin/ITO/glass structure: Towards melanin based memory devices,” *Org. Electron.*, vol. 11, no. 11, pp. 1809–1814, Nov. 2010, doi: 10.1016/j.orgel.2010.08.001.

APPENDICES

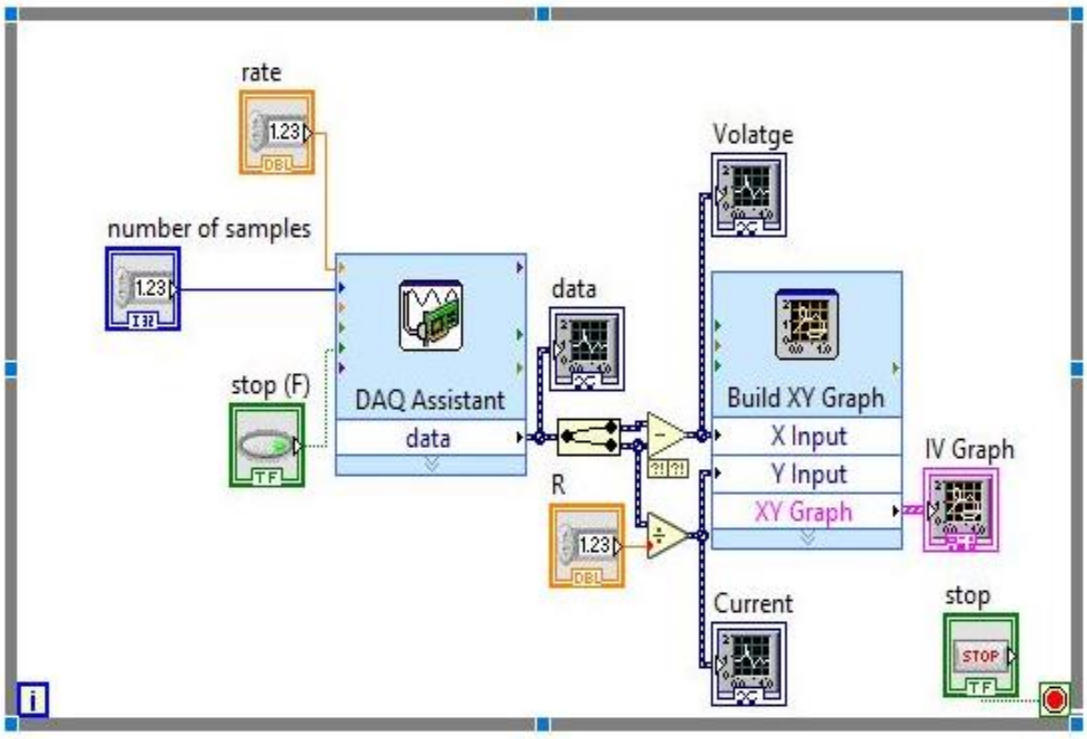

Fig. 1: Block diagram of Labview program used to get I-V characteristics of ZnO double layer device at different AC frequencies using a voltage divider circuit and PXIe data acquisition device.

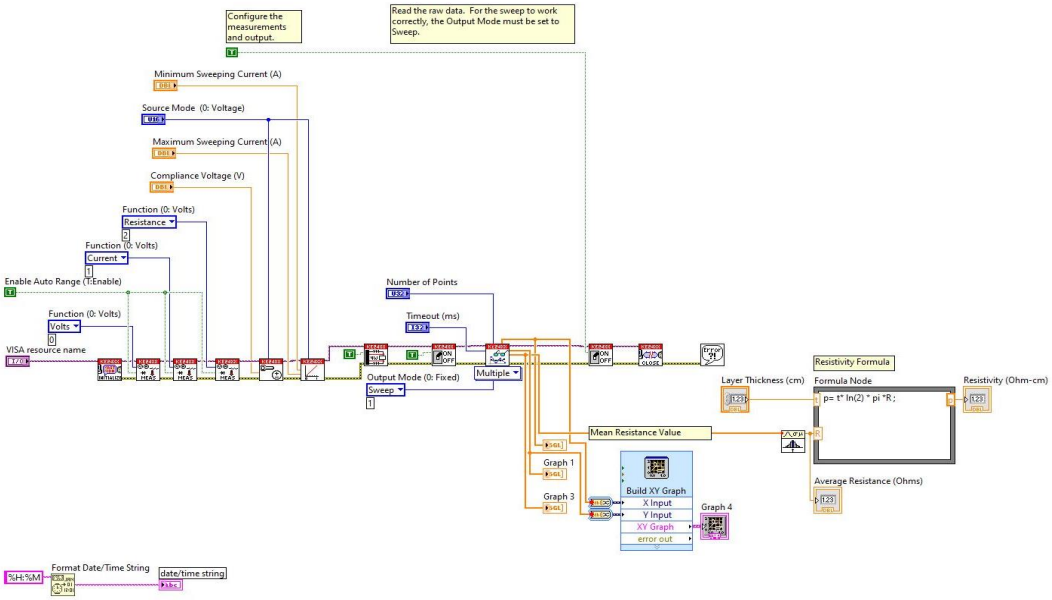

Fig. 2: Block diagram of Labview program used to get resistivity of ZnO thin films using 4 point probe method.

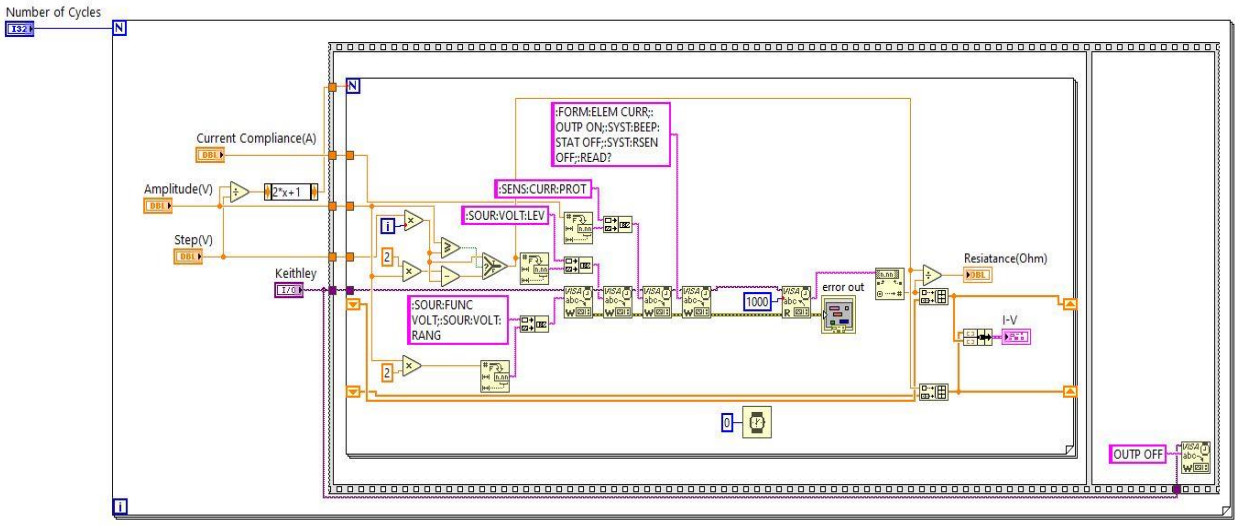

Fig. 3: Block diagram of Labview program used to get cycles of unipolar I-V characteristics using Keithley source meter.

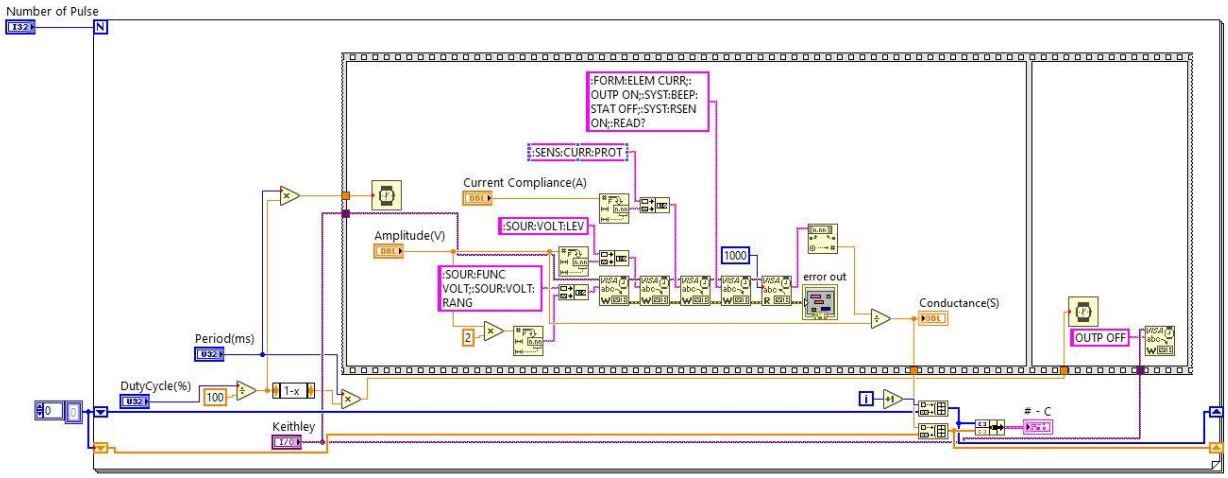

Fig. 4: Block diagram of Labview program used to measure conductance data as a function of number of pulse through the sample using Keithley source meter.

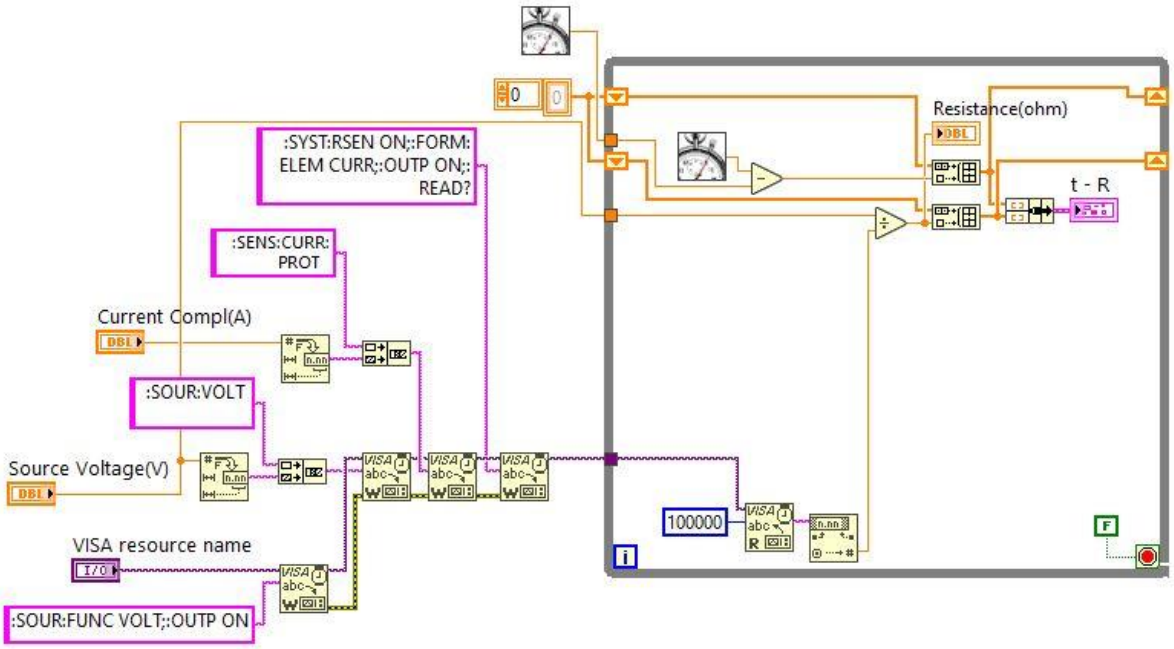

Fig. 5: Block diagram of Labview program used to monitor resistance of the sensor in real time using Keithley source meter.

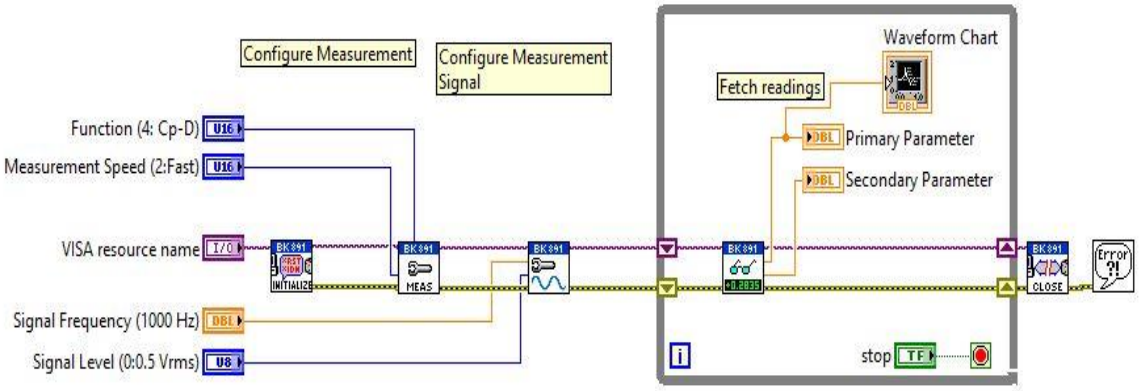

Fig. 6: Block diagram of Labview program used to measure capacitance of the sample at different RH level by using LCR meter.

VITA

Punya Prasad Mainali

Candidate for the Degree of

Doctor of Philosophy

Thesis: CHARGE STORAGE AND TRANSPORT IN METAL OXIDE RESISTIVE SWITCHING DEVICES

Major Field: Physics

Biographical:

Education:

Completed the requirements for the Doctor of Philosophy in experimental condensed matter physics at Oklahoma State University, Stillwater, Oklahoma in December, 2022.
Completed the requirements for the Master of Science in physics at Oklahoma State University, Stillwater, Oklahoma in December, 2020.
Completed the requirements for the Master of Science in physics at Tribhuvan University, Kathmandu, Nepal in December, 2017.
Completed the requirements for the Bachelor of Science in Physics at Tribhuvan University, Kathmandu, Nepal in 2014.

Experience:

DRAM Thin film process development engineer at Micron Semiconductor Inc. starting in March 2023.
Graduate teaching and research assistant: 2017-2022 at Oklahoma State University.

Publications:

Mainali et al. J. Appl. Phys., vol. 129, no. 20, p. 205106, May 2021, doi: 10.1063/5.0050564.
Austin et al. Nanomaterials 2020, 10, 2434.
Bastatas et al. ACS Sens., vol. 3, no. 11, pp. 2367–2374, Nov. 2018, doi: 10.1021/acssensors.8b00746.